THE DESIGN AND ANALYSIS OF AN OPTOELECTRONIC BROADBAND MATRIX SWITCH

by

JAMES ALAN STRACHAN
B.A.Sc., University of British Columbia, 1980

A THESIS SUBMITTED IN PARTIAL FULFILLMENT
OF THE REQUIREMENTS FOR THE DEGREE OF
MASTER OF APPLIED SCIENCE
in the Department of
Electrical Engineering

We accept this thesis as conforming
to the required standard

[redacted]
Supervisor Dr. V. K. Bhargava

[redacted]
Dr. P. F. Driessen

[redacted]
Dr. G. C. Shoja

[redacted]
Dr. E. H. Hara

June 4, 1987

Supervisor: Professor V.K. Bhargava

ABSTRACT

Optoelectronic matrix switches using switching photodiodes have a number of distinct advantages which make them attractive for broadband switching applications. Their broad frequency bandwidth capabilities, high isolation on/off ratio and low crosstalk in the input and output distribution lines readily lead to the construction of large dimension matrix switches.

This thesis presents the design and analysis of a 2×4 broadband optoelectronic matrix switch operating at a wavelength of 1.55 μm. The switch is constructed utilizing InGaAs/InP avalanche photodiodes and an InGaAsP laser source modulated with several signals to test the performance of the switch over a wide range of frequencies. The switch is analyzed using conventional mathematical techniques for loss, SNR and frequency response and a system model is developed to characterize the overall performance. The results are then compared to actual measured data and summarized.

Examiners:

[redacted]

Supervisor Dr. V. K. Bhargava

[redacted]

Dr. P. F. Driessen

[redacted]

Dr. G. C. Shoja

[redacted]

Dr. E. H. Hara

Contents

List of Tables

List of Figures

ACKNOWLEDGEMENTS

I would like to thank Dr. E.H. Hara and Dr. V.K. Bhargava for their guidance, during the course of this project and for their helpful advice during the preparation of this manuscript. I would also like to express my appreciation to the British Columbia Telephone Company for offering me the opportunity to continue my education and for providing financial assistance.

DEDICATION

to

the memory of

James Strachan

1902-1982

Chapter 1

Introduction

1.1 Introduction

With the rapid deployment of fibre optic systems in telecommunications networks throughout the world, larger bandwidths and higher bit rates are being transmitted. The ability to route or switch this information within and between systems is becoming increasingly important to those companies wishing to better utilize their fibre optics networks. Data rates of up to 1 gigabit per second, required for high definition television (HDTV), will soon be transmitted to subscribers in certain countries and methods of switching this high bit rate through the existing fibre networks is being explored.

Section 1.2 of this chapter reviews the development of several of these methods while section 1.3 provides a summary of the most promising, including the optoelectronic switch to be studied here.

Chapter 2 presents the overall design and construction of the optoelec-

tronic switch. Characteristics of the components are discussed in addition to material and RF leakage problems. Insertion loss, isolation, frequency response and switching response measurements are made.

In Chapter 3, an analytical system model of the optoelectronic switch is developed. Equivalent circuit models for the laser and photodiodes are presented and used to calculate the frequency response. Loss models for the fibre couplers and splice losses are used to calculate the overall insertion loss of the system.

In Chapter 4, experimental measurements are compared to the theoretical results and in the last chapter, results are summarized and further directions for research are suggested.

1.2 Overview of Existing Switching Methods

1.2.1 Electrooptic

Proposed in 1969 by Miller [1] and Marcatili [53] of Bell Laboratories, dielectric waveguide couplers were first constructed of two parallel slab waveguides. The waveguide with an index of refraction, n, was immersed in another dielectric with a slightly smaller index of refraction. The separation between the two slabs determined the degree of optical power coupled from the first slab to the second. The length L of the two guides determined the distance of propagation required for the energy to be transferred from one

guide to another [3].

The first electrooptic switch was proposed by Taylor [3] in 1973. He stated, that an electric potential could be applied across the dielectric slabs inducing a change in the refractive indices, thus changing the propagation constant β and the propagation length L. With electrical control over the propagation length, two states could be created as shown in Figures 1.1a and b with the resulting voltage vs. output power graph as shown in Figure 1.1c. The "bar" or off state where light entering one slab outputs from the same slab, and the "cross" or on state, where light entering one slab is transferred or coupled to the second slab.

In 1975, Papuchon et al [4] and Kogelnik and Schmidt [5] constructed such switches based on $Ti : LiNbO_3$. Two parallel Ti strips were diffused onto the $LiNbO_3$ substrate and switching occurred when the propagation constant mismatch $\Delta\beta$ between the two guides was zero. Approximately 6 Volts was required to make $\Delta\beta = 0$.

Early electrooptic switches were fabricated with long coupling lengths (typically several mm) and operated at a wavelength $\lambda = .63\mu m$. As work on longer wavelength switches progressed, it was discovered [6] that higher switching voltages (50-80V) [7] were required to produce the cross state. As these "basic" switches were combined to produce larger matrices, the size of the basic switch was reduced to accommodate more elements on a single substrate. This reduced coupling length also increased the required

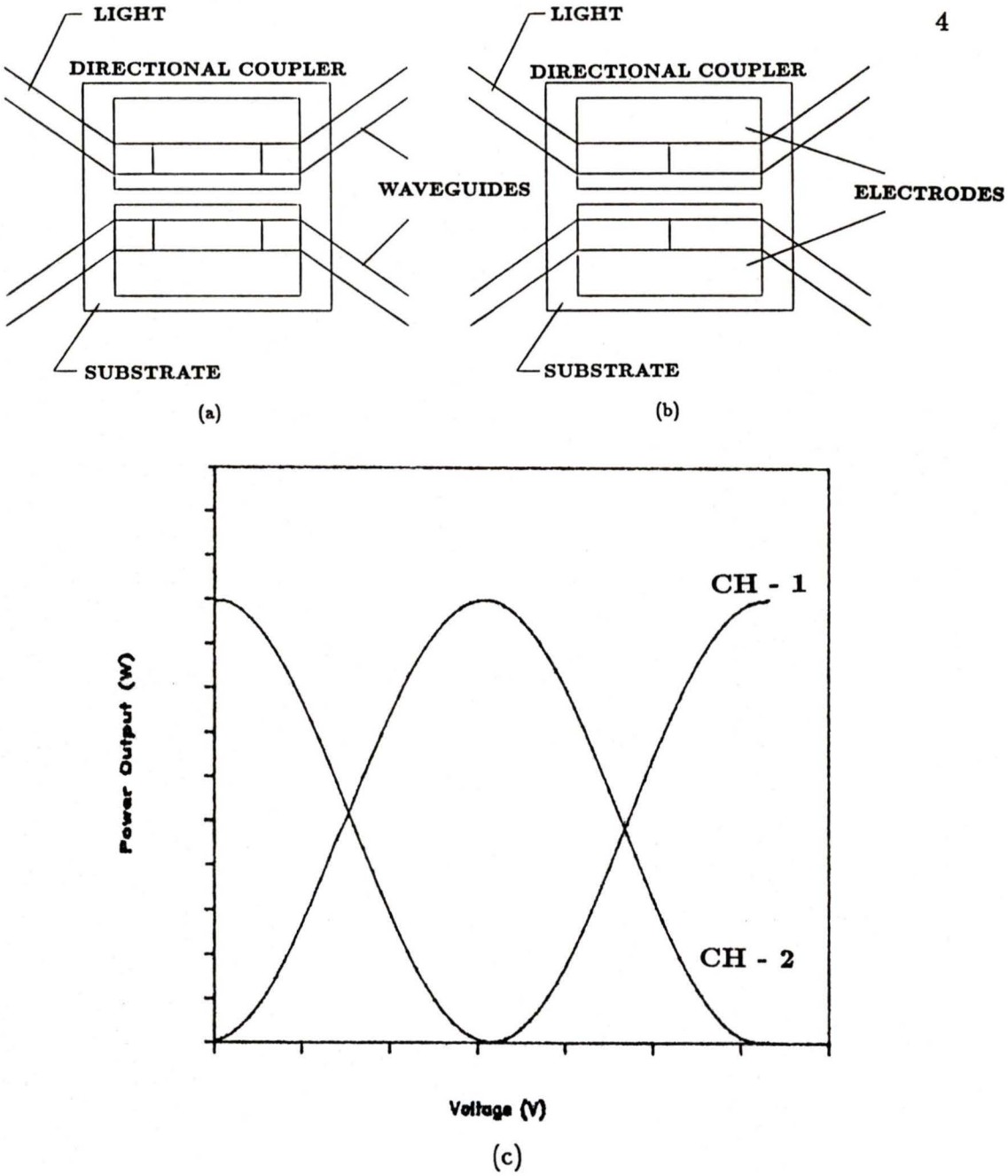

Figure 1.1: The two states of an electrooptic switch. a) The "bar" state. b) The "cross" state. c)Voltage vs output power.

switching voltage [8]. With new fabrication techniques [9], this voltage was reduced to acceptable levels (5-10V).

Recent results at $\lambda = 1.3\mu m$ shows the total attenuation or path insertion loss for a basic 2×2 switch at $\approx$ 10dB with a crosstalk figure of $\approx$ -25dB for a bandwidth of 2GHz [10]. Switching speeds of 100ps have recently been recorded [11]. Recently, a $Ti : LiNbO_3$ switch has been designed and fabricated at the $1.55\mu m$ wavelength [12], with an insertion loss of $<$ 3dB and a switching voltage of 10V. Several different matrix switches have been fabricated and tested [13,8,14] with the largest being an 8×8 strictly nonblocking switch with an insertion loss of $< 7dB$ and a switching voltage of 26V [15].

It has been shown [10], that the maximum matrix size for a particular electrooptic switch can be determined by the optical SNR and the attenuation α through the switch. The first order approximations are given by Equations (1.1) and (1.2) [10].

$$SNR_{wc} = X_X(dB) - \alpha_B - (N-1)\alpha_C(dB) - 10\log\left[\frac{1 - 10^{\frac{-(N-1)\alpha_C(dB)}{10}}}{1 - 10^{\frac{-\alpha_C(dB)}{10}}}\right] \tag{1.1}$$

$$
\begin{array}{rrcl}
where & SNR_{wc} & = & the\ worst\ case\ SNR \\
 & X_X & = & is\ the\ coupler\ crosstalk \\
 & \alpha_B & = & is\ the\ bar\ loss \\
 & \alpha_C & = & is\ the\ cross\ loss \\
 & N & = & size\ of\ the\ matrix(N \times N)
\end{array}
$$

$$\alpha_{wc} = \alpha_B + (2N - 2)\alpha_C \tag{1.2}$$

Utilizing current technology, these equations lead to a maximum matrix size of 8 × 8 for an optical SNR of greater than 11dB. However, improvements in fabrication technology will most likely lower the crosstalk and insertion levels down to where larger matrices can be fabricated.

One of the drawbacks of using $LiNbO_3$ as the waveguide is its inability to allow integration of the laser or receiving photodiode onto a single substrate. Galium Arsenide (GaAs) materials are currently being investigated [16] but the electrooptic coefficient is less sensitive than that of $LiNbO_3$ so higher switching voltages would be required.

1.2.2 Mechanical

Mechanical, or moving fibre switches, operate by shifting a single fibre or group of fibres against another array of fibres, thereby disconnecting and connecting different transmission paths. The fibres must be aligned accurately to allow maximum power transfer.

One of the first such switches [17] used a square tube in which two

multimode output fibres were positioned diagonally across from each other at the corners of the tube. The input fibre (60 μm outside diameter) was positioned from the outside into the appropriate corner of the tube for either fibre 1 or 2. Index matching fluid was used to reduce insertion loss.

A second method, utilizes V grooves to improve the alignment [18] of both the input and output fibres. These fibres are also multimode with an outer diameter of 150 μm and a core diameter of 60 μm. The output fibres are fixed onto a block in the shape of a fan while the input fibre moves in an arc to connect to the appropriate output fibre. Producing an insertion loss of only .25dB with a crosstalk figure of -60dB, switches of this kind have been constructed up to a matrix size of 1×93 [19].

With the move toward single mode fibre systems, more accurate alignment methods are being developed to compensate for the smaller fibre core diameter (approx. 9 μm) [20]. The fibre is firmly placed into a slotted silicon chip which has parallel grooves etched onto the top and bottom surfaces. These chips are then stacked together to form an array. By sliding along the etched grooves, very accurate alignment is possible. Insertion loss for this type of switch is less than 1dB with a crosstalk figure of approximately -70dB [20].

Mechanical switches have found commercial use in situations where the environment is rugged and reliability must be maintained such as the AT&T SL submarine cable.

1.2.3 Optoelectronic

Optoelectronic switches are a combination of electronic and optical switching, where a photodiode is used as the switching device. A modulated signal is delivered to the photodiode via a fibre waveguide, thus reducing crosstalk within the switch. A schematic of this configuration is shown in Figure 1.2. The photodiodes are turned on or off by means of a suitable bias control. In a matrix switch, the output of the photodiodes are connected together to form a single output line.

Homojunction photodiodes or Si PIN photodiodes were the first switching devices used [21,22]. Acting as a large capacitor in the off-state, because of the forward bias current (20mA), the photodiode effectively short circuited the output load resistor R_L. This device provided suitable isolation (80dB) up to 230 MHz but required a fairly large voltage (20V) to switch and had a switching time of about 100ns.

With the fabrication of longer wavelength heterojunction photodiodes (eg. GaInP/InP), shorter switching times of 30ns were observed [23,24] up to frequencies of 500 MHz. In contrast to the Si PIN optoelectronic switch, the GaInP/InP switch required only the removal of the bias voltage to achieve the off-state because the heterojunction created a potential barrier which the photo-electrons could not pass through. A comparatively high reverse voltage of 30V was required for the on-state which made it difficult

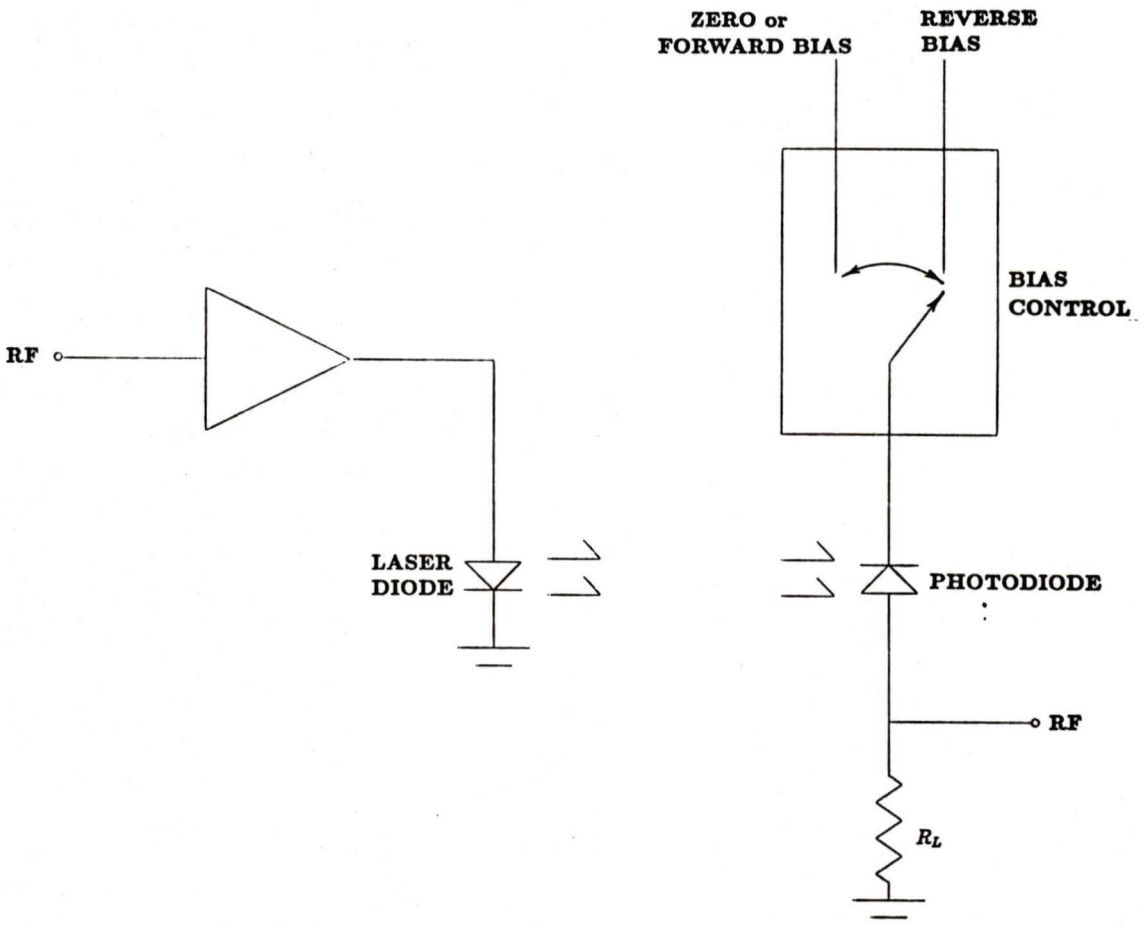

Figure 1.2: Principle of operation of the optoelectronic switch.

to achieve nanosecond switching times.

Using GaAs field effect transistors (FET), photoconductive optoelectronic switches exhibited switching times of less than 1ns up to frequencies of 1GHz with a low operating voltage [25,26]. The on-state and off-state were achieved by 7V and 0V respectively. Switching times of 250 ps with a frequency response beyond 20 GHz have been predicted [26].

Experimental matrix switches have been designed and constructed incorporating all three of the above devices. Suitable shielding of the output lines reduces electronic (RF) crosstalk.

The largest optoelectronic matrix switch constructed to date is an Si PIN matrix, 7×7 in size with a crosstalk figure of -80dB and a passband of 10Hz to 100MHz [26]. With the reduction in costs and increased availability of longer wavelength devices, optoelectronic switches in the long wavelength region can now be constructed readily.

1.2.4 All Optical Switching

With the increasing interest in the all-optical computer, devices which exhibit ultra fast switching times ($<$ 1ps) and can behave like a logic gate have been developed.

Unlike electrooptic switches which are electrically controlled and are therefore limited by the speed of the electronics, all optical or self-electro-optic-devices (SEED) [27,28,29,30] are optically controlled which allows

ultrafast switching. These new devices are constructed using a multiple quantum well structure (MQW) which exhibits an electro-absorption effect where certain wavelengths of light can be absorbed by the material. The wavelength where absorption takes place can be changed by inducing an electrical charge. In the SEED device, the light absorbed produces a photocurrent which in turn, when passed through a load, can change the voltage across the MQW structure, producing an optoelectronic feedback. If operated in a region of positive feedback, a switching function is obtained. Devices have been fabricated which have a switching time of 0.5ns and require less than a femtojoule of optical energy to change switching states.

1.2.5 Other Methods

Magnetooptic

Based on the Faraday effect of certain crystal structures, particularly yttrium-iron-garnet (YIG) [31], magnetooptic switches have been developed which exhibit low insertion loss and require less than 5V switching voltage.

The optical path is changed by controlling the rotation of the polarization plane of light [32]. By applying a small magnetic field ($\approx$ 100 Oe.) to a YIG crystal, a $\pm 45^{o}$ Faraday rotation is created. The input light signal is passed through a prism and is separated into two perpendicular polar-

ized components. After passing through the Faraday rotator, these two components are optically separated. Optical switching occurs by reversing the direction the the magnetic field applied to the crystal. Such a device is shown in Figure 1.3. The input light beam entering at A is separated by the polarization separation film into an s-component and a p-component. The s-component exits at the top of the prism and the p-component exits at the bottom. Light input at B is also separted into the s and p components but exit the crystal with the s-component at the bottom and the p-component at the top.

Initial designs of this switch [32] required a YIG crystal for each of

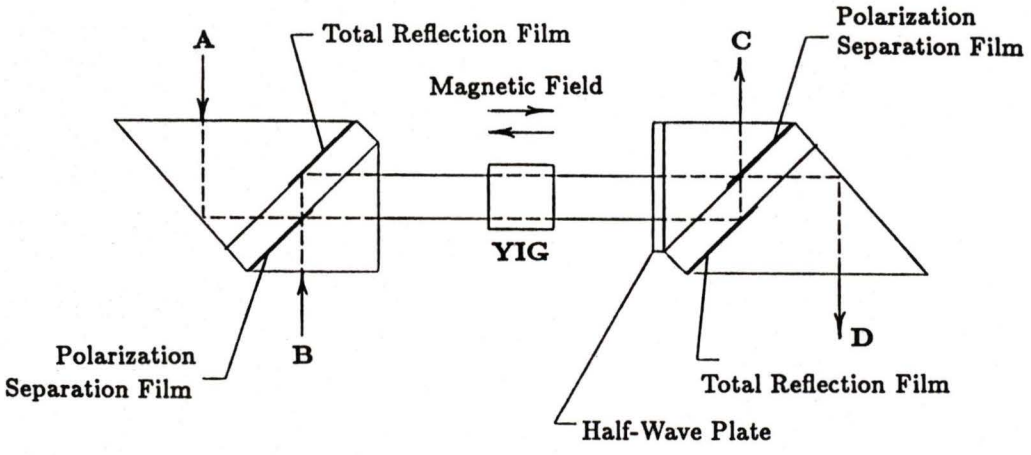

Figure 1.3: Magnetooptic switch using a YIG crystal. A and B are the input light beams. C and D are the output light beams.

the polarized components. A new design has been developed which requires only one crystal for both paths and has a measured insertion loss of 1.2dB

with a far-end crosstalk figure of -26dB [33].

The major advantage of the magnetooptic switch is the independence of insertion loss to the polarization state.

Acoustooptic

The deflection of an optically guided wave by a surface acoustic wave was observed by Kuhn et al [34] who measured the deflection efficiency and diffracted wave angle on a glass plate.

As with electrooptic switching, it was discovered that $LiNbO_3$ also exhibited a large acoustooptic effect [35] and thus all the necessary components could be integrated onto one substrate. Two parallel slab waveguides were etched onto the substrate between two surface acoustic transducers as shown in Figure 1.4. The acoustic wave created by the transducers caused a change in the propagation constant β as well as the coupling coefficient κ producing modulations of $\Delta\beta$ and $\Delta\kappa$ in the two quantities. Devices have been fabricated up to $\lambda = 1.3\mu m$ with crosstalk measured at -30dB [36].

Acoustooptic switch wavelengths are limited by the acoustic wavelengths that can be generated by the transducers and the the acoustooptic coefficient of the material.

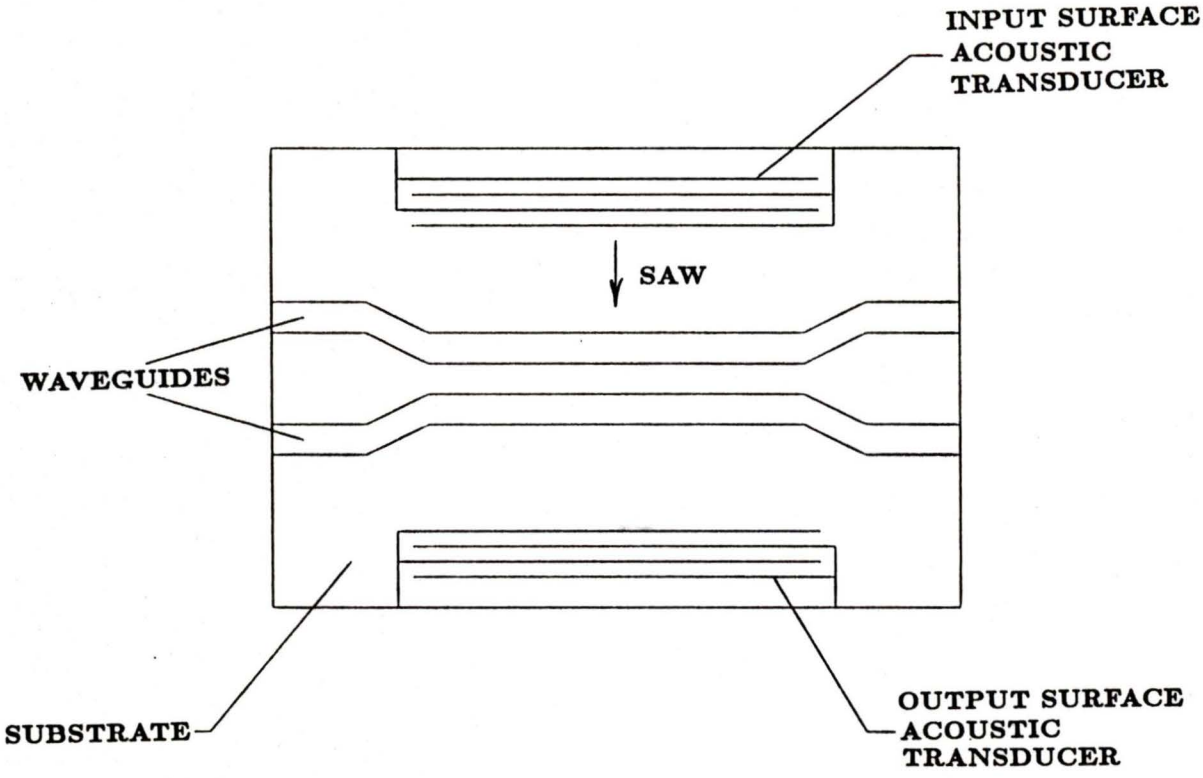

Figure 1.4: Acoustooptic switch.

Holographic Switching

Basically an optical projection device, holographic gratings are used to redirect the incoming light to the appropriate output port [37,38].

A coupling hologram is first produced by matching the light portals of the hologram with various output fibres. A deflection hologram is then constructed of elementary holograms placed in the optical beam path via in plane-translations of the hologram. As the deflecting hologram is rotated, an optical channel is opened to each of the output fibres. Such devices have low insertion loss and hence large matrices can be constructed. However, the hologram must be produced in a laboratory environment and would be difficult to manufacture commercially. Alignment of the elementary holograms and coupling hologram must also be precise.

Thermooptic Switching

Changes in the index of refraction due to temperature variation for use in a switch was observed by Miller et al [39] in 1966.

With a similar structure to the electrooptic switch (See Figure 1.5) , heaters can be attached to the waveguide to produce the necessary temperature increase (100° C) for the change in the index of refraction and hence switching to take place [40]. Such a device has been fabricated with an insertion loss of only 1.1dB and a crosstalk figure of $<$ -13dB.

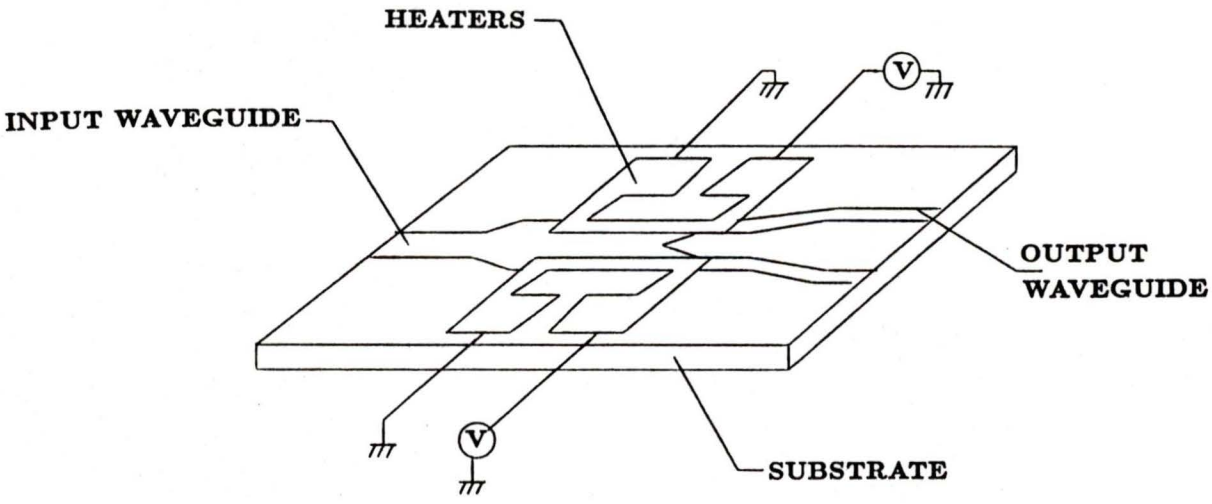

Figure 1.5: Thermooptic switch with one input waveguide and two output waveguides.

1.3 Summary

Research into an economical and optimum solution for a wideband switching system continues at a hectic pace. Optical switching, aside from the speed advantage, offers a more flexible means of designing communications systems.

Research into semiconductor wideband switches continues with recent promising results [41,42], but these devices cannot approach the high switching speeds available in an optical system.

With its good crosstalk figures, high switching speeds and the availibility of longer wavelength components and measuring equipment, an optoelectronic switch was chosen as the subject for this thesis.

Possible applications such as that to standby (backup) switching for long distance telephone trunk lines operating at gigabit rates and phased array antennas for SS/TDMA (Satellite Switched/Time Division Multiple Access) systems were also taken into consideration in selection of the topic.

Chapter 2

Design and Construction

2.1 Introduction

One of the goals of a fibre optic systems engineer is to design systems where the optical signal will travel longer distances without the need to regenerate the signal.

The first installed fibre optic systems were constructed of multimode fibre cable using short wavelengths ($\lambda = .85\mu m$) light sources (LEDs or lasers) and silicon photodiodes. These typically operated over a distance of less than 10km without the need to regenerate the signal. With the advent of single mode fibre cables, and longer wavelength lasers and photodiodes, these distances increased.

From the spectral loss characteristics of single mode fibre cable designed for minimum dispersion at $1.3\mu m$ in Figure 2.1 [43], it can be seen that there are two wavelength regions where the loss in the single mode fibre is lowest, $1.3\mu m$ and $1.55\mu m$. By proper doping of the silica cores,

the dispersion curve can be shifted to a minimum at $1.55\mu m$ (See Figure 2.2). Light sources and photodetectors which operate in this region are now being manufactured commercially and $1.55\mu m$ fibre optic systems are currently being implemented in many telecommunications long distance trunk lines.

Previous optoelectronic switches have been constructed using devices at $\lambda = .85\mu m$ [21] and $\lambda = 1.3\mu m$ [23]. The switch proposed in this thesis uses devices which operate in the $1.55\mu m$ wavelength region and dispersion shifted single mode (DSSM) fibre cable with minimum loss measured at $\lambda = 1.55\mu m$. In this chapter, the design and construction of an optoelectronic broadband matrix switch is described. The characteristics of each component are discussed and results of various measurements given. These measurements show the advantages and limitations of such a switch when used as a component of a fibre optic network.

2.2 Laser Diode

A $1.55\mu m$ InGaAsP double heterostructure (DH) ridge waveguide laser is used as the optical signal source. The optical cavity is formed by cleaving the semiconductor wafer perpendicular to the DH plane. Optical feedback occurs at the InGaAsP/air interface which has a high reflectivity arising from the differences in indices of refraction for InGaAsP and for

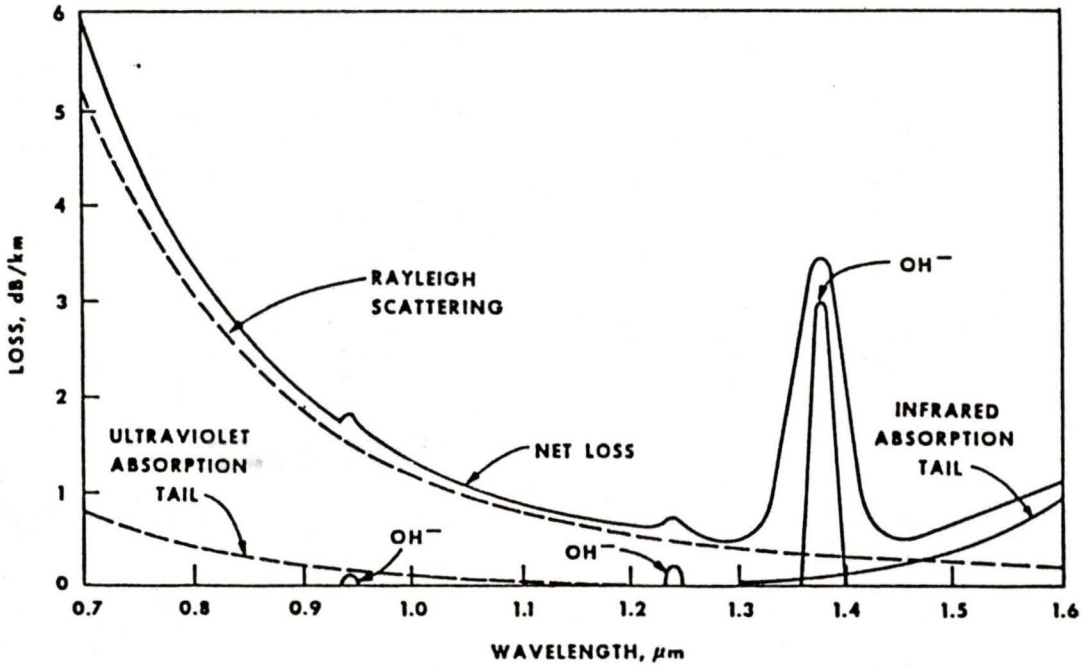

Figure 2.1: Spectral loss characteristics of single mode fibre cable designed for minimum dispersion at$\lambda = 1.3\mu m$.

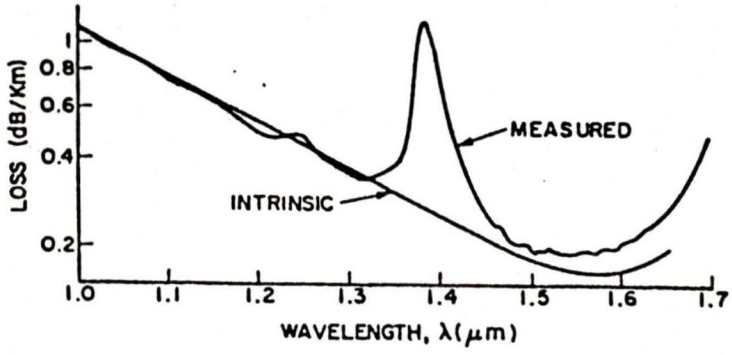

Figure 2.2: Spectral loss characteristics of single mode fibre cable designed for minimum dispersion at$\lambda = 1.55\mu m$.

air. As the injection current increases above threshold, the cavity gain is sufficient to overcome the losses, and laser oscillation results. A stripe geometry is used to confine the current flow to a narrow width. In the ridge waveguide, the stripe width is determined by the width of the laser ridge which is approximately 6 μm. The layer geometry of this device is given in Figure 2.3 [44,45] showing the active InGaAsP region between the two InP

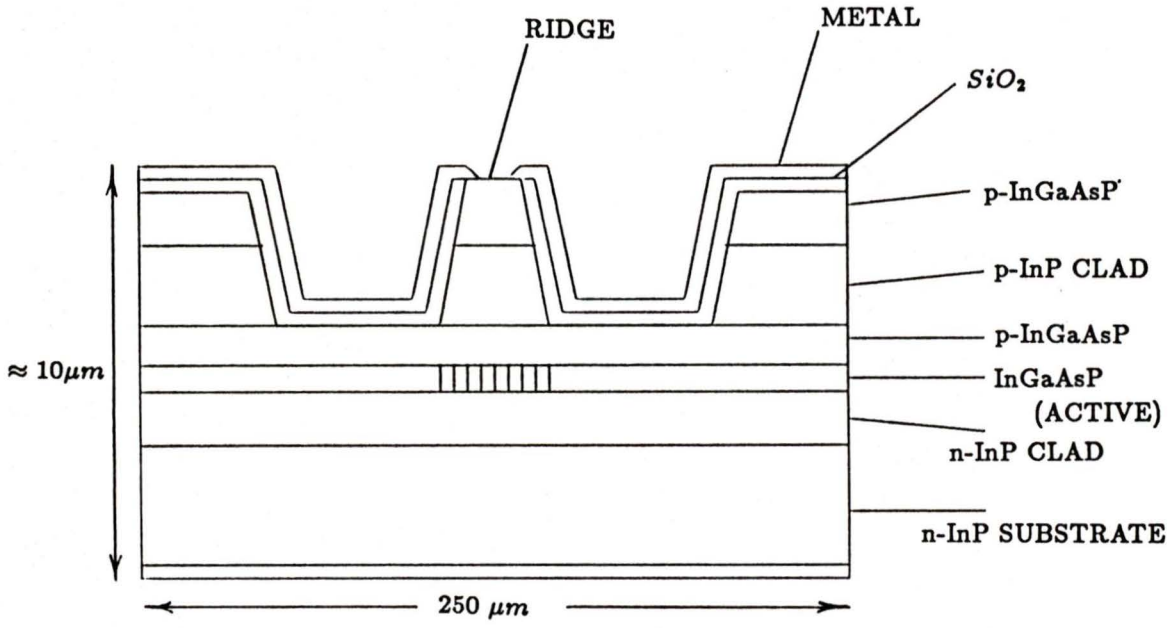

Figure 2.3: Layer geometry of InGaAsP double heterostructure ridge waveguide laser.

substrates forming the two heterojunctions. The conduction and valence band diagrams are shown in Figure 2.4 [45] .

For this device, the optical field is controlled in the transverse di-

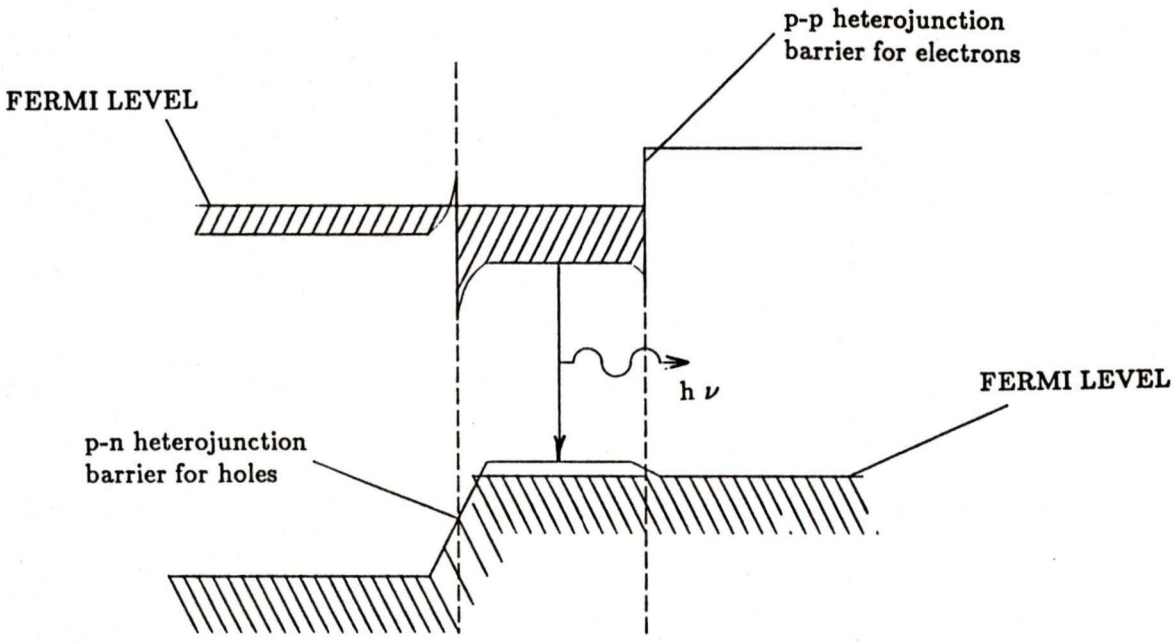

Figure 2.4: Conduction and valence band diagram of the double heterostructure laser.

rection by the injected carrier profile and is said to be gain guided. The transverse direction is perpendicular to the optical cavity direction. Called the fundamental transverse mode, this type of operation sometimes results in non-linearities in the optical output characteristics.

The characteristics of the laser are given in Table 2.1 where ϕM is the minimum peak power at 2 Amps, t_w is the pulse width and prr is the pulse repetition rate. The leakage current represents a dc current which bypasses the active region.

Type	Peak Curr. i_F A	Power ϕM Min. mW	t_w μs	prr kHz	Resp. Time t_r ns	Leakage Current nA
InGaAsP 1550nm No. C86052E	2	4	1.0	10	<1	1

Table 2.1: Diode lasers, typical characteristics, T = 27°C

2.3 Modulating the Optical Signal

To directly modulate the $1.55\mu m$ InGaAsP laser, the threshold current must be found to determine the operating point. By using the experimental arrangement shown in Figure 2.5, a plot of power output vs. current was generated as shown in Figure 2.6. From this graph, the bias current can be chosen as 630mA. The Photodyne XT17 power meter measures op-

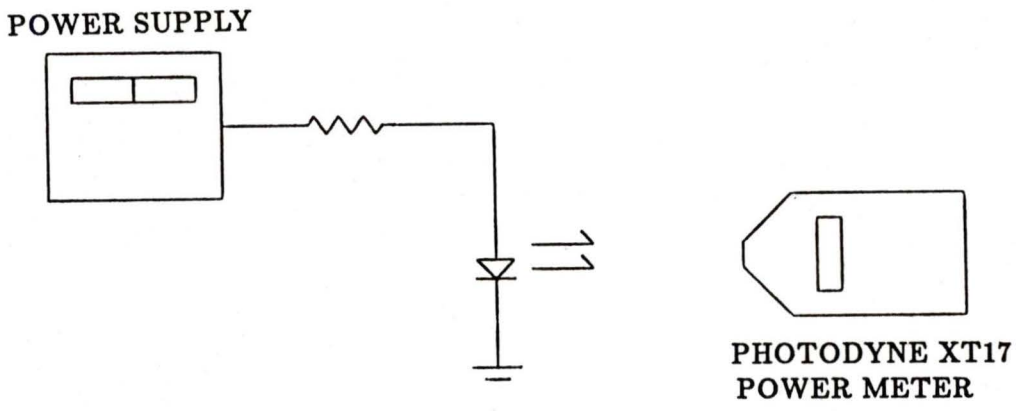

Figure 2.5: Measurement of power output vs. current.

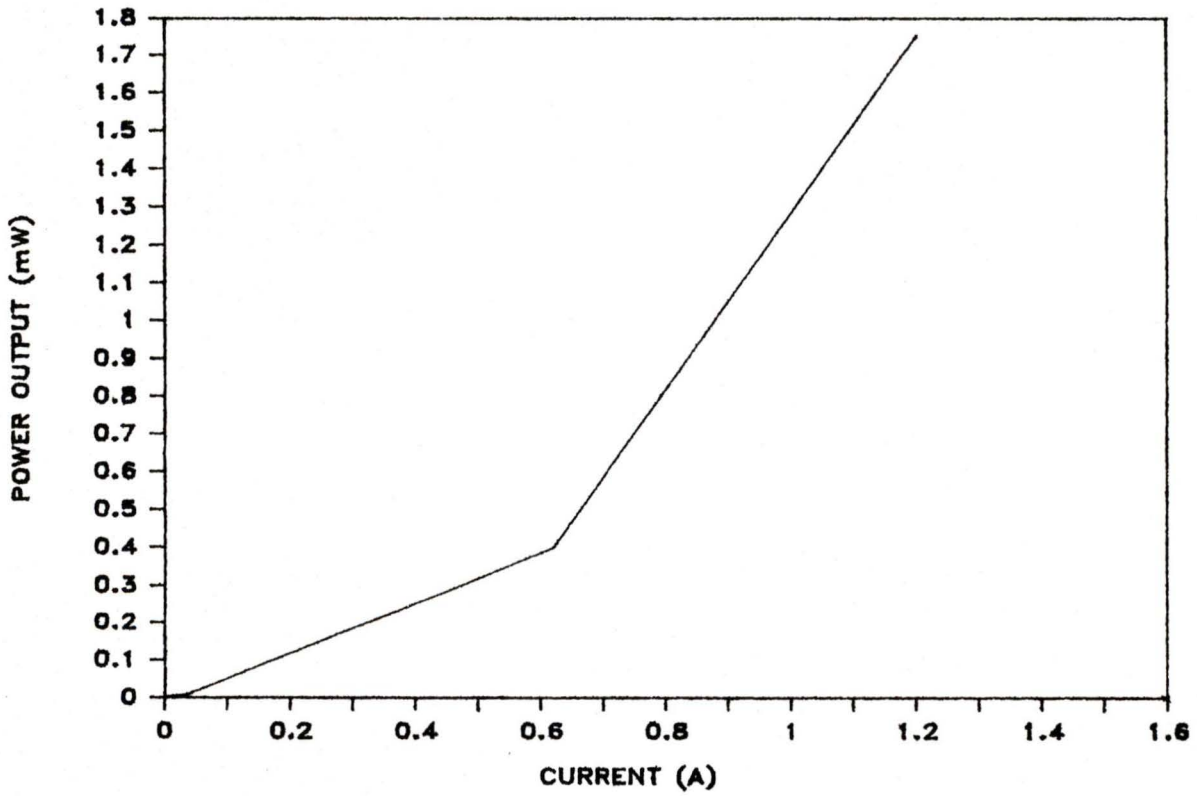

Figure 2.6: Power output vs. current for the InGaAsP ridge waveguide laser.

tical power in mW where 0mA is the reference point for 0mW. This unit is calibrated for maximum sensitivity at $\lambda = 1.55\mu m$ [46].

An HP8350B sweep oscillator under control of an HP8757A Network Analyzer provides the modulated signal. The modulator drive supplies a $\pm$ 2.2V square wave into 50 ohms with symmetry of 50/50 $\pm$ 1%. The output of the sweep oscillator is coupled through a $.05\mu F$ capacitor and a 47Ω resistor and is combined by a bias T with a 630 mA bias current and a 27Ω resistor to the anode of the laser [47]. The cathode is connected to ground (See Figure 2.7).

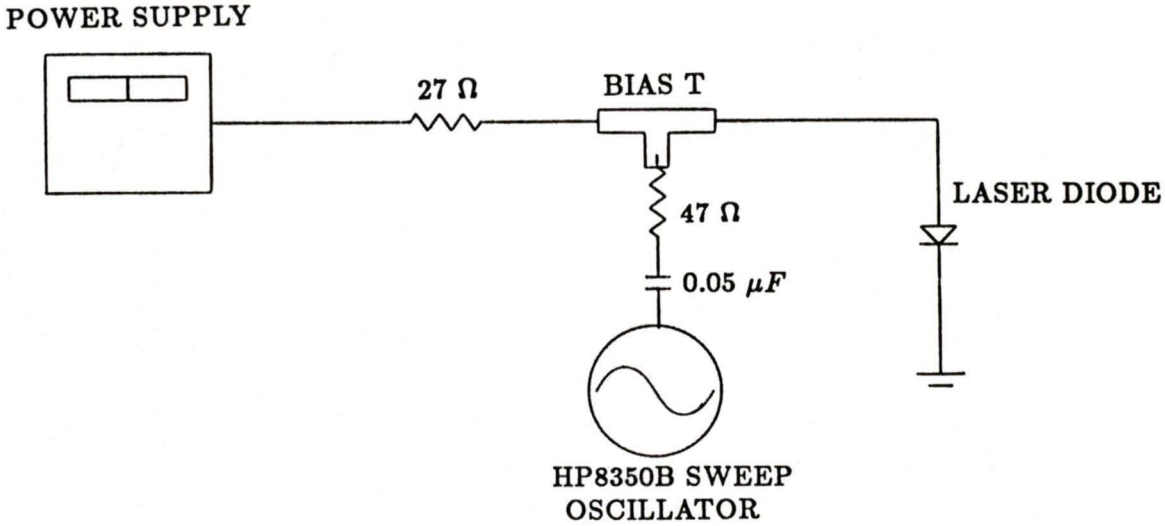

Figure 2.7: Equipment configuration for the modulation of the optical signal.

2.4 Fibre Optic Cable

A fibre optic cable consists of a core and cladding region typically made of silicon glass. For multimode fibre cable, the core diameters are 10 to 20 times larger than those of single mode fibre cable and hence more modes propagate through the fibre waveguide. For single mode fibres whose core diameters range from 5 to 15 μm, only a single mode propagates through the fibre waveguide.

As the optical signal pulse propagates along the fibre, it tends to spread out over time and overlaps other transmitted pulses. Graded Index multimode fibres have a core whose index of refraction is highest at the centre of the core and tapers off parabolically towards the edge of the core. The pulse dispersion effect is reduced in Graded Index multimode fibre and in single mode fibre.

Typical light sources emit over a range of wavelengths which can propagate at different speeds down the fibre. This effect, called chromatic dispersion can be characterized by the variation in delay (ps/km) with respect to wavelength change (nm) and has the units of ps/nm $\cdot$ km.

The optical fibre pigtails of the laser diode and photodiodes and the 1×2 optical splitters are dispersion-shifted-single-mode (DSSM) fibre manufactured by Corning Glassworks. The characteristics of the test fibre are shown in Table 2.2 where $1550nm$ is the wavelength where the minimum chromatic dispersion occurs. The maximum average attenuation is due to

absorption and scattering effects.

Product SMF/D3	Coating CPC3
Chromatic Dispersion Min. Wavelength	$1550 \pm 10nm$
Slope of Chromatic Dispersion Around Minimum	$\leq .75ps/nm^2 \cdot km$
Maximum Chromatic Dispersion in Transmission Window (1520-1580nm)	$< 3.0ps/nm \cdot km$
Maximum Average Attenuation	$< .22dB/km$
Core Refractive Index	≈ 1.47
Cladding Refractive Index	≈ 1.452

Table 2.2: Characteristics of test fibre.

2.5 Fibre Optic Couplers

The optical fibre couplers are manufactured by Opto-Electronics Inc. The couplers are fabricated using the fused taper technique. The two fibres are stripped of their coating and cladding in the coupling region and thoroughly cleaned. The fibres are combined and twisted, then fused and tapered with a suitable heat source. The transmitted and coupled power is continuously monitored and the tapering process ceases when the desired coupling or splitting ratio is obtained. The characteristics of the couplers are shown in Table 2.3.

Product FS-10-1550-1	
Nominal Splitting Ratio (P_2/P_3) Port 1 Input	1
Measured Splitting Ratio	$.9 \pm .1$
Measured Excess Loss	$\leq$ 1.5 dB
Taper Length	15mm $\pm$ .5 %
Taper Core Diameter	$2.51\mu m \pm$ .5%

Table 2.3: Characteristics of the optical fibre splitter.

2.6 Matrix Construction

The laser's fibre pigtail was fusion spliced to the 1 $\times$ 2 directional coupler which in turn was fusion spliced to a second and third coupler to produce a 1 $\times$ 4 split. The 4 InGaAs/InP photodiode pigtails were spliced onto the directional coupler ends. This process was repeated to produce the second 1 $\times$ 4 matrix. A block diagram of the matrix switch is shown in Figure 2.8

All fusion splices were produced using the NT6F22A fusion machine which uses an optical power maximization technique to minimize splice loss. In this method, the two fibre cables to be spliced together are mechanically stripped of any coating material to leave approximately 4cm of bare fibre. The fibres are then cleaved to produce a 90^0 end face. The two fibre ends to be fused are placed in the jaws of the fusion machine and their ends are butted together. A section of one of the fibres, approximately 20cm from the cleaved end is placed in the launch module. The mechanism of the launch module puts a bend into the fibre cable and light is injected into

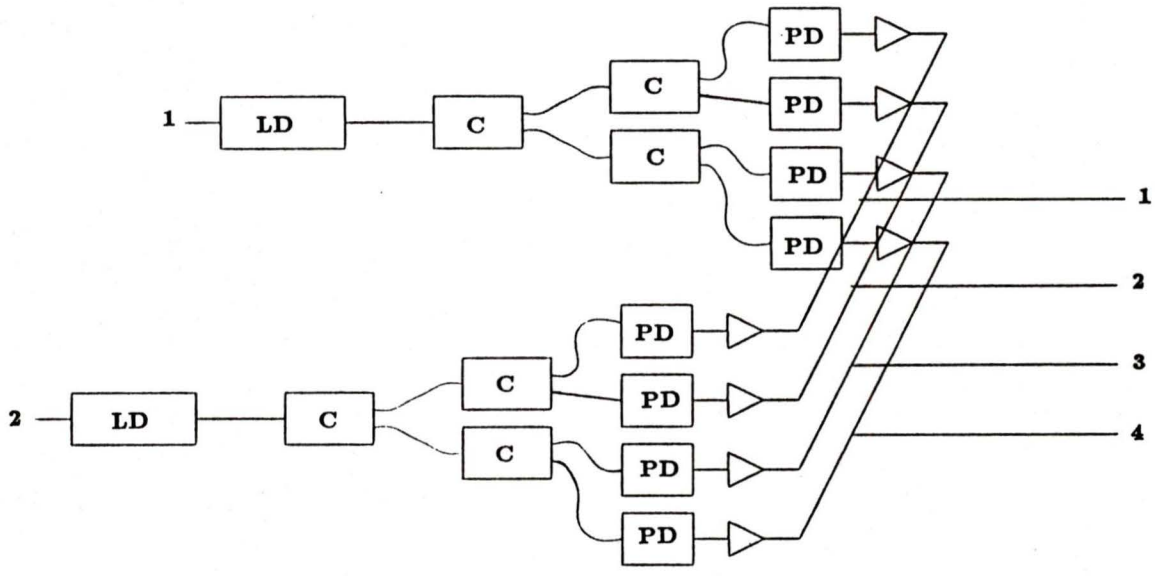

Figure 2.8: Block diagram of the 2 × 4 matrix switch. LD is the laser diode; C is the fibre optic coupler; PD is the photodiode.

the fibre cable through the bend. A section of the second fibre is placed into the detector module at the same distance. The detector module also bends the fibre cable and detects the light propagating out of the fibre at the bend. Light is launched into the first fibre by the launch module and is received by the detector module. By repositioning the two butted fibres appropriately, a maximum optical power can be detected by the detector module. When this point is established, the two fibres are fused together. The experimental arrangement is shown in Figure 2.9.

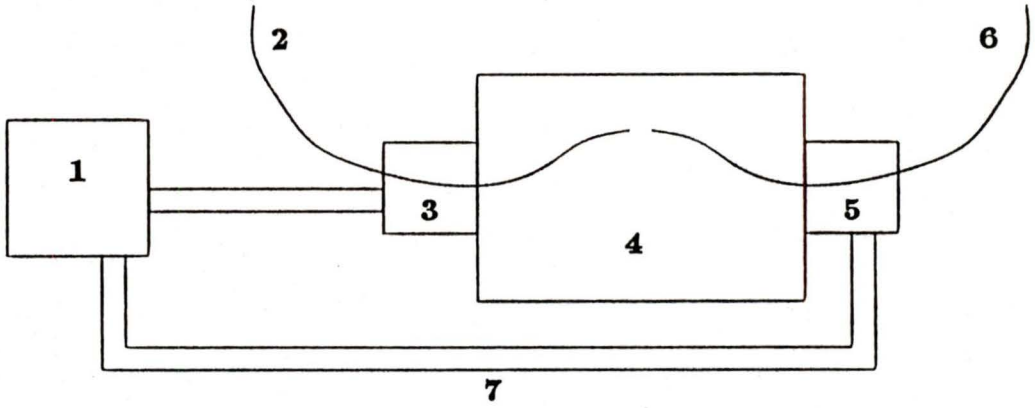

Figure 2.9: Equipment configuration for fusion method used. 1)NT7L1055 Power Optimizer; 2 & 6)DSSM fibre to be fused; 3)NT7L1025 AR Launch Module; 4)NT6F22AA Fusion Machine; 5)NT7L1075 AR Detect Module; 7)Electrical Connection

2.7 Photodiodes

InGaAs/InP pin photodiodes are used as the switching and receiving devices. The layer geometry of this device is shown in Figure 2.10 [48,49] with the energy band structure shown in Figure 2.11 [45] . The character-

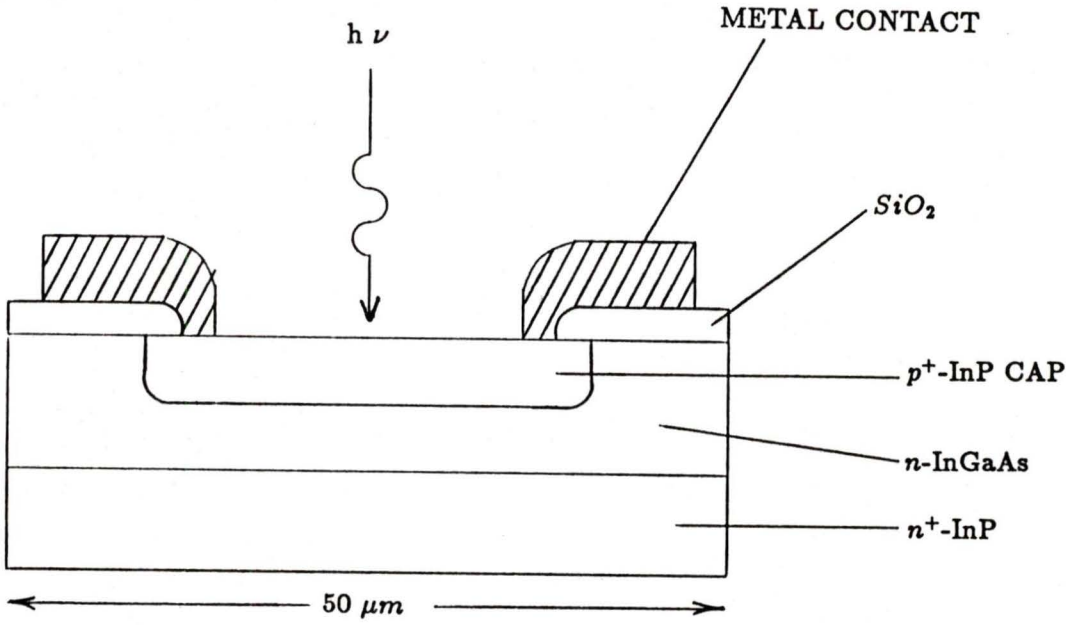

Figure 2.10: InGaAs/InP photodiode layer geometry

istics of the photodiode are given in Table 2.4.

When the incident light from the laser falls onto the photosensitive area of the diode, carriers are generated. At zero bias, the energy barrier between the p doped InP and the n doped InGaAs reduces the responsivity of the diode by preventing the flow of the photocurrent. At reverse bias, this barrier is lowered and the responsivity is increased.

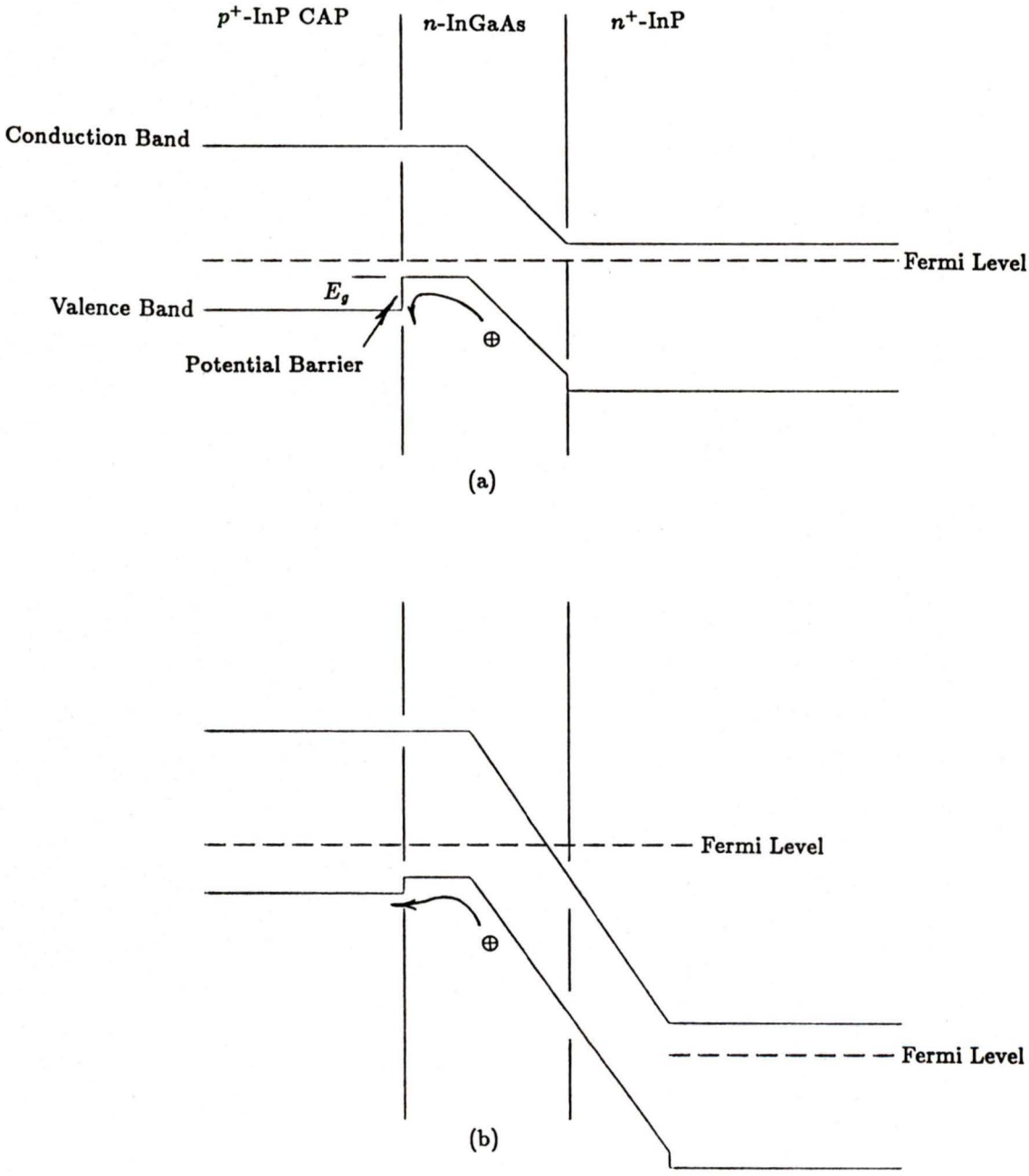

Figure 2.11: InGaAs/InP photodiode energy band structure. (a) Zero bias (b) Reverse bias. ⟵ ⊕ is the direction of the photocurrent.

2.8 Switching Circuit

By controlling the bias on the InGaAs/InP photodiode, the modulated signal from the laser source can be switched on and off. Reverse biasing the photodiode by applying a negative voltage across the device places it in the on-state and zero biasing the photodiode places it in the off-state.

From the characteristics of bias voltage vs. capacitance for the InGaAs/InP photodiode given in Figure 2.12, a constant value of less than .6 pf is reached for biases above 5 Volts. The on state reverse bias voltage is chosen at 10 Volts to be sure that the device is operating in the region of high responsivity and lowest capacitance.

An SN5836 high speed switching transistor was chosen to switch the photodiode between reverse and zero bias. The characteristics of the device are given in Table 2.5. Vceo is the collector emitter voltage, I_c is the collector current and hFE is the forward transverse current ratio.

When the photodiode is at zero bias, the responsivity is maintained but at a lower efficiency. The switching transistor is placed in series with the photodiode to open circuit the photocurrent path at zero bias.

The switching transistor was switched with a 12V, 30ns pulse and the D-MOS FET was turned on by a 10V 8ns pulse. The configuration

Type	Photo. Sens. Surface Dia.	Responsivity Reverse Bias		Dark Curr. I_d	Spectral Noise Curr. Dens.	Cap C_d (100 kHz)	Resp. Time t_r
		At 1300 nm	At 1550 nm				
	mm	A/W	A/W	nA	$pA/Hz^{1/2}$	pf	ns
InGaAs/InP No. C30979EQC	.05	.60	.70	15	.2	<1	<1

Table 2.4: Photodiodes, typical characteristics, T = 22°C, bias voltage = 5 Volts

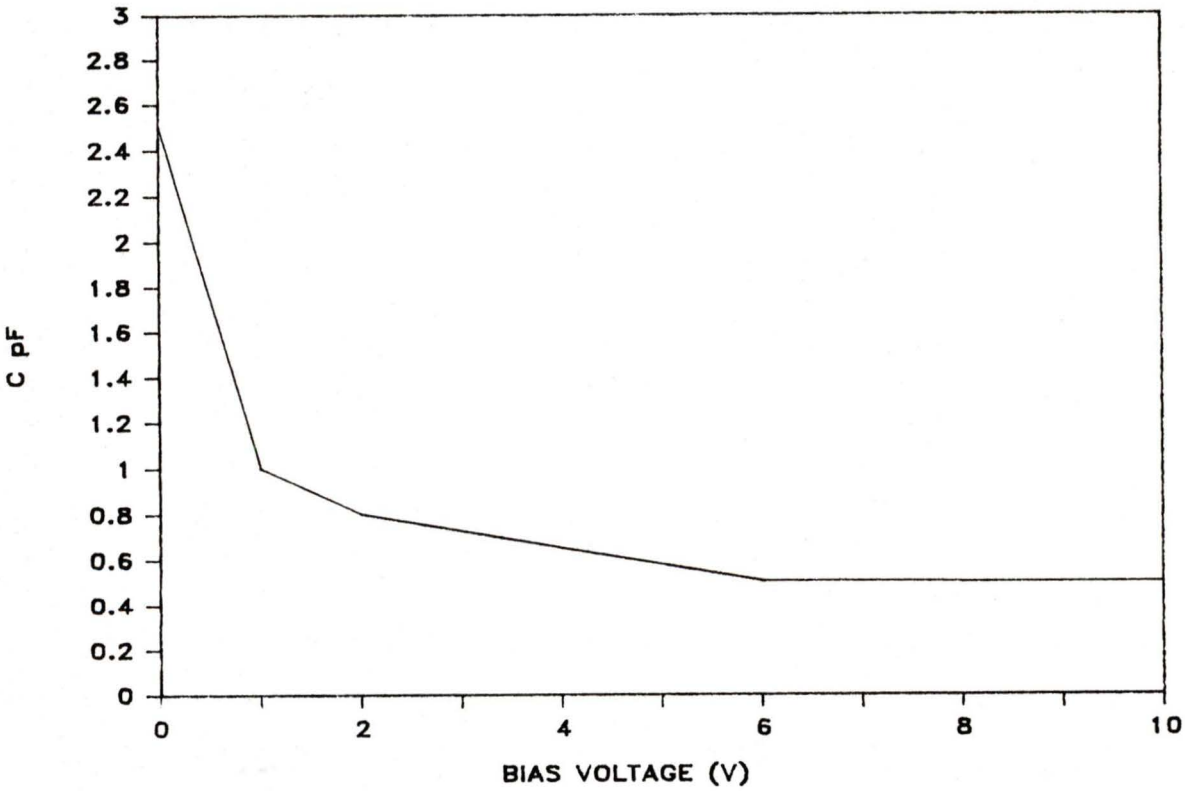

Figure 2.12: Reverse bias voltage vs. capacitance for the InGaAs photodiode

is shown in Figure 2.13 [50]. The switching transistor was driven between cutoff (the off state) and saturation (the on state). The D-MOS FET was used to provide a low resistance path to ground for the photodiode capacitance to discharge.

2.9 Receiver Circuit

For a practical system analysis, the pin/FET combination receiver provides optimum performance at long wavelengths and low power signals (e.g. -30dBm). To achieve similar results obtained by using avalanche photodiodes, two RCA receiver assemblies, model no. C306XX-034 were used to produce the best values in measuring the output signals from the photodiodes. A schematic of this receiver is shown in Figure 2.14.

Motorola MWA 310 hybrid buffer amplifiers were used at the output of the photodiodes to protect the receiver circuitry from the off state short circuit of the switching assembly. These amplifiers have a frequency bandwidth of 1200MHz at unity gain. The signals from the buffer amplifiers

NPN Type	Vceo	I_c mA	hFE Min.	IT MHz	T on/ns T off/ns
2N5836	10	200	25	2000	320ps-

Table 2.5: Highspeed switching characteristics of SN5836

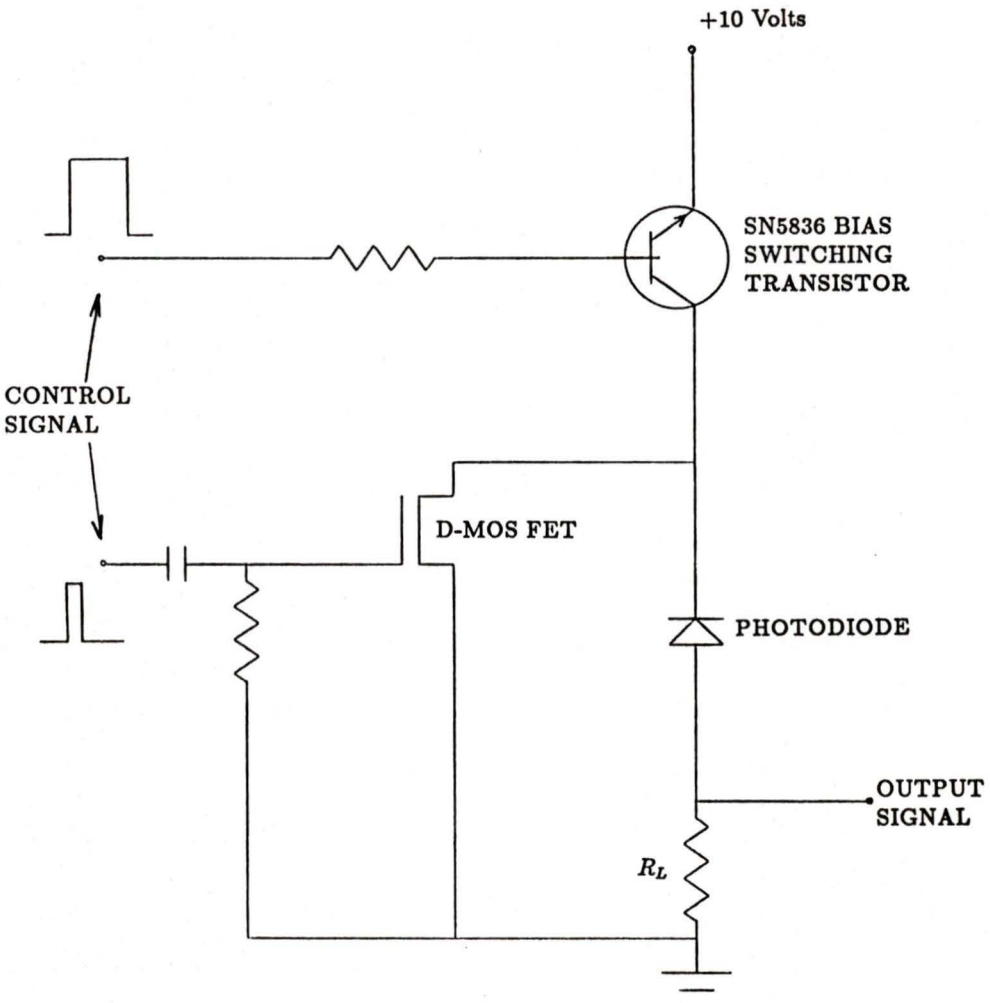

Figure 2.13: Switching circuit with photodiode.

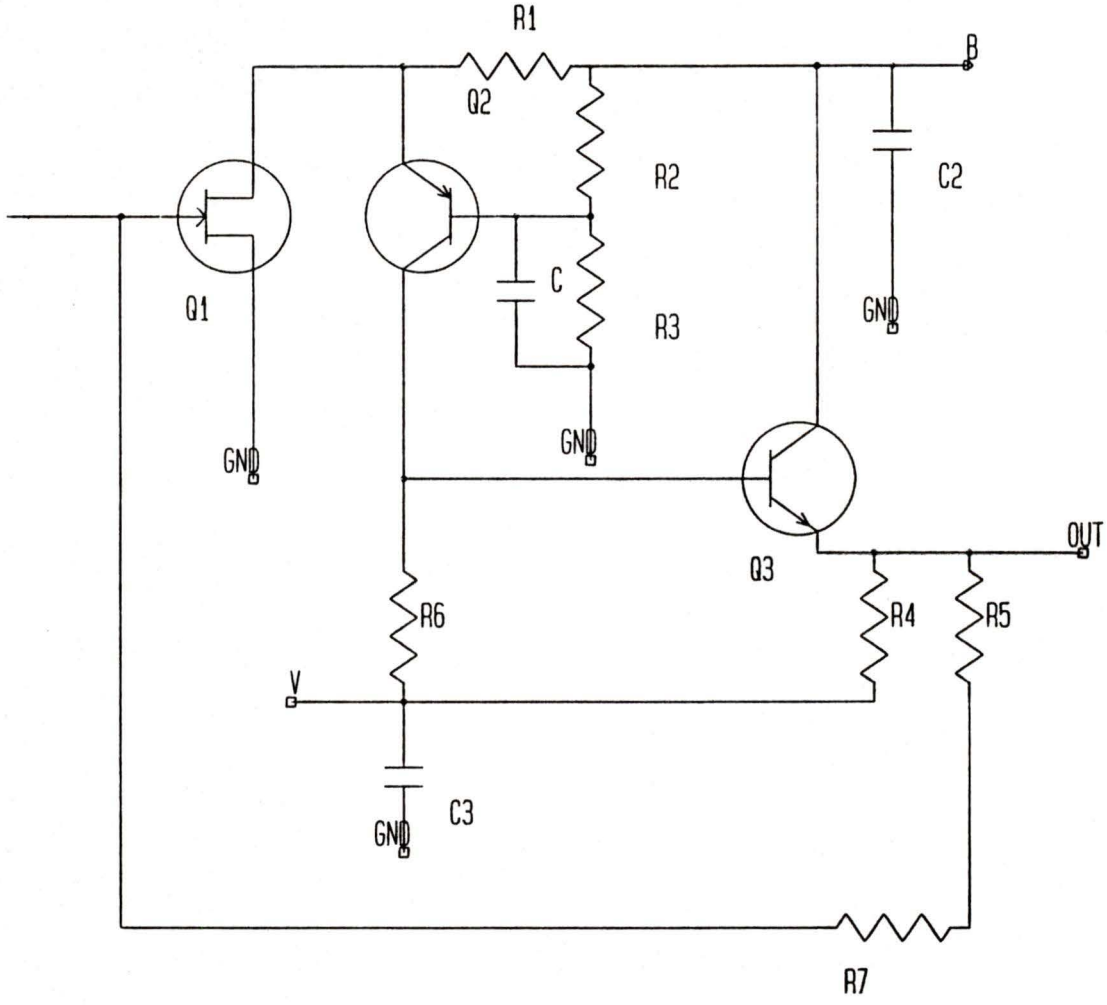

Figure 2.14: RCA receiver circuitry.

were then summed using coax cable and T connectors to produce 4 output lines.

All switching and buffer circuits were constructed using printed circuit boards and were shielded in metal cases. Wiring distances were kept as short as possible to avoid RF crosstalk. Special pins were provided so that the photodiode can be removed easily for different measurement purposes. A picture of the completed 2 × 4 switch is shown in Figure 2.15.

With the photodiodes reverse biased, the modulation circuitry is activated with the resulting transmit and receive pulses shown in Figure 2.16.

2.10 Measurements

Insertion loss, which is a combination of the splice and coupler losses was measured during construction. Throughput power P_o was measured by the Photodyne XT17 power meter at the end of the last coupler. The laser pigtail fusion splice was then broken and a new end face was prepared. The power output of the reference pigtail was measured and the total loss calculated from

$$dB = P_i - P_o \tag{2.1}$$

where P_i, P_o = *log units* (dBm)
and P_i *is the laser diode output power from its pigtail.*

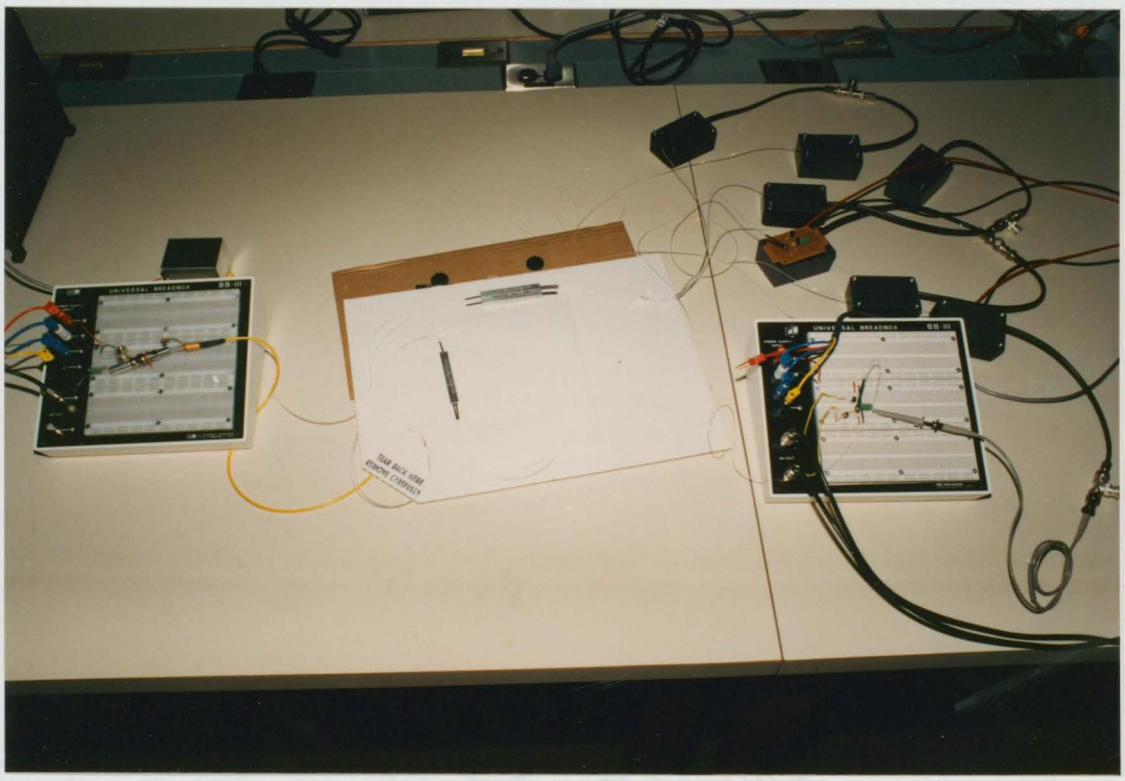

Figure 2.15: Completed 2 × 4 optoelectronic matrix switch. To the left are the laser diodes and associated modulation circuitry. In the center are the fibre optic splitters and to the right are the 8 photodiode switching circuits.

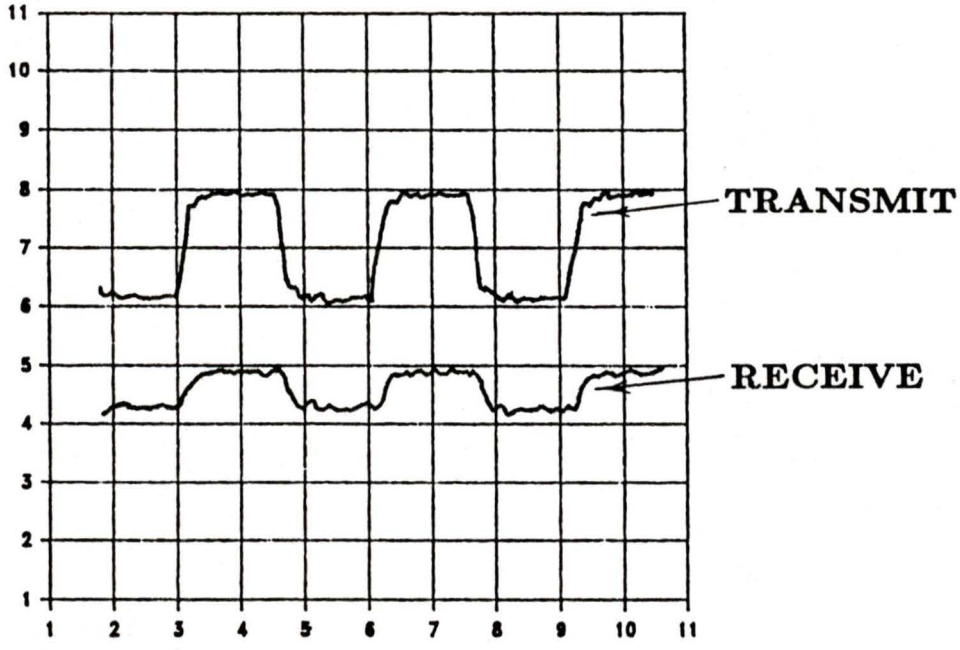

TRANSMIT
VERT. = 1V/DIV
HOR. = 1ns/DIV

RECEIVE
VERT. = 100mV/DIV
HOR. = 1ns/DIV

Figure 2.16: Transmit and receive pulses of optoelectronic switch.

The results of the loss measurements are shown in Table 2.6 and Figure 2.17.

Isolation (on-off power ratio) and frequency response is measured

Measured	
Mean	Standard Deviation
4.17dB	.24dB

Table 2.6: Measured value of splice and coupler losses for the 8 output lines from the couplers.

using an HP8757A Network Analyzer with an HP8350B Sweep Oscillator and HP11664A detector. The HP11664A detector has a frequency range of 10MHz to 18GHz and a dynamic range of 76db. The experimental arrangement is shown in Figure 2.18.

The oscillator sweeps from 0 to 1.2 GHz and the response is stored in the network analyzer. An HP7090A plotter is connected through the HP-IB bus to the network analyzer. The optical output power response for the on and off states is plotted in Figure 2.19. It can be seen that at high frequencies (860MHz), the isolation is approximately 69dB which is more than adequate for digital signals which normally require at least 30dB. In the off-state, the photocurrent is limited by the leakage current of the transistor.

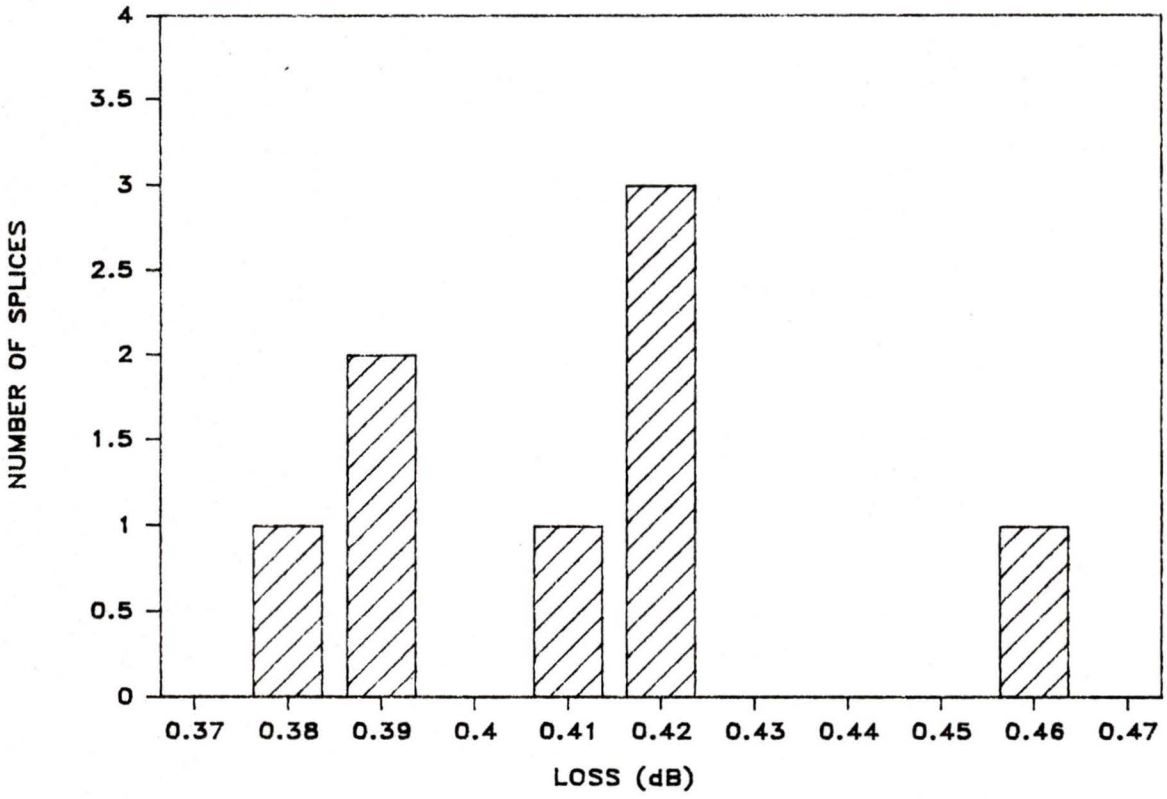

Figure 2.17: Loss analysis of 8 output lines from the couplers.

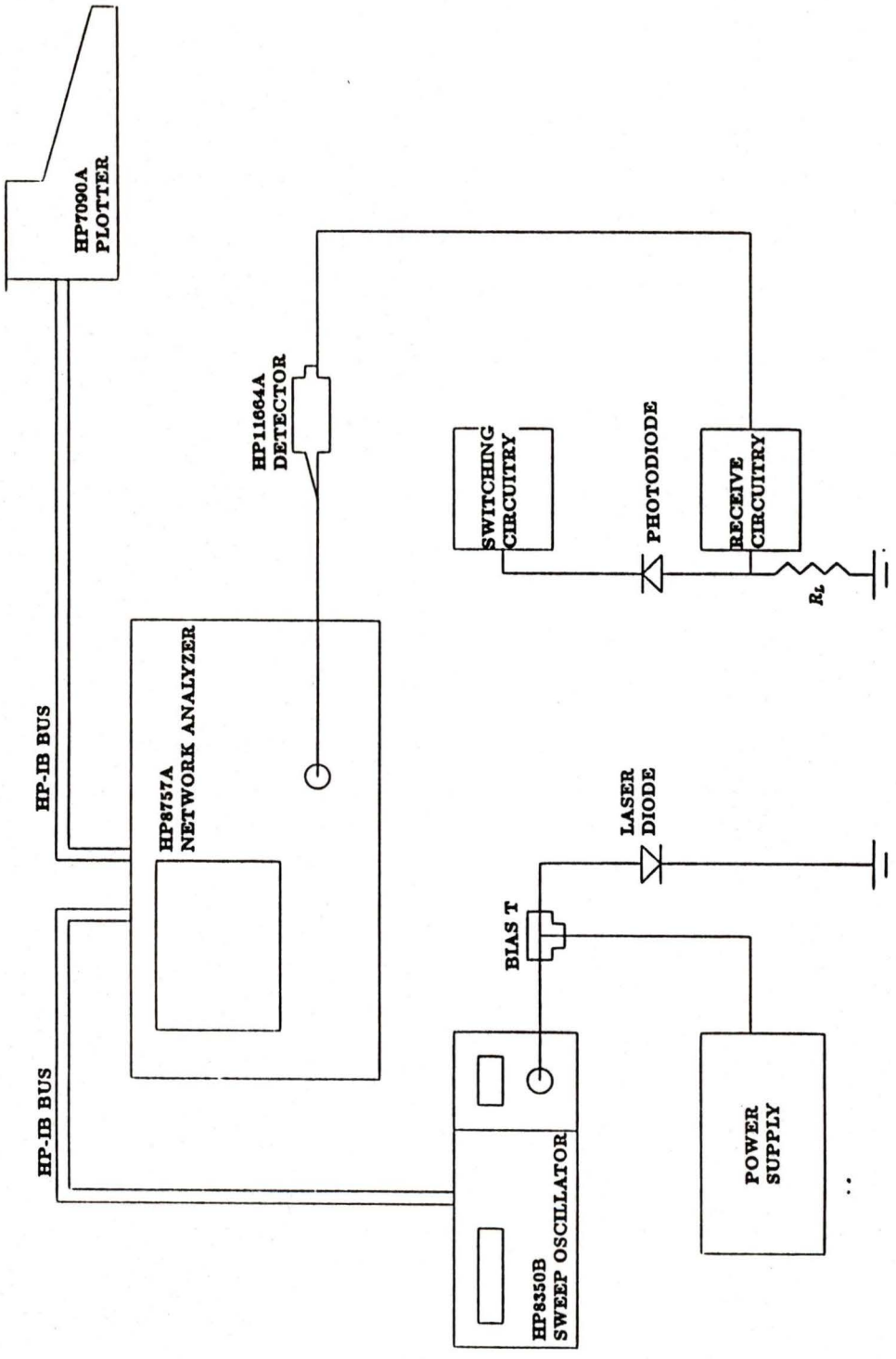

Figure 2.18: Isolation and frequency response measurement configuration.

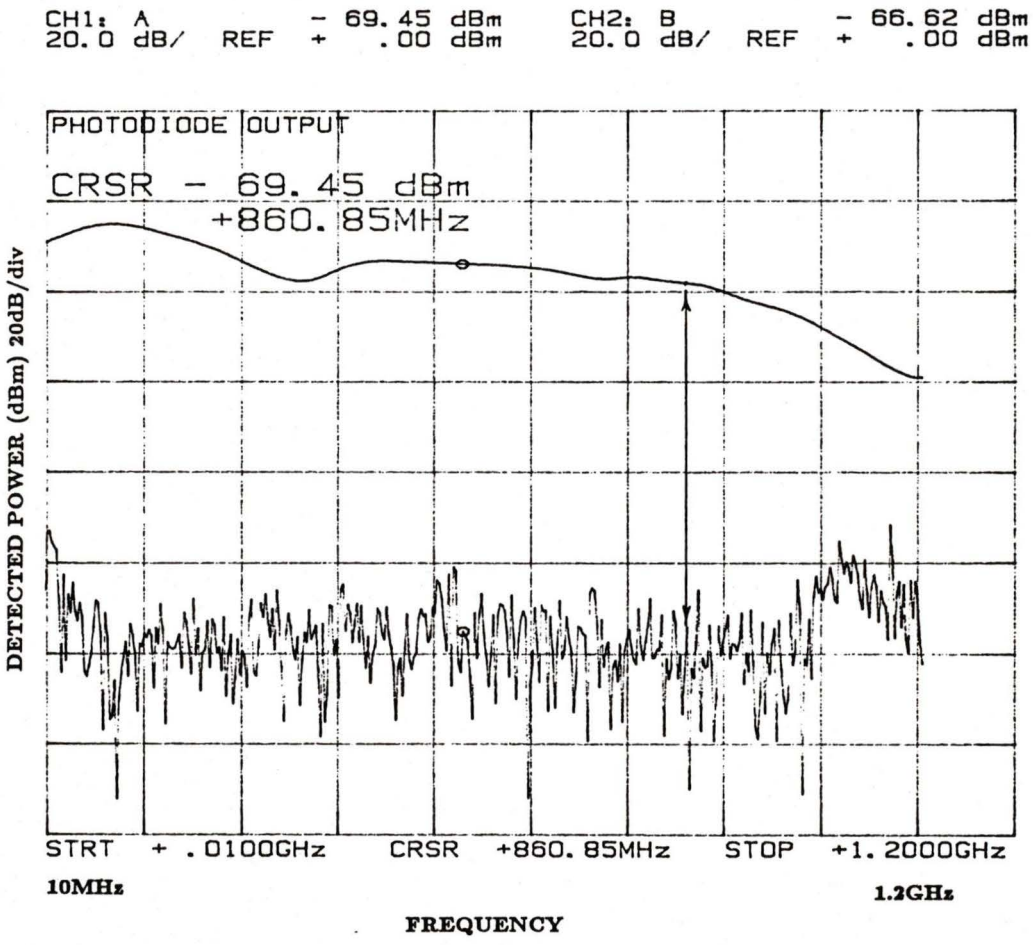

Figure 2.19: Isolation and frequency response of a single device. Incident optical power is .15mW; wavelength=1.55 μm;dc responsivity = .7 A/W. On-state bias = -10V; off-state bias = 0V.

2.11 RF Leakage and Ground Loops

The isolation results shown in Figure 2.19 were significantly worse than those achieved previously [26]. To reduce RF leakage (coupling, crosstalk), the output lines are shielded and separated while the laser and associated modulating circuitry are situated at such a distance from the receivers (approx. 15 metres) so as to be isolated. Line filters are added to the AC lines, and two banks of nicad batteries, each producing 10 Volts, are used to power two of the photodiodes and associated switching circuits. All the printed circuit board grounds were made common and decoupling capacitors to ground were inserted into power lines for the photodiode switching circuits.

An improvement in isolation of 11dB at 860MHz was observed and is plotted in Figure 2.20. The change in the high frequency response may be due to the added capacitance of the buffer amplifier, receiver circuitry or the D-MOS FET.

2.12 Switching Response

To measure the switching response times, the matrix switch is scaled down to a size of 1×2. The two RCA receiver assemblies are attached to the photodiode assemblies.

This configuration emulates an optical protection switch where if one

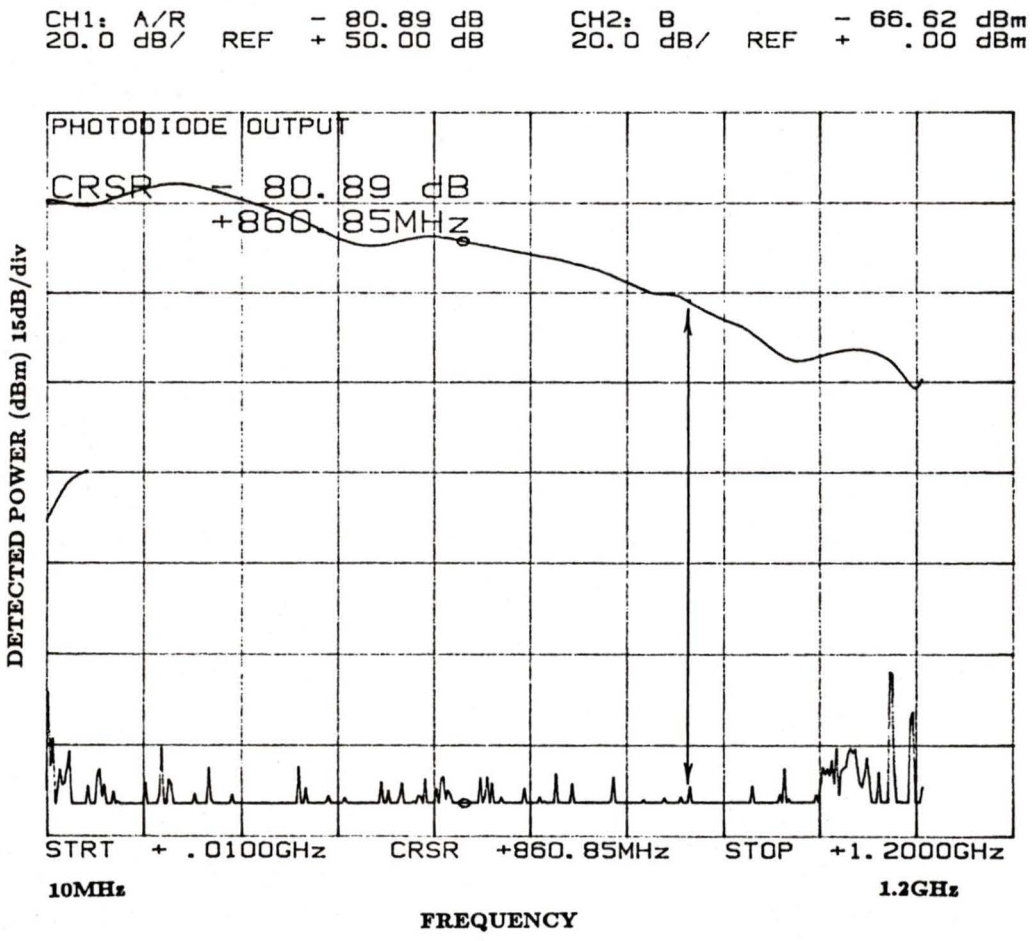

Figure 2.20: Isolation and frequency response of a single device. Incident optical power is .15mW; wavelength=1.55 μm; dc responsivity = .7 A/W. On state bias = -10V; off-state bias = 0V. RF leakage and ground loops improved

fibre of a communication system is broken or damaged, the system switches over to the second fibre.

A digital storage scope is used to observe the switching responses of the photodiode. The output of the receive circuitry is input to channel A while the output of the control signal is input to channel B. The turn off and turn on switching transients are shown in Figures 2.21 and 2.22 respectively. It can be seen that the turn off transient is 25ns and the turn on transient is 48 ns.

When the photodiode is at zero bias, a charge accumulates at the pn junction. When the device is switched from the off-state to the on-state, this charge must be dissipated. As a result, there is a delay in turning on the switch. The results support this statement. The limiting factors in switching times are charging and discharging of the diode capacitance.

2.13 Summary

In this chapter, the design and construction of a broadband optoelectronic matrix switch was presented.

The layer geometry and energy band diagrams of the InGaAsP ridge waveguide laser were presented and the principle of operation explained. The operating threshold current of the laser was determined by experimental measurement. Intensity modulation was used to produce the high

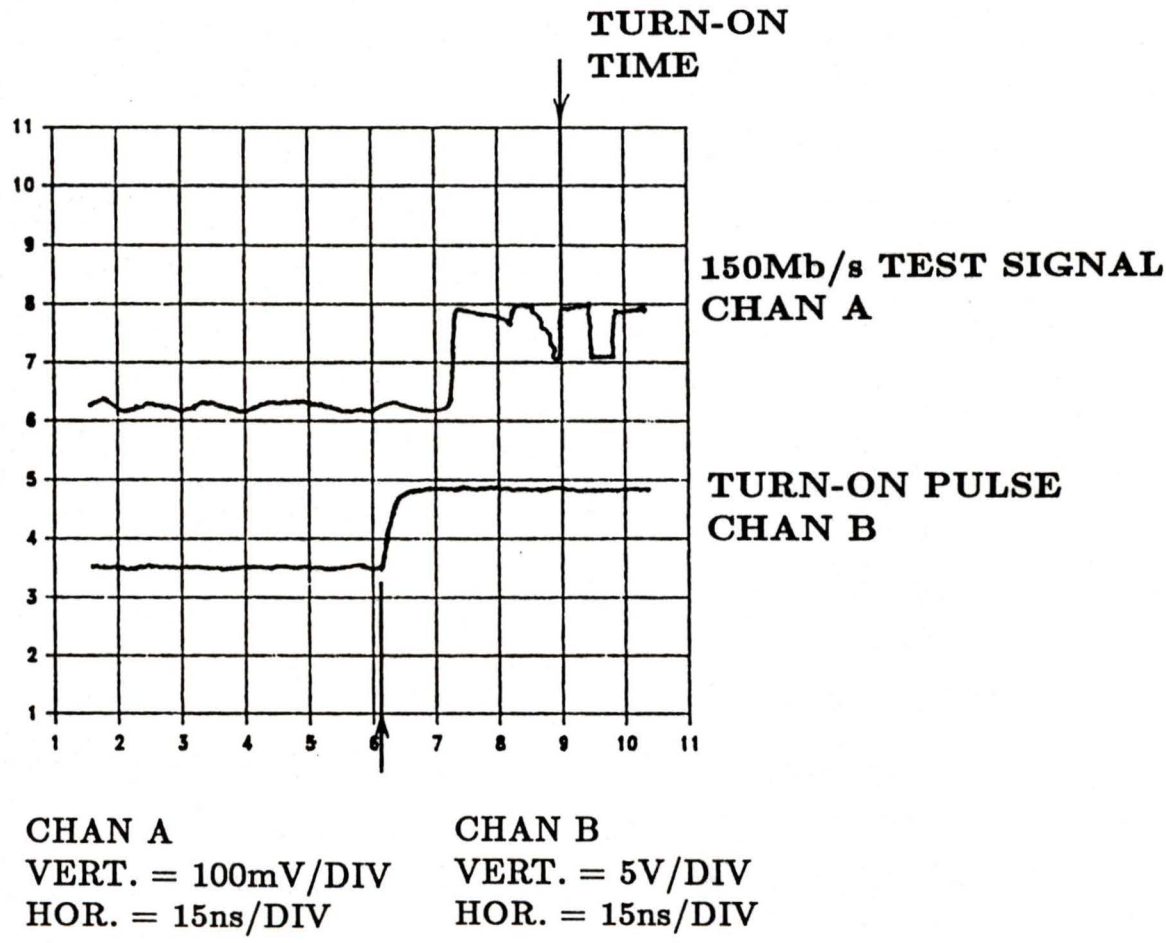

Figure 2.21: Turn on transient of 48ns

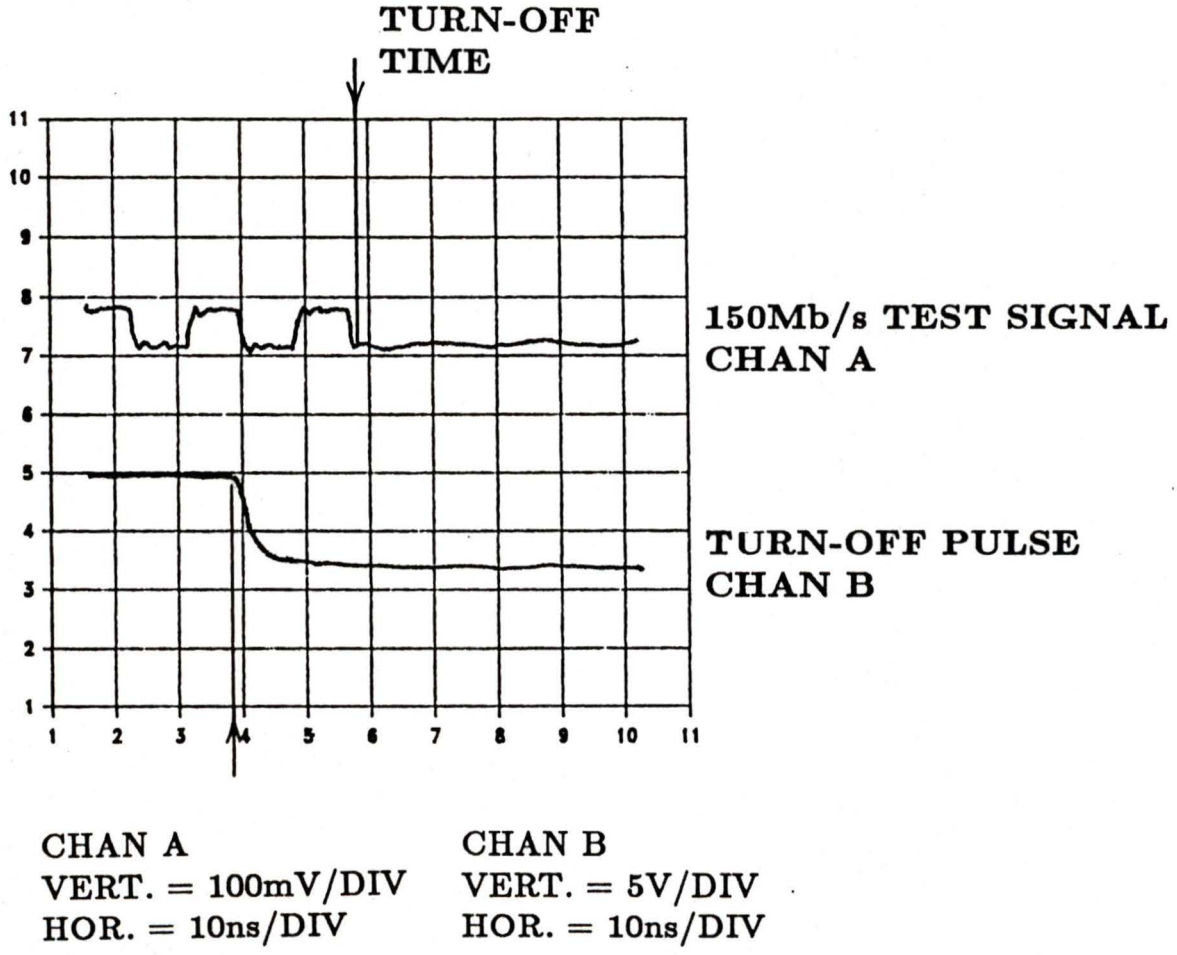

Figure 2.22: Turn off transient of 25ns

bandwidth optical signal.

The characteristics of the fibre optic cable and couplers were given with an explanation of the fusion technique used to fuse the optical cable.

The geometry and bandgap diagrams of the InGaAs/InP photodiodes were presented with an explanation of the operating principles. The switching and receiving circuitry were given and a complete working picture of the switch was shown.

Insertion loss was measured to be an average of 4.17dB $\pm$ .24dB for the 8 output lines from the couplers. Isolation was measured at 69dB at 860MHz before any corrective measures were taken to reduce RF leakage. An improvement of 11dB was obtained for a total isolation of 80dB when corrective measures were taken. Turn on switching response was measured at 48ns and turn off switching response was measured at 25ns.

Chapter 3

Analysis

3.1 Introduction

In the design of wideband optical switching systems, the most important parameters to be analyzed are insertion loss, isolation, frequency response and switching time. The isolation and frequency response determine the type and bandwidth of signal which can be switched. The insertion loss predicts the distances the signal can travel before it is necessary to regenerate the pulse and the switching time determines whether the switch can be used as a protection device.

In the previous chapter, the design and construction of an optoelectronic broadband matrix switch was described. The insertion loss, isolation, frequency response and switching time of the completed device were measured. In this chapter, these parameters are calculated using various models that describe the basic components of the switch.

3.2 Insertion Loss Analysis

The insertion loss in the matrix is a combination of the single mode splice and coupler losses. The actual attenuation due to fibre length is small with the relatively short distances involved in the construction of the switch.

3.2.1 Splice Loss

The ability to accurately model single mode fibre optic splices is important in the development of large scale lightwave communication systems. As prototype construction for these systems becomes more costly, computer simulation and mathematical analysis of the various splice loss mechanisms offers an alternative approach to hardware evaluation.

The characteristics of the dispersion shifted single mode(DSSM) fibre has been given previously in Chapter 2, Table 2.2. To analyze the DSSM fibre, the fundamental differences between DSSM and normal single mode fibres must be discussed.

DSSM fibres with $\lambda = 1.55\mu m$ can be fabricated by increasing the relative refractive index between core and cladding (Δ) and decreasing the core diameter, as compared to conventional ($\lambda = 1.3\mu m$) design.

Fibre designs with triangular core index of refraction profiles were found to exhibit the least loss and have been fabricated successfully. GeO_2 is used in doping the silicon core to shift the minimum dispersion curve from $1.3\mu m$ to $1.55\mu m$.

Basic Mechanisms

To develop equations for splice loss in DSSM fibre it is necessary to review the fundamental sources of splice loss for $1.3\mu m$ single mode fibre.

The three sources of monomode splice loss are as follows:[51]

1. Field width mismatch at the splice due to profile differences.
2. Lateral core displacement due to core concentricity.
3. Losses due to the splicing technique. As we are using fusion splicing, core deformation is the prominent loss mechanism.

Loss due to profile mismatch is small as all components are manufactured using the same Corning SMC-3 fibre optic cable.

Core concentricity and deformation can be modeled in terms of three components: longitudinal offset, angular tilt and lateral offset as shown in Figure 3.1.

With the fusion splicing technique used here, the ends of the fibre are butted together before they are joined. This virtually eliminates loss due to longitudinal offset and leaves angular tilt (α) and lateral offset (D) as the main sources of joint loss.

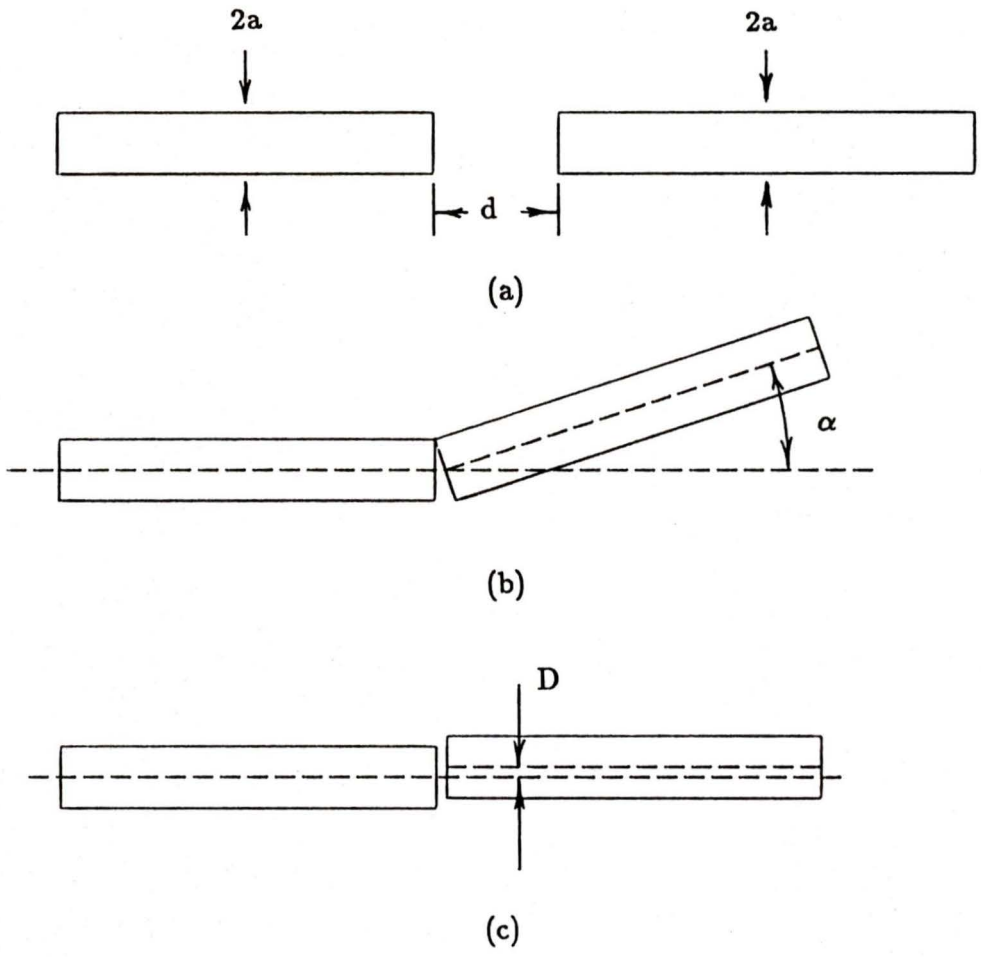

Figure 3.1: The three different types of splice loss geometries: a) longitudinal offset; b) angular tilt; c) lateral offset

Gaussian Analysis of $1.3\mu m$ Single Mode Fibre

For a single mode fibre optic waveguide, the only mode that propagates is the HE_{11} mode [43], and only the field spreading of the HE_{11} mode in a fibre is an important parameter for fibre jointing [52]. With the half power width of the field pattern or spot size being similar to the width of an incident Gaussian beam, the field distribution of a single mode fibre can be assumed to be approximately equal to the width of the incident Gaussian beam output from the laser into the fibre [54].

The spot size is a function of the core radius a, wavelength λ, cutoff wavelength $V = \frac{(2\pi a)}{\lambda}(n_1^2 - n_2^2)^{1/2}$ and numerical aperature $NA = (n_1^2 - n_2^2)^{1/2}$, where n_1, n_2 are the refractive indices of core and cladding respectively.

By replacing the HE_{11} mode of the sending fibre by its approximate transformed Gaussian field, the splice loss calculations can be greatly simplified.

From the end-on and 3-D view of Figures 3.2a and b, the various loss parameters can be seen more clearly. The axis of the incoming fibre makes an angle α with that of the outgoing fibre axis and ϕ is the projected rotation angle on the transverse plane relative to the displacement. The polarization angle of the HE_{11} mode is δ.

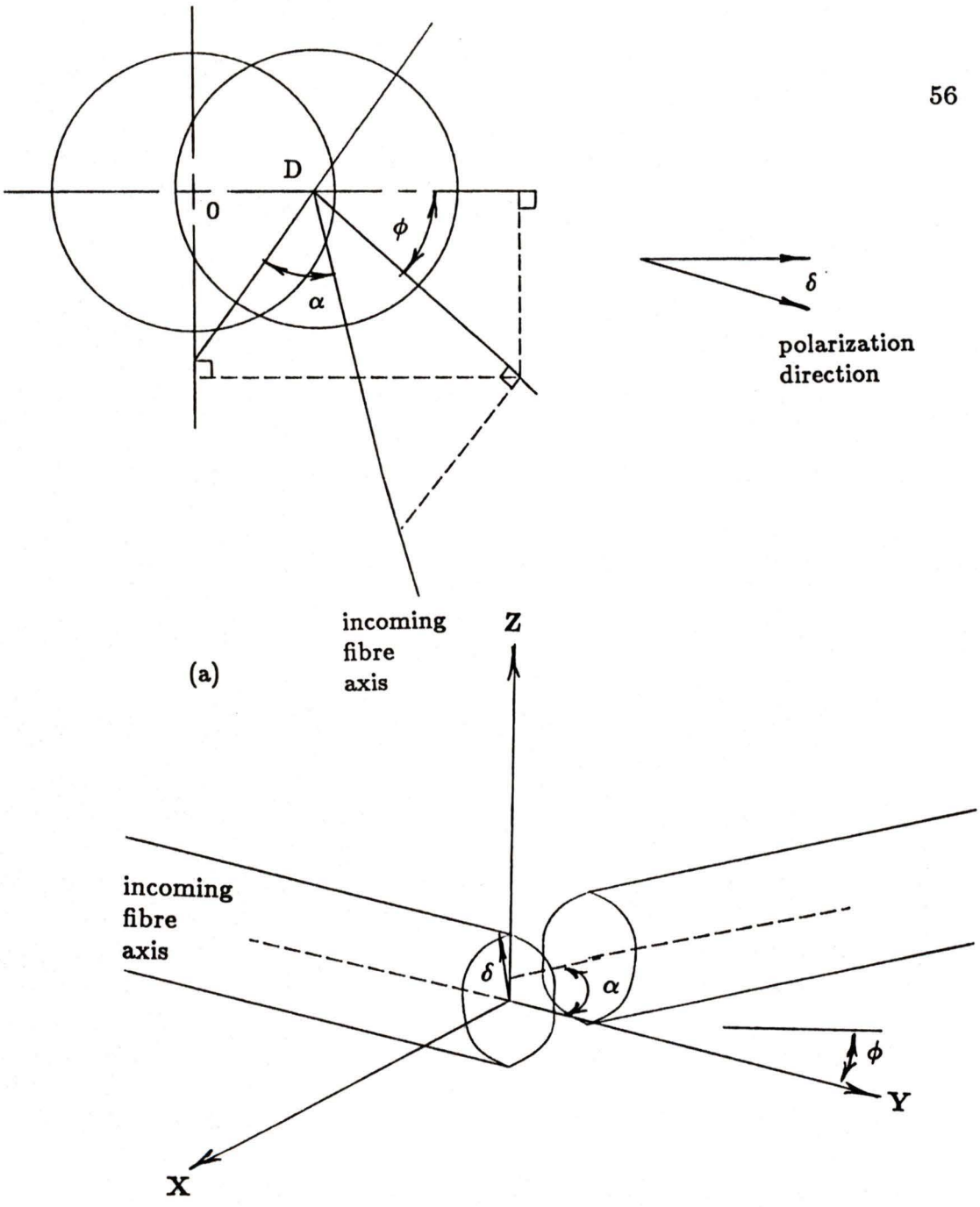

Figure 3.2: Lateral offset and angular tilt geometry, a) end-on view, b) 3-D perspective.

It has been shown that the transmission efficiency η through the joint is [53,54]

$$\eta = \frac{\exp[-(D/\omega)^2]}{w^4\pi^2}\left|\int_0^{2\pi}\int_0^{\infty}\exp\left[-\frac{R^2 - RD\cos(\theta-\delta)}{w^2} - \frac{jn_1V\alpha}{NA}(R^2+D^2-2RD\cos(\theta-\delta))^{1/2}\cos(\theta-\delta)\right] RdRd\theta\right|^2 \tag{3.1}$$

where n_1 *is the core refractive index*
R, θ *are the normalized polar coordinates*

where ω, the normalized spot size of the HE_{11} mode is given by

$$\omega = (0.65 + 1.62V^{-1.5} + 2.88V^{-6})/2^{1/2} \tag{3.2}$$

By setting $\alpha = 0$ in Equation 3.1, the loss due to lateral offset is given by

$$T_l = 2.17(D/\omega)^2 dB \tag{3.3}$$

and similarly, the loss due to angular misalignment can be found by setting $D = 0$.

$$T_a = 2.17(\alpha\omega n_1 V/NA)^2 dB \tag{3.4}$$

It has been found [54] that for small losses of less than .75dB per splice, that the total loss in a fibre splice is given by the arithmetic sum of T_l and T_a.

By substituting the expressions for V and NA into Equation 3.4 we get

$$\begin{aligned} T &= T_l + T_a \\ &= 2.17(D/\omega)^2 + 2.17\left[(\alpha\omega n_1)\frac{2\pi a}{\lambda}\frac{(n_1^2-n_2^2)^{1/2}}{a(n_1^2-n_2^2)^{1/2}}\right]^{1/2} \\ &= 2.17(D/\omega)^2 dB + 2.17(2\pi\alpha\omega n_1/\lambda)^2 dB \end{aligned} \tag{3.5}$$

which can be used to model the loss in a $1.3\mu m$ single mode fibre cable.

Deviated Gaussian Analysis of $1.55\mu m$ DSSM fibre

Single mode fibres can be considered "weakly guided" [55] where

$$n_1/n_2 - 1 \ll 1 \tag{3.6}$$

where n_1 = *maximum index of the core*
n_2 = *cladding index*

In the manufacture of DSSM $1.55\mu m$ fibres, the differences between the core and cladding indexes are decreased leading to fibres which are more weakly guided than those at $1.3\mu m$. This leads to spot sizes which are clearly different from the Gaussian standard fields [56].

This led Petermann [56] to a new "strange" spot size ω_L which he called the Laplace spot size. Povlson et al [57] derived a deviation parameter to relate the Gaussian spot size to the Laplace spot size. This parameter

is called ξ_o where

$$\xi_o = \omega_G/\omega_L \tag{3.7}$$

where ω_G = *Gaussian spot size*

and by using empirical methods, determined the relationship between ξ_o and ω_L

$$\xi_o = .957 - .0053\omega_L + .013\omega_L^2 \tag{3.8}$$

and that the Laplace spot size for the $1.55\mu m$ DSSM fibre is $4.5\mu m$. Povlson also has shown that these functions are almost index profile independent so that for the triangular profiles used in the DSSM fibre (See Equation 3.9),

$$n^2(r) = n_o^2\left(1 - 2\Delta\left(\frac{r}{a}\right)\right) \tag{3.9}$$

where $\Delta = \frac{n_o - n_c}{n_0}$
n_o = *maximum core index*
n_c = *cladding index*

we can use the maximum value n_o as the core index of refraction.

Substituting these parameters into Equation 3.5, we get

$$T = 2.17(D/\xi_o\omega_L)^2 + 2.17\left(\frac{2\pi\xi\omega_L n_o\alpha}{\lambda}\right)^2 dB \tag{3.10}$$

Monte Carlo Simulation

To accurately model the randomness of the fusion splice, a Monte Carlo simulation is performed (See Appendix 1).

It has been shown [58] that the triangular profile DSSM fibre is more sensitive to lateral offset (core concentricity) than fibre tilt.

For the fusion method used here, surface tension forces which realign the cladding of the fibre produces core concentricity and deformation losses [59]. Extensive analysis of fusion techniques [51] have shown that the minimum and maximum offset ranges from 0 to $1.1\mu m$ and the axial tilt from 0 to 1.1 degrees.

Using the above parameters, Equation 3.10 was simulated 10,000 times with the results shown in Figure 3.3 and the mean and standard deviation shown in Table 3.1. This leads to a theoretical mean of .29dB

Simulated	
Mean	Standard Deviation
.29dB	.04dB

Table 3.1: Mean and standard deviation of a splice for 10^4 samples.

per splice.

3.2.2 Coupler Loss

The fabrication of the single mode fibre tapered coupler has been given previously in Chapter 2. As the two fibres are melted together, the core diameters are reduced, thus lowering the cutoff value V. When the fundamental mode exceeds its cutoff condition, it detaches from the core of the fibre and becomes a cladding mode guided by the air-cladding boundary.

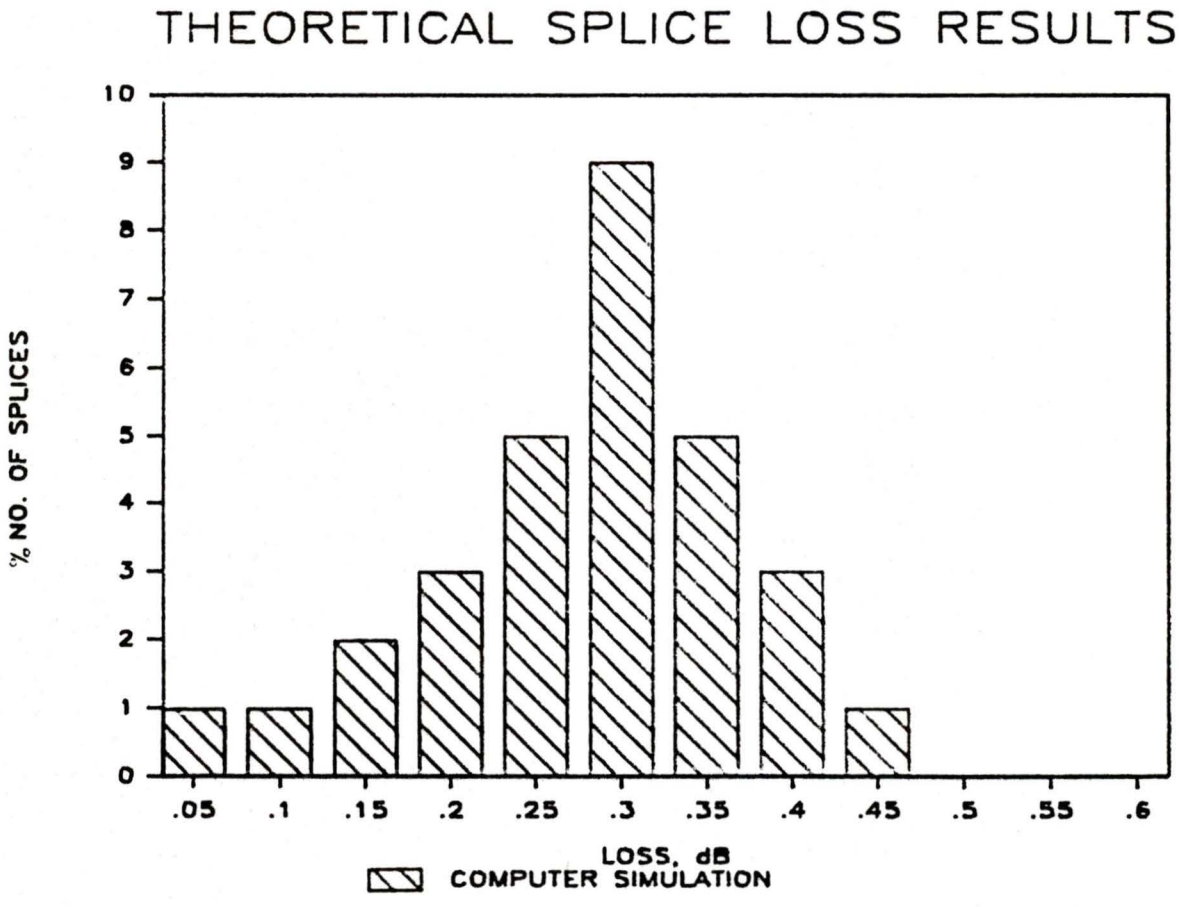

Figure 3.3: Theoretical simulation of splice loss.

This cutoff loss mechanism has been described extensively in several papers [60,61,62]. The loss in the coupler is a function of the shape of the taper, the core diameters, operating wavelengths and refractive indices. To accurately calculate the loss in the taper, models of the slopes of the taper have been proposed with good results [61] (See Figure 3.4).

The power of one of the output ports can be described by Equation

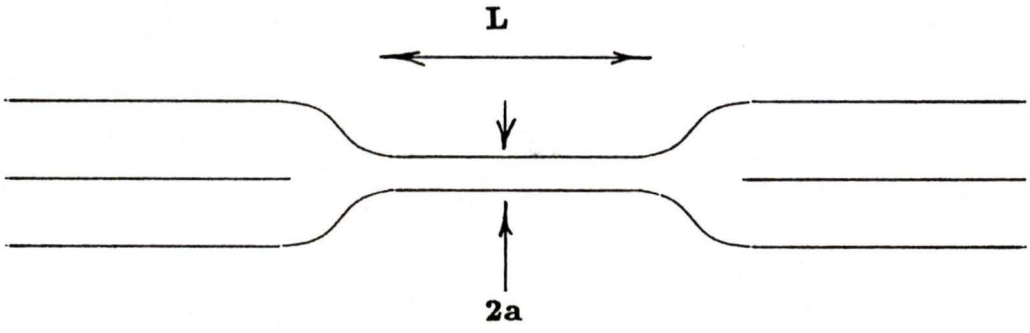

Figure 3.4: Geometric model of the taper of a single mode fibre splitter. L is the taper length and 2a is the taper width.

3.11

$$P = P_i \sin^2(cL) \tag{3.11}$$

$$\begin{aligned} \textit{where} \quad P_i &= \textit{Power into the fibre} \\ c &= \frac{3\pi\lambda}{32 n_2 a^2} \frac{1}{(1+1/V)^2} \\ L &= \textit{Taper length} \\ a &= \textit{Taper core diameter} \\ \textit{and} \quad V &= \frac{2\pi a}{\lambda}(n_1^2 - n_2^2)^2 \ \textit{as before} \end{aligned}$$

The loss can be calculated by

$$\begin{aligned} 10\log_{10} P &= 10\log_{10} P_i + 10\log_{10}\sin^2(cL) \\ PdB - P_i dB &= \alpha \\ \alpha &= 10\log_{10} sin^2(cL) \end{aligned} \tag{3.12}$$

The loss in each coupler is then calculated to be 1.3 $\pm$ .3dB. The variation in the loss results from the $\pm$.5% difference in the manufacturer's specifications.

3.2.3 Total Loss

A block diagram of the various loss components in the matrix switch is shown in Figure 3.5. By adding the loss in the splices with those of the couplers, the total theoretical insertion loss can be calculated. The results are shown in Table 3.2.

Theoretical	
Mean	Standard Deviation
3.47	.72dB

Table 3.2: Mean and standard deviation of theoretical insertion loss analysis.

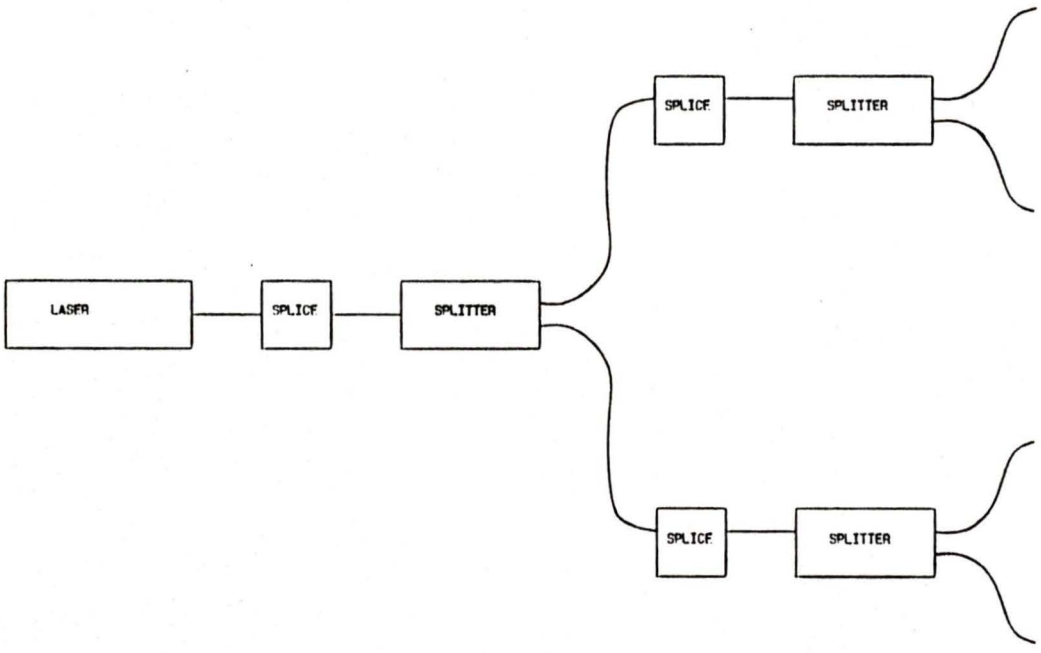

Figure 3.5: Loss components in the matrix switch

3.3 Frequency Response Analysis

The frequency response of the laser and photodiode receiver assembly determines the bandwidth of the signal that can be switched. Each component is studied using equivalent circuit models. This technique provides a better understanding of the performance of the devices and uses as a basis, the operating characteristics provided by the manufacturer. After the parameters of the models are derived, a standard computer circuit analysis package, SPICE (Simulation Program with Integrated Circuit Emphasis), is used to determine the device response.

3.3.1 Laser Model

The structure of the InGaAsP/InP ridge waveguide laser has been shown previously in Chapter 2, Figure 2.3. The circuit model for the ridge waveguide laser used here [63,64] combines the effects of the package and chip parasitics with the emission and absorption effects of the active region.

Parasitic Model

The package and chip parasitics can be analyzed with the model shown in Figure 3.6.

The electrical parasitics of the chip are modeled by R_s and C_s. The

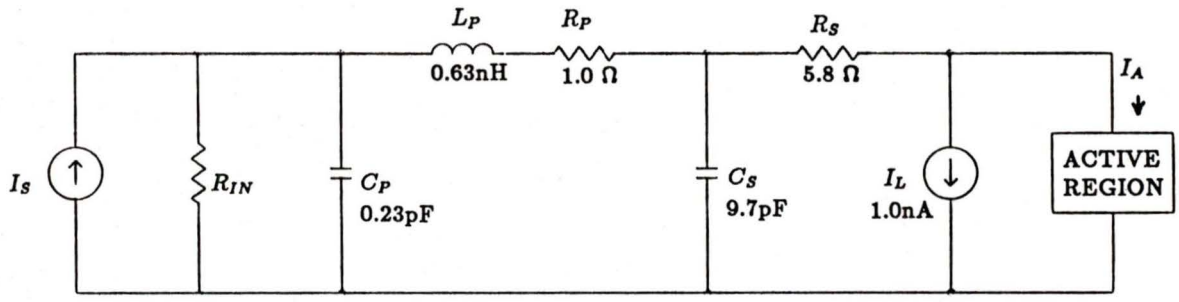

Figure 3.6: Chip and package parasitic circuit model for the laser diode.

symbol R_s is the series resistance of the ridge and metal contacts plus the resistance of the substrate below the active region. The substrate resistance is small compared to that of the metal layer and can be ignored. C_s is the shunt parasitic capacitance which is composed of the insulator layer capacitance plus the space charge capacitance at the heterojunction.

The package parasitics are modeled by R_p, L_p and C_p. The quantities R_p and L_p represent the resistance and inductance of the bond wire respectively while C_p represents the shunt capacitance to ground.

R_{in} and I_s represent the source resistance and current of the drive circuit while I_L represents dc leakage current. I_L is negligibly small for ridge waveguide lasers (See Chapter 2, Table 2.1). The package parasitic element values are provided by RCA but may vary slightly between devices. R_s is calculated using the chip dimensions and characteristics provided by the manufacture and the equation for the resistance of a semiconductor bar

$$R = \frac{L}{w\mathtt{t}}\frac{1}{\sigma} \tag{3.13}$$

where L = *length of the bar*
w = *width of the bar*
$\mathtt{t}$ = *thickness of the bar*
and

$$\sigma = qp\mu_p \tag{3.14}$$

where q = *the elementary charge in coulombs*
p = *doping density in* cm^{-3}
μ_p = *hole mobility in* $cm^2V^{-1}s^{-1}$

For the InGaAsP/InP ridge which is p doped, the hole mobility is $70cm^2V^{-1}s^{-1}$ with a doping density of $3 \times 10^{17}cm^{-3}$. The dimensions are [49] $3 \times 6 \times 280\mu m^3$. With an estimated contact resistance of 0.5 Ω the total series resistance is calculated to be 5.8 Ω.

With the laser operating in forward bias, the charge storage capacitance at the p-n junction is dominant. This can be calculated from the equation

$$\begin{aligned} G_j &= \frac{q}{kT} I(dc) \\ C_j &= G_j \tau_p \end{aligned} \tag{3.15}$$

where q = *the elementary charge in coulombs*
k = *Boltzmann's constant in* J/K
T = *temperature in degreesC*
and τ_p = *hole lifetime in sec*

This current flowing through the p-n junction is small as the small p-layer isolates the junction from the active region. With $\frac{q}{kT} = 38.61V^{-1}$, hole lifetime of $\sim 10^{-8}$ s and dc current of $1mA$, the charge storage capacitance is calculated to be 38pF.

The insulation capacitance is calculated from the equation

$$C_i = \frac{\epsilon_r \epsilon_o A}{d} \tag{3.16}$$

where ϵ_r = *dielectric constant*
ϵ_o = *permitivity of free space in* F/cm
A = *Area*
d = *thickness of the layer*

The total series capacitance

$$\frac{1}{C_s} = \frac{1}{C_j} + \frac{1}{C_i} \tag{3.17}$$

is then calculated to be 9.7pF.

The package parasitics R_p, L_p and C_p are measured by the manufacturer. R_{in} is the resistance of the source which is 47 Ω. The values of the parasitic parameter elements are given in Table 3.3.

3.3.2 Active Region Model

The operation of a semiconductor laser is related to three processes: absorption, spontaneous and stimulated emission. A photon is absorbed when an electron from a filled state in the valence band moves to an empty state in the conduction band. Stimulation occurs when a photon with energy corresponding to the energy difference between the filled state and

Element	Unit	Laser
C_p	pF	0.23
L_p	nH	0.63
R_p	Ω	1.0
C_s	pF	9.7
R_s	Ω	5.8
I_L	nA	1.0

Table 3.3: Parasitic element values for a ridge waveguide laser model

conduction band, stimulates the emission of a similar photon of equal energy by the transition of an electron from a filled state in the conduction band to an empty state in the valence band. Spontaneous emission occurs when an electron in the conduction band spontaneously returns to an empty state in the valence band with the emission of a photon.

In the double heterostructure (DH) laser, as the forward bias current is applied, there is spontaneous emission in all directions. As the threshold is reached, stimulated emission occurs.

The ability of a laser to respond to high modulation rates is limited by the damping of the oscillations in the cavity. Coupling between the carrier and photon populations and nonlinear absorption at the edges of the stripes are factors which contribute to the damping mechanism.

For single or near single frequency lasers, the dynamic properties of

the active region can be studied using the single mode rate Equations 3.18 and 3.19 [63]:

$$\frac{dS}{dt} = \{\Gamma g(N)[1-\varepsilon S] - 1/\tau_p\}\, S + \Gamma\beta\frac{N}{\tau_n} \tag{3.18}$$

$$\frac{dN}{dt} = \frac{I_A}{\alpha} - \frac{N}{\tau_n} - g(N)[1-\varepsilon S]S \tag{3.19}$$

where S is the photon density averaged over the nominal modal volume, N is the electron density averaged over the volume of the active region, Γ is the optical confinement factor given by the ratio of the active region and modal volumes, $g(N) = g_o(N - N_o)$ is the optical gain, g_o is a constant gain factor, N_o is the electron density at which $g = 0$,τ_p is the photon lifetime, τ_n is the spontaneous recombination lifetime, β is the fraction of spontaneous emission coupled into the lasing mode, α is the volume of the active region multiplied by the electronic charge, and I_A is the current injected into the active region from the parasitic equivalent circuit. The parameter ε is a small number which defines the gain compression characteristics of the active region.

By transforming these equations into an equivalent large signal model [65], and then linearizing the large signal model [66], a small signal model is derived as shown in Figure 3.7.

The element electrical values are given in terms of the dc drive current and the device characteristics by the expressions in equation 3.20 through

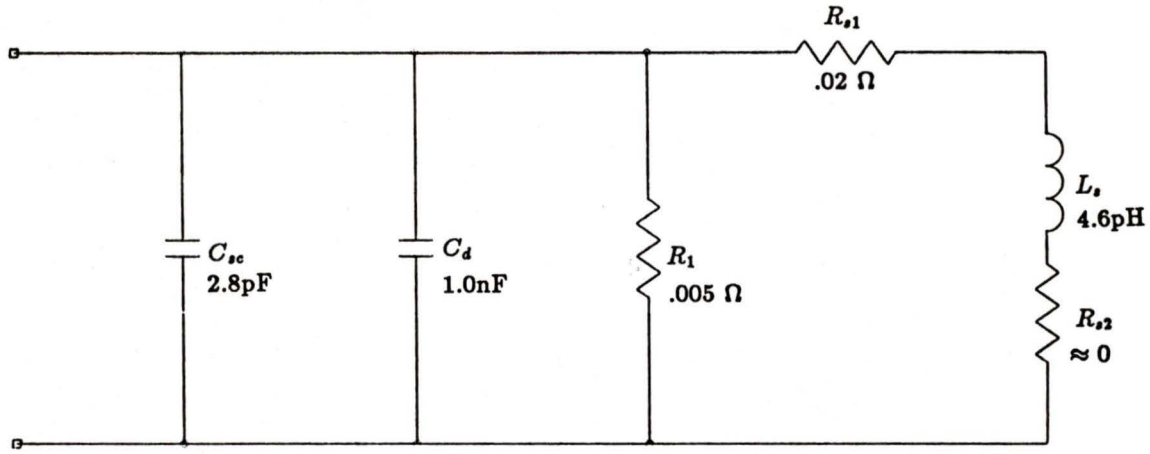

Figure 3.7: Small signal circuit model of the active region

3.25.

$$R_1 \simeq \frac{R_d}{1 + g_o \tau_n S_o} \tag{3.20}$$

$$C_d = \tau_n / R_d \tag{3.21}$$

$$R_d \simeq 2kT / q I_{tA} \tag{3.22}$$

$$L_s \simeq \frac{R_d \tau_p}{g_o \tau_n S_o} \tag{3.23}$$

$$R_{s1} \simeq \frac{\varepsilon R_d}{g_o \tau_n} \tag{3.24}$$

$$R_{s2} \simeq \frac{\beta \Gamma R_d \tau_p I_{tA}}{\alpha g_o \tau_n S_o^2} \tag{3.25}$$

with C_{sc} equal to the space charge of the active region of the heterojunction. The threshold current of the active layer is given by

$$I_{tA} \simeq \frac{\alpha\left(\frac{1}{\tau_p \Gamma g_o} + N_o\right)}{\tau_n} \tag{3.26}$$

and the steady state photon density (above threshold) is given by

$$S_o \simeq \frac{\Gamma \tau_p}{\alpha}(I_o - I_{th}) \tag{3.27}$$

where I_o *is the dc component of the total drive current*$(I_A + I_L)$
and $I_{th} = I_{tA} + I_L$ *is the external threshold current*

The parameter values are shown in Table 3.4 [63]. I_{th} and I_L are provided by the manufacturer.

The calculated electrical element values are shown in Table 3.5.

3.3.3 SPICE Analysis

SPICE is a circuit simulation program for nonlinear DC, nonlinear transient and linear AC analysis. Resistors, capacitors, inductors, independent and dependent voltage and current sources, and four types of semiconductor devices:diodes, BJTs, JFETs and MOSFETs may be contained in the circuit. The AC small signal analysis computes the required output parameter versus a function of frequency. The user specifies the frequency

Parameter	Unit	Laser
α	Am^3s	6.6×10^{-35}
β		2.0×10^{-4}
Γ		0.3
ε	m^3	6.7×10^{-23}
g_o	$s^{-1}m^3$	3.2×10^{-12}
N_o	m^{-3}	10^{24}
τ_n	ns	1.0
τ_p	ns	1.0
I_{th}	ma	630
I_L	na	10

Table 3.4: Parameter values for a ridge waveguide laser model.

Element	Unit	Laser
R_1	Ω	.005
C_d	nF	1
R_d	Ω	1
L_s	pH	4.6
R_{s1}	Ω	.02
R_{s2}	Ω	≈ 0
C_{sc}	pF	2.8

Table 3.5: Element values for ridge waveguide active region model.

range and the input signal with variations in magnitude, phase and pulse type variable. Output may be plotted in dB and several points can be analyzed at one time.

The electrical values given in Tables 3.3 and 3.5 are programmed into SPICE (See Appendix 2) and the resulting frequency response is calculated. The result is shown in Figure 3.8. By varying the calculated values by 5 percent, the resulting frequency responses show very little change as shown in Figure 3.8.

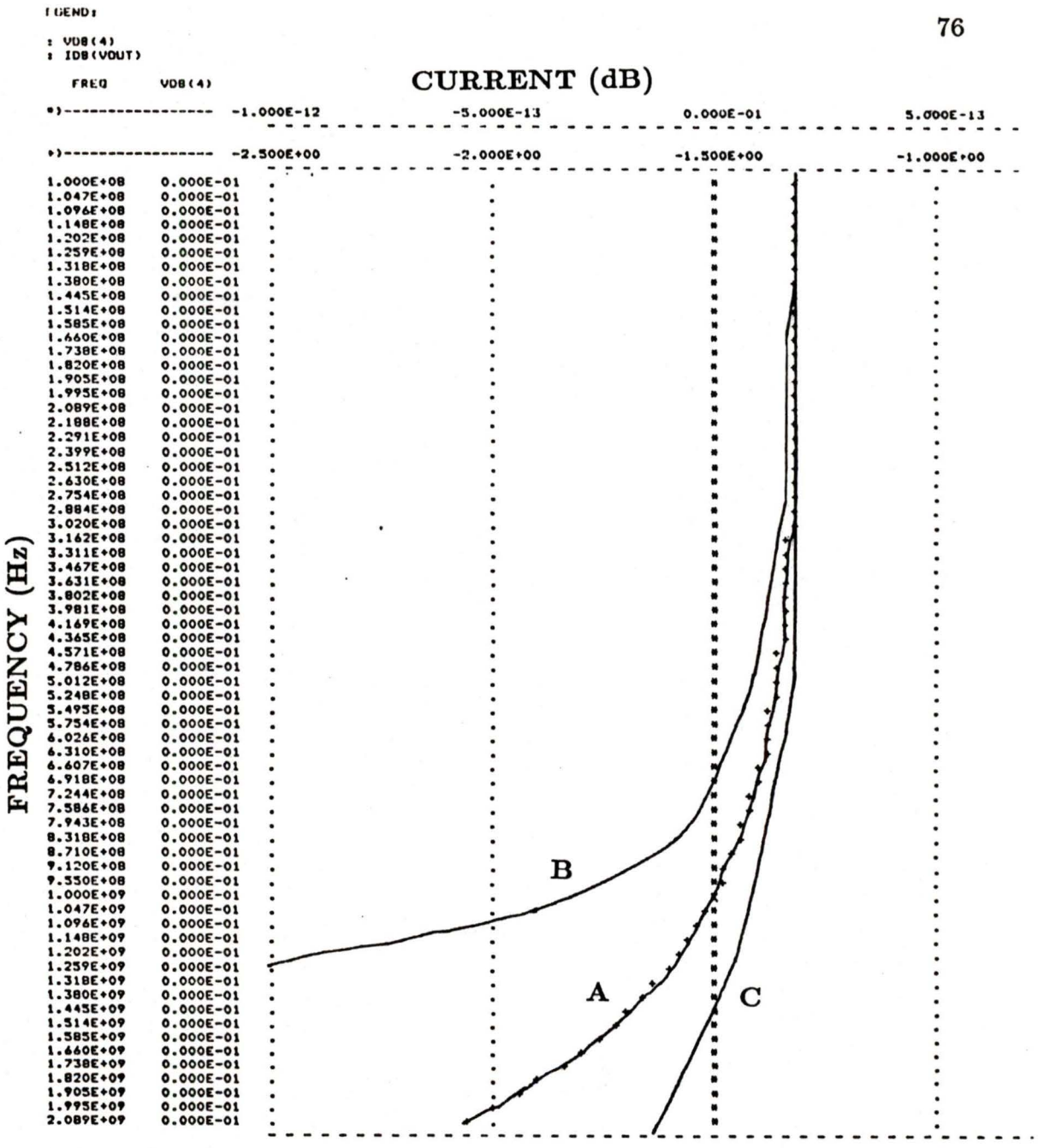

Figure 3.8: Frequency response of the InGaAsP ridge waveguide laser diode using the circuit models of Figures 3.6 and 3.7. A)Calculated results; B)Increasing R_s and C_s by 5%; C)Decreasing R_s and C_s by 5%.

3.4 Photodiode Model

The structure of the InGaAs/InP photodiode has been given previously in Chapter 2, Figure 2.4. The junction is formed between the two semiconductors of different bandgap energies where $E_g = .73eV$ for InGaAs and $E_g = 1.27eV$ for InP.

In general, the performance of a photodetector is characterized by three parameters:quantum efficiency, the response time and the sensitivity or detectivity. For the heterojunction photodiode, quantum efficiency does not depend as much on the geometry of the device but on the use of large bandgap materials for the optical window. By operating in reverse bias, the carrier transit time is reduced as is the junction capacitance, improving the response time. The sensitivity for a given wavelength is easily controlled by the use of the appropriate materials.

The equivalent circuit of the photodiode is given in Figure 3.9 [45]. The elements $i_p, \sqrt{i_s^2}, C_j, R_j$, and R_s are associated with the photodiode. The rms signal current is i_p and the mean square average shot noise is $\sqrt{i_s^2}$. The component C_j is the junction capacitance, R_j the junction resistance, and R_s the series resistance which is usually very small and can be neglected. The variable R_L is an external load resistor and R_i is the input resistance of the following amplifier.

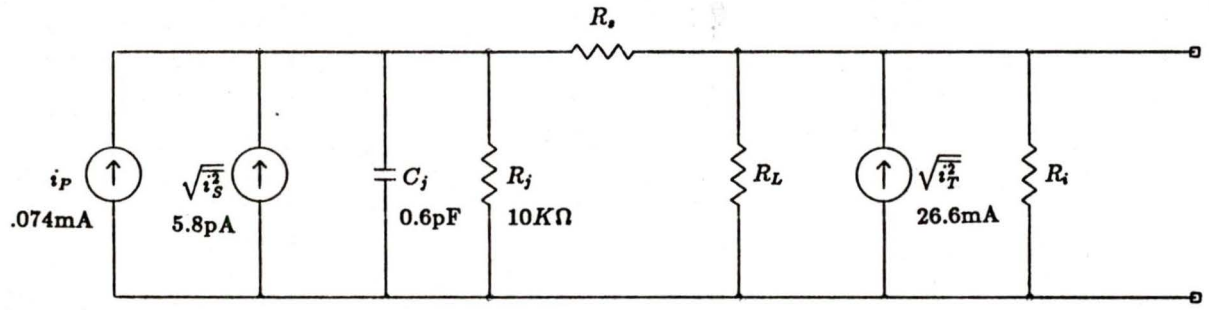

Figure 3.9: Equivalent circuit model of a photodiode

For an intensity modulated signal given by

$$P(\omega) = P_{opt}(1 + me^{j\omega t}) \tag{3.28}$$

where P_{opt} = *the average optical signal power*
m = *the modulation index*
ω = *the modulation frequency*

the responsivity is given by

$$\Re = \frac{I_p}{P_{opt}} = \frac{\eta q}{h\nu} = \frac{\eta \lambda}{1.24} A/W \tag{3.29}$$

where λ = *the wavelength in* μm
and I_p = *the photogenerated current*
η = *quantum efficiency*
h = *Planck's constant in* $J - s$
ν = *the frequency of light*

From Table 2.4 in Chapter 2, the responsivity at $1.55\mu m$ is .7 A/W. The quantum efficiency η can then be calculated to be .56.

The average photocurrent due to the optical signal is given by

$$I_p = q\eta P_{opt}/h\nu \tag{3.30}$$

where P_{opt} is obtained from the insertion loss measurements taken in Chapter 2 and is 0.15 mW. From this result, the rms signal power, $mP_{opt}/\sqrt{2}$ can be used to obtain the rms signal current

$$i_p = q\eta m P_{opt}/\sqrt{2}h\nu \tag{3.31}$$

The shot noise i_s is given by

$$\langle i_s^2 \rangle = 2q(I_P + I_B + I_D)B \tag{3.32}$$

where B = *the bandwidth*
I_B = *current from background illumination*
I_D = *dark current*

The junction resistance R_j can be calculated from Equation 3.13 given previously. The dimensions of the junction are $50 \times 50 \times 5\ \mu m^3$. Hole mobility μ_p is $150 cm^2 V^{-1} s^{-1}$, hole recombination lifetime τ_p is 1×10^{-8} sec and doping density p is estimated to be $1 \times 10^{18} cm^{-3}$ [67].

The thermal noise is given by Equation 1.32

$$\langle i_T^2 \rangle = 4kT(1/R_{eq})B \tag{3.33}$$

$$where \quad 1/R_{eq} = (1/R_j) + (1/R_L) + (1/R_i)$$

The parameters of the photodiode are summarized in Table 3.6.

The receiver and switching circuitry is added to the equivalent pho-

Element	Unit	Photodiode
i_p	mA	.074
$\sqrt{\overline{i_s^2}}$	pA	5.8
C_j	pF	0.6
R_j	$K\Omega$	10
$\sqrt{\overline{i_T^2}}$	mA	26.6

Table 3.6: Photodiode Element Values

todiode circuit for final analysis as shown in Figure 3.10. The appropriate Gummel-Poon parameters for the bipolar junction transistor, buffer am-

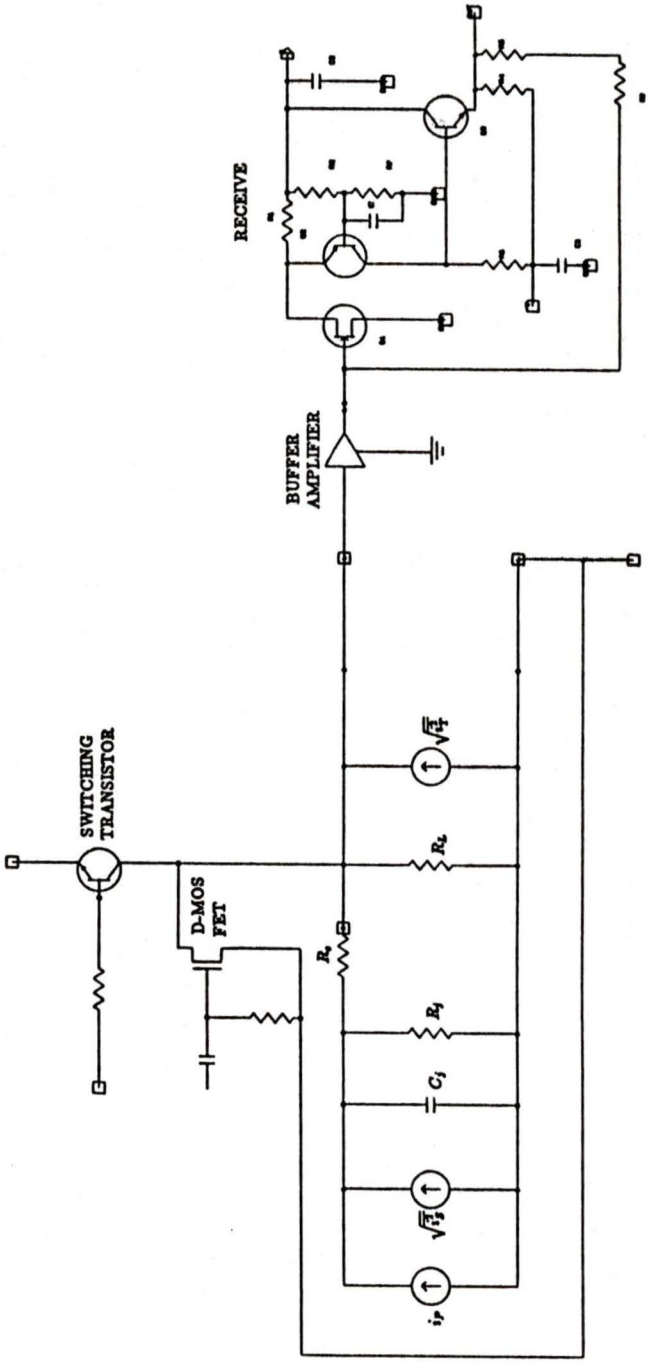

Figure 3.10: Complete receiving and switching assembly circuitry including the photodiode model.

plifier and parameters for the field effect transistor's are programmed into SPICE (See Appendix 2). A frequency response is then generated as shown in Figure 3.11. In this case, the bias switching transistor is modeled in the on state by a common collector configuration in saturation. By removing the switching assembly and receiver circuitry and modeling only the photodiode in SPICE, we get the frequency response shown in Figure 3.11. By examining the two curves, the addition of the switching and receiving circuitry does change the frequency response of just the photodiode.

In the off state, the photocurrent path of the photodiode is short circuited by the switching transistor which has a small leakage current. The isolation is increased with the presence of this transistor. The junction capacitance of the photodiode increases but the dark current decreases. Responsivity is reduced to .2 A/W which reduces quantum efficiency and the photogenerated current. The new parameter values are calculated and shown in Table 3.7. These new values are input into SPICE and a new frequency response is generated. (See Figure 3.12) By normalizing the output current to the input current and plotting the two curves on the same graph, the isolation between the on and off states can be predicted. This is shown in Figure 3.13.

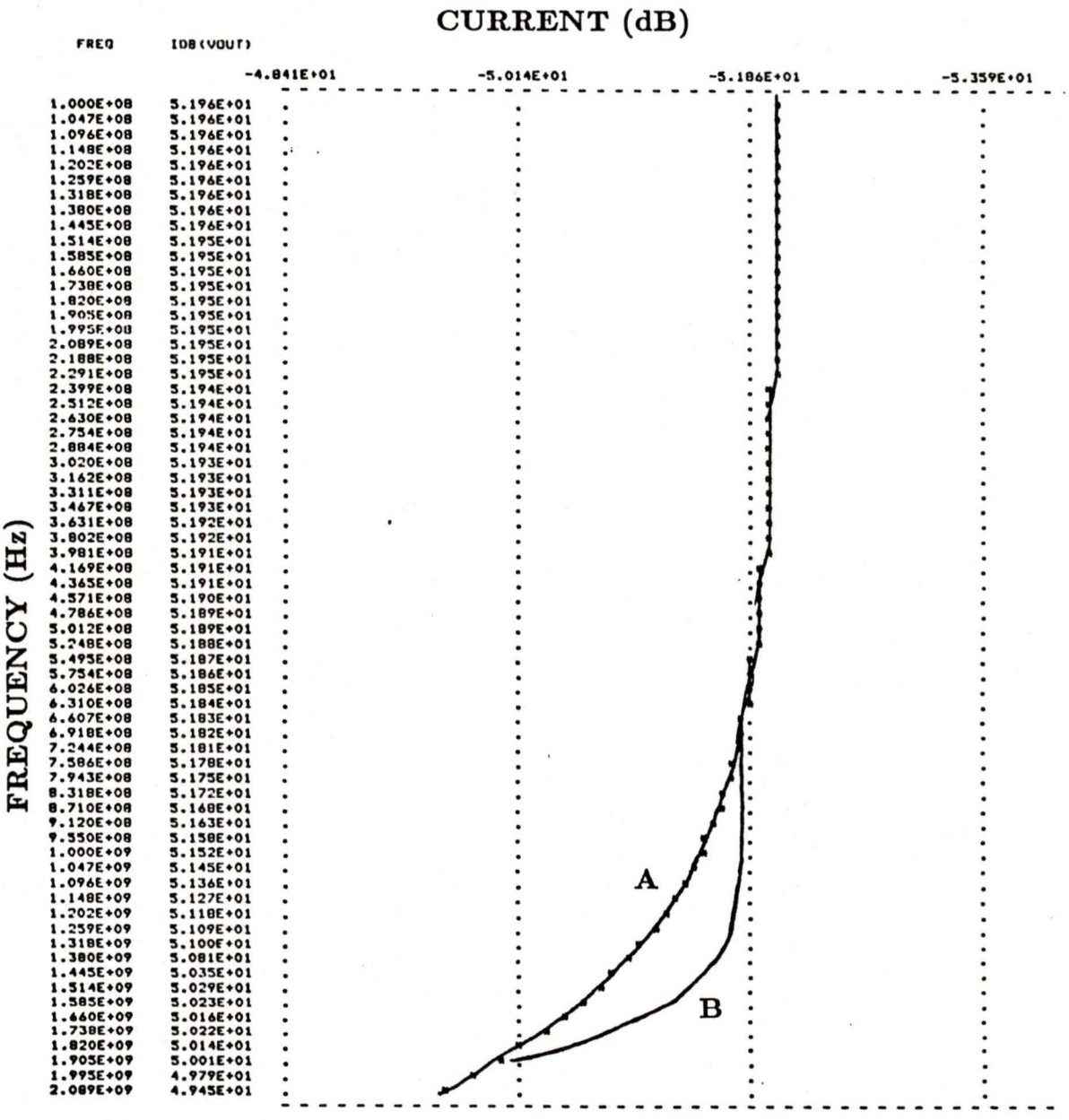

Figure 3.11: Frequency response of the switching and receiving circuitry and InGaAs/InP photodiode model. A)Photodiode, switching circuitry and receive circuitry. B)Photodiode only.

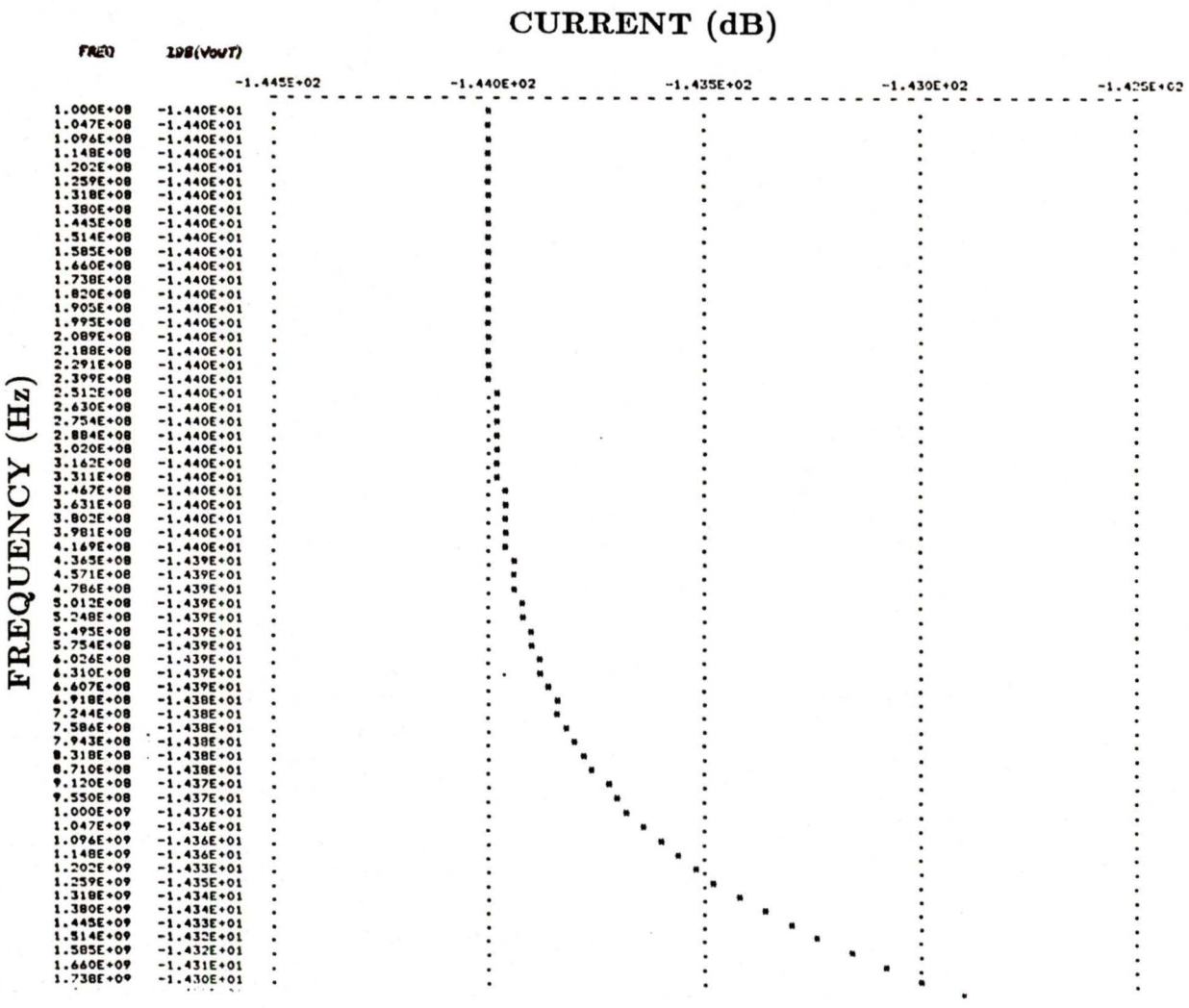

Figure 3.12: Frequency response of the receiving circuitry in the off state.

Element	Unit	Photodiode
i_p	mA	.021
$\sqrt{\overline{i_s^2}}$	pA	2.6
C_j	pF	2.6
R_j	K Ω	10
$\sqrt{\overline{i_T^2}}$	mA	26.6

Table 3.7: Photodiode Element Values in the off state

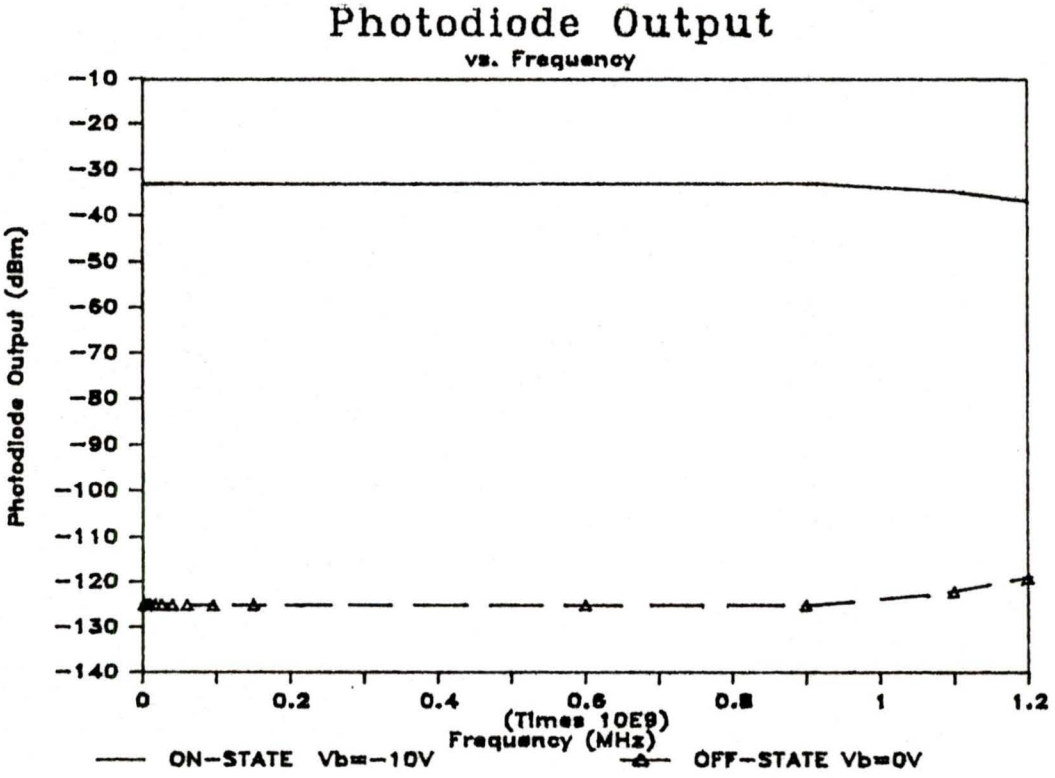

Figure 3.13: Theoretical isolation between photodiode on and off states.

3.5 Switching Response

The switching rise and fall times can be modeled by using the transient analysis component of SPICE. The controlling signal of the switching transistor can be configured to be a pulse with set width and appropriate rise and fall times.

To analyze the turn off switching transients, the initial conditions of the photodiode are set to the values calculated when the photodiode is at reverse bias (See Appendix 2). A pulse is sent to both the switching transistor and DMOS-FET. The resulting transient response is shown in Figure 3.14.

At turn on, the initial conditions of the photodiode are set to those calculated at zero bias. The appropriate pulse is sent to the switching transistor and the resulting transient is shown in Figure 3.15.

The turn on switching time is twice that of the turn off switching time. This was also shown in the experimental measurements of Chapter 2.

3.6 Summary

In this chapter, models for the insertion loss,laser and photodiodes were presented and switching transients were calculated.

By first showing that the joint loss in $1.3\mu m$ single mode fibre has been modeled by using the Gaussian spot size, a new model for $1.55\mu m$

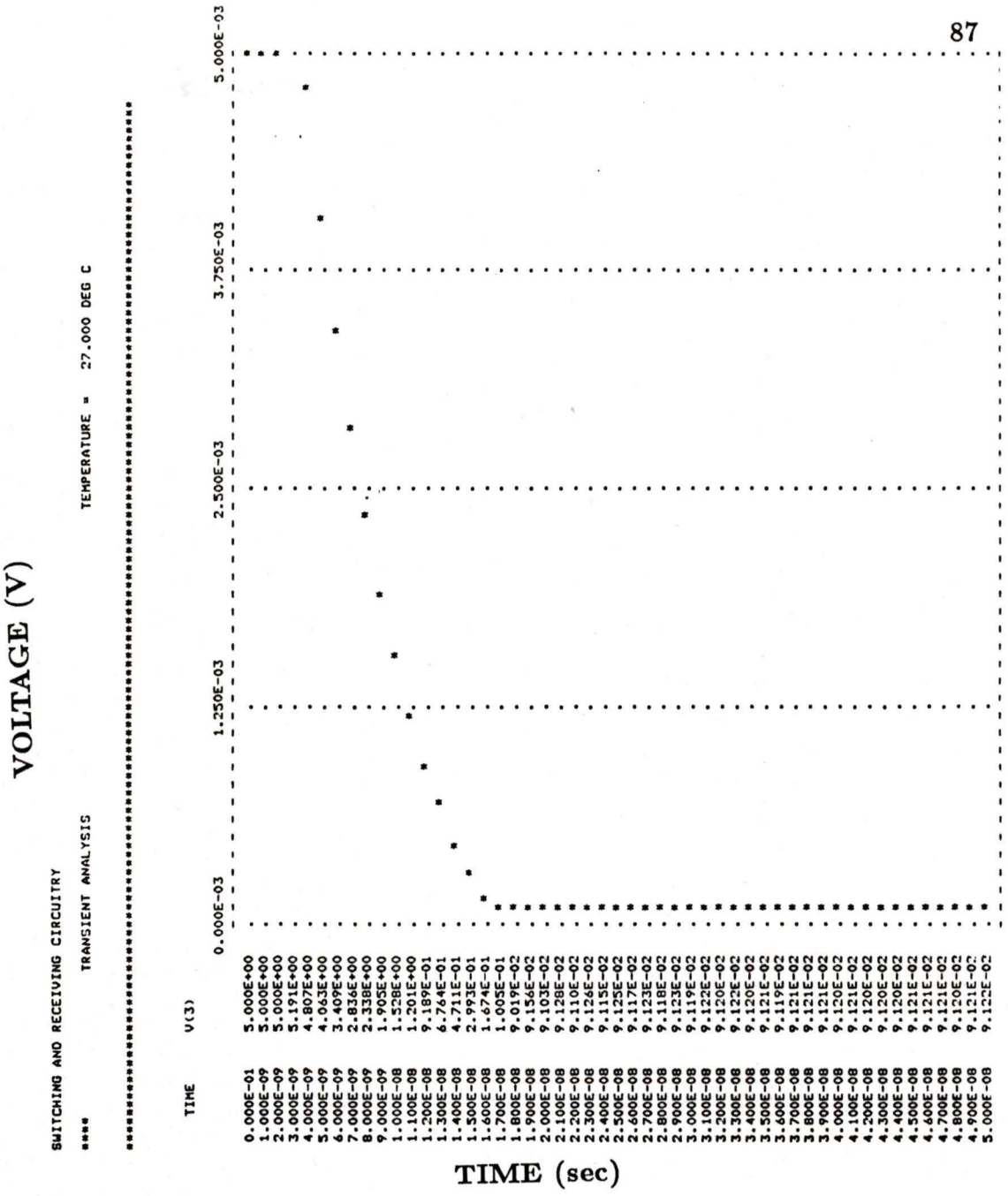

Figure 3.14: Simulation of the turn-off transients using SPICE.

VOLTAGE (V)

SWITCHING AND RECEIVING CIRCUITRY

**** TRANSIENT ANALYSIS TEMPERATURE = 27.000 DEG C

TIME	V(3)
0.000E-01	9.121E-02
1.000E-09	9.121E-02
2.000E-09	9.121E-02
3.000E-09	1.200E-01
4.000E-09	2.078E-01
5.000E-09	3.751E-01
6.000E-09	5.617E-01
7.000E-09	7.643E-01
8.000E-09	9.789E-01
9.000E-09	1.201E+00
1.000E-08	1.427E+00
1.100E-08	1.655E+00
1.200E-08	1.882E+00
1.300E-08	2.106E+00
1.400E-08	2.326E+00
1.500E-08	2.540E+00
1.600E-08	2.749E+00
1.700E-08	2.951E+00
1.800E-08	3.145E+00
1.900E-08	3.332E+00
2.000E-08	3.511E+00
2.100E-08	3.682E+00
2.200E-08	3.844E+00
2.300E-08	3.998E+00
2.400E-08	4.144E+00
2.500E-08	4.282E+00
2.600E-08	4.412E+00
2.700E-08	4.532E+00
2.800E-08	4.645E+00
2.900E-08	4.747E+00
3.000E-08	4.836E+00
3.100E-08	4.903E+00
3.200E-08	4.935E+00
3.300E-08	4.947E+00
3.400E-08	4.954E+00
3.500E-08	4.960E+00
3.600E-08	4.966E+00
3.700E-08	4.970E+00
3.800E-08	4.974E+00
3.900E-08	4.978E+00
4.000E-08	4.981E+00
4.100E-08	4.983E+00
4.200E-08	4.986E+00
4.300E-08	4.988E+00
4.400E-08	4.989E+00
4.500E-08	4.991E+00
4.600E-08	4.992E+00
4.700E-08	4.993E+00
4.800E-08	4.994E+00
4.900E-08	4.995E+00
5.000E-08	4.995E+00

Figure 3.15: Simulation of the turn-on transients using SPICE.

dispersion-shifted single-mode fibre (DSSM) was shown. By using Petermann's strange spot size, the loss mechanism was found to be a deviated version of the Gaussian loss equation. To model the randomness of a fusion splice, the loss equation was simulated using Monte Carlo techniques.

The laser diode was analyzed using an equivalent circuit model used previously. Junction resistances and capacitances were estimated using the basic semiconductor equations. The active region was modeled using a small signal circuit model derived from the large signal model and the various elements were calculated according to equations derived from the single mode state equations. A frequency response was generated using SPICE. The 3dB point of the laser diode equivalent circuit model was found to be approximately 3GHz.

The photodiode diode was also modeled using a previously derived circuit model and the various new parameters were derived from the device characteristics. The switching and receiving circuitry was then added to the photodiode equivalent circuit and a frequency response was generated using SPICE. The 3dB point of the photodiode equivalent circuit model was found to be approximately 2.2GHz. Both the on and off states were modeled and a theoretical isolation response was plotted. From this plot, a theoretical isolation of 90dB was predicted.

The on and off switching response was modeled using SPICE and the on and off state equivalent circuits of the photodiode. The turn-off time was calculated to be 17ns and the turn-on time was calculated to be 33ns.

Chapter 4

Results and Discussion

4.1 Introduction

The previous chapters have dealt with the design, construction and theoretical analysis of an optoelectronic broadband matrix switch. In this chapter the actual measured results are compared to those derived theoretically. Insertion loss, isolation and frequency response and switching transient times are compared to those derived from the various models of the components of the switch.

4.2 Insertion Loss

Measured and theoretical insertion loss is compared in Table 4.1. The

Measured		*Calculated*	
Mean	Standard Deviation	Mean	Standard Deviation
4.17dB	.24dB	3.47dB	.72dB

Table 4.1: Comparison of measured and calculated insertion losses

experimental loss is higher than the theoretical loss but within the standard deviation.

From practical experience with the Northern Telecom fusion machine, splice losses tend to vary over a fairly large range. Unless the splicing technique is practiced continuously, optimum splice loss performance cannot be maintained. By repeating a series of splices on a separate piece of DSSM Corning fibre optic cable, the splice loss ranges from .25dB to .43dB.

An alternative to fusion splicing the fibre cable components would be to use fibre optic connectors. This would reduce construction time and would make measurements easier. However, connectors add significant loss into the system and for practical networks, such as those for long distance trunk lines, fusion splicing is used.

The coupler loss equation is particularly sensitive to the taper radius and taper length. The manufacturer's specifications are taken from an average of components. Even with the small .5% variations in these characteristics, the theoretical loss can change by up to 30%. Couplers designed at $\lambda = 1.55\mu m$ are relatively new and the technology for optimizing their construction has not been fully developed. The type available within North America for $\lambda = 1.55\mu m$ fibre couplers is 1×2. This can be compared with a maximum size of 1×8 for couplers which are constructed of $\lambda = 1.3\mu m$ single mode fibre optic cable. The measured loss of a single coupler using the Photodyne XT17 power meter is within 5% of the manufacturer's spec-

ifications.

4.3 Frequency Response

From the theoretical analysis of the InGaAsP ridge waveguide laser diode, the parasitic elements are found to be the limiting factor in the frequency response analysis. With the rather high threshold current of 630mA, the leakage current in the active region is large, hence producing a larger space charge capacitance at the pn junction. This large capacitance also effects the active region but the other components are so small as to not have much effect.

The resulting frequency responses derived from varying the calculated components R_s and C_s, shows a very sensitive correlation to changes in these values. By carefully controlling doping densities and layer geometry, significant improvements in frequency responses can be made.

The 3dB point of the laser diode equivalent circuit model is approximately 3GHz. The 3dB point of the photodiode equivalent circuit model is approximately 2.2GHz. The overall limiting frequency response, therefore, is that of the photodiode and its associated circuitry.

4.4 Isolation

Measured and theoretical isolation characteristics are compared in Figure 4.1. The theoretical results are 10 to 15dB better than those measured in the laboratory.

In the optoelectronic switch, the isolation is the ratio between the output power received at reverse bias to that at zero bias. The isolation is obtained from the impedance changes and the heterojunction potential barrier which changes the quantum efficiency at zero and reverse bias. With the switching transistor in series with the photodiode, isolation is improved. The photocurrent path is open circuited by the switching transistor in cutoff.

By analyzing the complete receiving and switching assembly in SPICE, the various changes in the circuit model and switching transistor can easily be incorporated. The leakage current in the switching transistor at cutoff, which affects zero bias isolation, is also included.

In a practical system, the power received by the photodiode would be substantially reduced ($\approx$ 20dB). This would lead to reduced isolation performance.

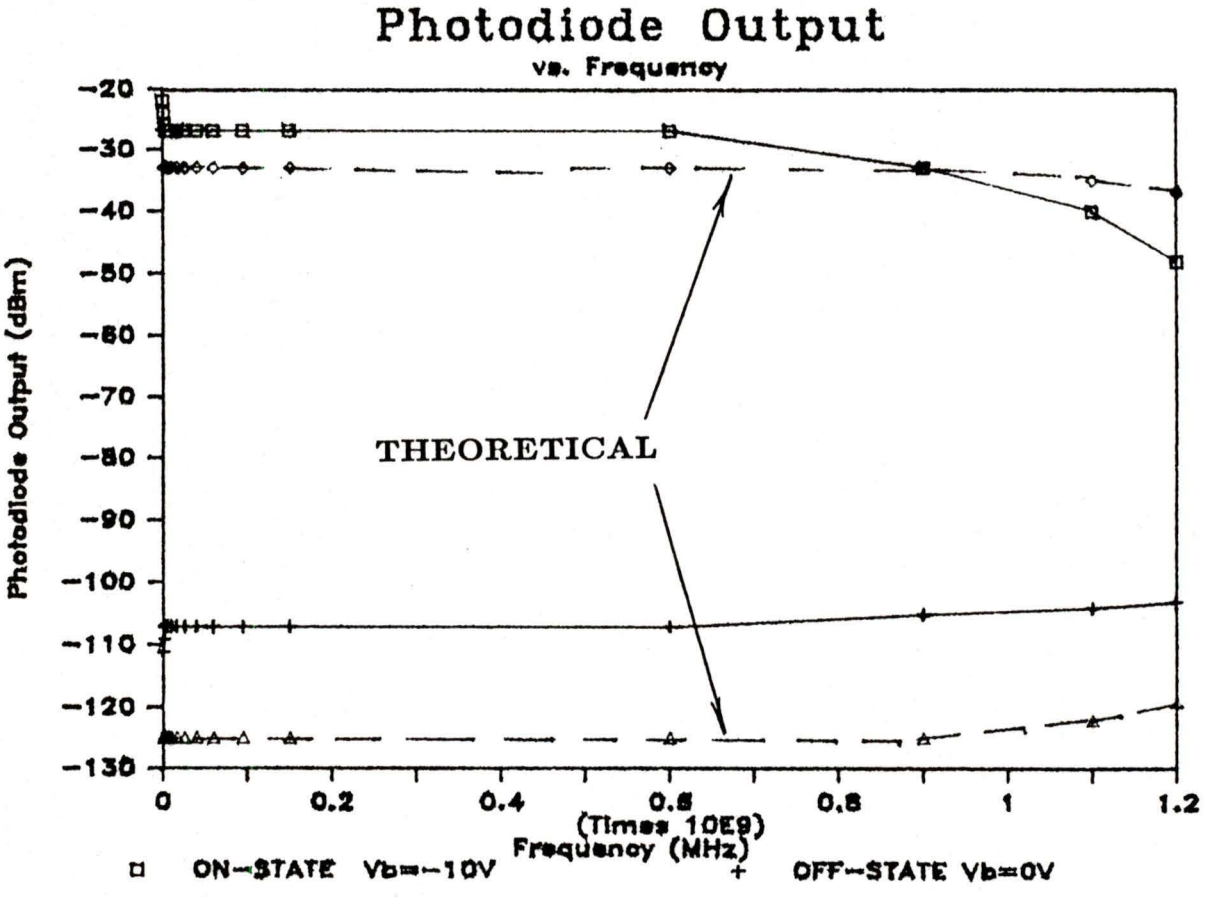

Figure 4.1: Comparison of measured and theoretical isolation characteristics.

4.5 RF Leakage, Ground Loops and Background Radiation

At the high frequencies used in measuring the characteristics of the optoelectronic switch, many variables contribute to reduced isolation.

Even short leads of coaxial cable from the HP8350B sweep oscillator to the laser produced rounding in the signal pulses when measured by an oscilloscope. Test equipment powered by receptacles at opposite ends of the laboratory could affect one another through ground loops in the electrical system. Line filters were added to the AC lines and decoupling capacitors were added to the power lines of the photodiode switching circuits to reduce these problems. Nicad batteries were used to power the receiver assemblies to remove any ground loops between the test equipment and the matrix switch..

In practical applications, the power used by telecommunications equipment located in a central office is also provided by batteries. Power lines are filtered and special grounding facilities are provided.

At frequencies beyond 1GHz, it was observed that the light level within the laboratory affected the receive pulse at the photodiode. By turning off the lights in the laboratory, the pulse shape would change shape. This could indicate a fibre pigtail/photodiode interface that is not entirely sealed. It could also indicate a ground loop between the light circuitry and the oscilloscope power plug receptacle.

4.6 Switching Transients

The predicted switching transients calculated from SPICE and those measured in the lab are shown in Table 4.2. The SPICE analysis did not

Measured		Calculated	
Turn On	Turn Off	Turn On	Turn Off
48ns	25ns	33ns	17ns

Table 4.2: Comparison of measured and calculated isolations.

include the oscilloscope leads although they are matched to a 50 Ω load.

The manufacturer's data sheet indicates a 320ps rise and fall time for the switching transistor. This indicates that the limiting factor in switching transition times is not the switching transistor. The RC time constant of the photodiode junction capacitance and its associated load resistance, the buffer amplifier or the associated receiver circuitry could be the limiting factor.

An analysis of the manufacturer's specifications for the buffer amplifier shows a very small $< 2pF$ leakage capacitance at zero bias. The specifications of the final transistor Q3 of the receiver could not be obtained and was modeled using the default NPN transistor parameters in SPICE. The indications are that the receiving circuitry may be the limiting factor in giving a smaller value for the theoretical switching times.

4.7 Summary

In this chapter, the measured results from Chapter 2 were compared to the theoretical results from Chapter 3. A good correlation was obtained between the theoretical insertion loss and the switching transients and the actual measured values. Also in this chapter, RF leakage and ground loop considerations were presented.

The measured results indicate that this optoelectronic switch could switch an 800Mb/s digital signal with an isolation of 80dB. On and off switching transients are 48ns and 25ns respectively for a 200Mb/s signal. In summary, the performance of the switch is more than adequate to be used as a line protection device in digital fibre optic systems.

Chapter 5

Conclusion and Future Research Considerations

5.1 Introduction

In this thesis, the design, construction and analysis of a 2 × 4 optoelectronic broadband matrix switch has been presented. This switch is capable of switching an 800MB/s digital signal at an isolation of 80dB when the received optical power is .15mW. The switching transients are 48ns for turn on and 25ns for turn off. The switch has practical applications as a digital line protection device.

In Chapter 1, the thesis objectives were outlined and a brief review of the various optical switching methods was made. The reasons for choosing the optoelectronic switch as the method to be studied were also presented.

In Chapter 2, the construction of the switch was outlined. The char-

acteristics of each component were discussed and the operating currents and voltages were determined. Measurements of insertion loss, isolation and frequency response and switching transients were performed. RF leakage and ground loop problems were found to contribute significantly to performance problems. Methods to improve these problems were discussed and implemented.

In Chapter 3, a theoretical analysis of the various performance measurements was undertaken. Insertion loss of a splice was modeled using a Monte Carlo simulation of the deviated Gaussian equation for loss due to lateral offset and angular tilt. Coupler loss was modeled using a previously derived equation based on the taper shape. Equivalent circuit models of the laser diode and photodiode were presented and the various electrical elements were calculated. The computer circuit simulation program SPICE was used to perform the various analysis. Frequency response, isolation and switching transients curves were generated.

In Chapter 4, the measured results were compared to those calculated theoretically. The various limitations of the modeling methods were discussed and the limiting performance components were presented. RF leakage and ground loops were again discussed with examples of problems which could not be corrected.

5.2 Future Research Considerations

In the areas of optical communications, new areas of research continue to be explored and expanded. Recently, an array of photodiodes has been integrated onto a single chip. This would reduce many of the RF problems associated with the photodiodes particularly when the receiver is also integrated onto the chip. Although costly at this time, the use of an integrated pin/FET assembly in an optoelectronic switch would improve RF and switching transients.

The photodiodes used in this experiment exhibited a rather poor heterojunction barrier. Better manufactured devices would improve isolation and simplify the switching circuitry.

5.3 Summary

This thesis has presented the design and analysis of a 2×4 optoelectronic broadband matrix switch. Capable of switching an 800MB/s digital signal with an isolation of 80dB, the switch can be utilized as a line protection device. The optoelectronic switch is capable of being incorporated in future fibre optic networks.

References

[1] Miller, Stewart E. "Integrated Optics: An Introduction" *The Bell System Technical Journal*, Vol. 48, No. 7, September 1969, pp 2059-2069

[2] Marcatili, E.A.J. "Dielectric Rectangular Waveguide and Directional Coupler for Integrated Optics" *The Bell System Technical Journal*, Vol. 48, No. 7, September 1969, pp 2071-2102

[3] Taylor, H.F. "Optical Switching and Modulation in Parallel Dieletric Waveguides" *Journal of Applied Physics*, Vol. 44, No. 7, July 1973, pp 3257-3262

[4] Papuchon, M., Y. Combemale, X. Mathieu, D.B. Ostrowsky, L. Reiberr, et al. "Electrically Switched Optical Directional Coupler:Cobra" *Applied Physics Letters*, Vol. 27, No. 5, September 1975, pp 289-291

[5] Kogelnik, Herwig, Ronald V. Schmidt. "Switched Directional Couplers with Alternating $\Delta\beta$" *IEEE Journal of Quantum Electronics*,

July 1976, pp 396-401

[6] Alferness, R.C., V.R. Ramaswamy, Steven K. Korotky, Manuel D. Divino, Lawrence L. Buhl. "Efficient Single-Mode Fibre to Titanium Diffused Lithium Niobate Waveguide Coupling for $\lambda = 1.32\mu m$" *IEEE Journal of Quantum Electronics*, Vol. QE-18, No. 10, October 1982, pp 1807-1812

[7] McCaughan, L. "Long Wavelength Titanium-Doped Lithium Niobate Directional Coupler Optical Switches and Switch Arrays" *Optical Engineering*, Vol. 24, No. 2, March/April 1985, pp 241-243

[8] Kondo, Michikazu, Yoshinori Ohta, Masahiko Fujiwara, Mitsuhito Sakaguchi. "Integrated Optical Switch Matrix for Single-Mode Fibre Networks" *IEEE Journal of Quantum Mechanics*, Vol. QE-18, No. 10, October 1982, pp 1759-1764

[9] Alferness, R.C., S.K. Korotky, L.L. Buhl, M.D. Divino. "High-Speed Low-Loss Low-Drive-Power Travelling-Wave Optical Modulator for $\lambda = 1.32\mu m$" *Electronics Letters*, Vol. 20 No. 8, April 1984, pp 354-355

[10] Hinton, H.S. "A Nonblocking Optical Interconnection Network Using Directional Couplers" *Proceedings of the 1984 IEEE Globecom*, Section 26.5.1 to 26.5.4

[11] Alferness, R.C. "High-Speed Optical Switches for Single-Mode Lightwave Communications" *Proceedings of the IEEE Globecom*, Section 26.2.1 to 26.2.4

[12] Veselka, J.J., S.K. Korotky "Optimization of $Ti : LiNbO_3$ Optical Waveguides and Directional Coupler Switches for $1.56\mu m$ Wavelength" *IEEE Journal of Quantum Electronics*, Vol. QE-22, No. 6, June 1986, pp 933-938

[13] Schmidt, R.V., L.L. Buhl. "Experimental 4X4 Optical Switching Network" *Electronic Letters*, Vol. 12, No. 22, October 1976, pp 575-577

[14] Bogert, G.A., E.J. Murphy, R.T. Ku "Low Crosstalk 4X4 $Ti : LiNbO_3$ Optical Switch with Permanently Attached Polarization Maintaining Fibre" *IEEE Journal of Lightwave Technology*, Vol. LT-4, No. 10, October 1986, pp 1542-1545

[15] Granestrand, P., B. Stoltz, L. Thylen et al. "Strictly Nonblocking 8X8 Integrated Optical Switch Matrix" *Electronics Letters*, Vol. 22, No. 15, July 1986, pp 816-818

[16] Inoue, Hiroaki, Koji Ishida, Hitoshi Sato, and Hiroyoshi Matsumura. "Switching Characteristics of GaAs Directional Coupler Optical Switches" Applied Optics, Vol. 25, No. 9, May 1986, pp 1484-1490

[17] Hale, P.G., R. Kompfner. "Mechanical Optical-Fibre Switch" *Electronics Letters*, Vol. 12, No. 15, July 1976, pp 388

[18] Yamamoto, Hisao, Haruo Ogiwara. "Moving Optical-fibre Switch Experiment" *Applied Optics*, Vol. 17, No. 22, November 1978, pp 3675-3678

[19] Ogiwara, Haruo, Masaaki Yokoyama, Yutaka Ohmori. "Fibre switch of 1 × 93:an Experimental Trial" *Optical and Quantum Electronics* Vol. 12, 1980, pp 87-90

[20] Kaufman, S., R.L. Reynolds, G.C. Loeffler "A Mechanical Optical Switch" *Integrated Optical Circuit Engineering (1984)*, SPIE Vol. 517, pp 275-280

[21] MacDonald, R.I., E.H. Hara "Optoelectronic Broadband Switching Array" *Electronics Letters*, Vol. 14, No. 16, August 1978, pp 502-503

[22] MacDonald, R.I., E.H. Hara "Switching with Photodiodes" *IEEE Journal of Quantum Electronics*, Vol. QE-16, No. 3, March 1980, pp 289-295

[23] Hara, Elmer H., Susumu Machida, Masahiro Ikeda, Hiroshi Kanbe, Tatsuya Kimura. "A High Speed Optoelectronic Matrix Switch Using Heterojunction Switching Photodiodes." *IEEE Journal of Quantum Electronics*, Vol. QE-17, No. 8, August 1981, pp 1539-1546

[24] Uesugi, N., S. Machida, T. Kimura. "4X8 Optoelectronic Matrix Switch Equipment using InGaAsP/InP Heterojunction Switching Photodiodes" *Optical and Quantum Electronics*, Vol. 15, 1983, pp 217-224

[25] MacDonald, R.I., Dennis K.W. Lam, Robert H. Hum, Julian P. Noad. "Monolithic Array of Optoelectronic Broad-Band Switches" *IEEE Journal of Solid State Circuits*, Vol. SC-19, No. 2, April 1984, pp 219-222

[26] Hara, Elmer H. "Optoelectronic Switching" *Integrated Optical Circuit Engineering 1984*, SPIE Vol. 517 pp 234-241

[27] Smith, P.W., I.P. Kaminow, P.J. Maloney, L.W. Stulz. "Self-contained Integrated Bistable Optical Devices" *Applied Physics Letters*, Vol. 34, No. 1, January 1979, pp 62-64

[28] Miller, D.A.B. "Optical Logic and the Self Electro-optic Effect Device (SEED)" *Proceedings of the 1984 IEEE Globecom*, Section 26.6.1-26.6.3

[29] Li Kam Wa, P., J.E. Stitch, N.J. Mason, J.S. Roberts, J.N. Robson. "All Optical Multiple-Quantum-Well Waveguide Switch" *Electronics Letters*, Vol. 21, No. 1, January 1985, pp 26-27

[30] Li Kam Wa, P., N. Robson et al "All-Optical Switching Effects in a Passive GaAs/GaAlAs Multiple-Quantum-Wall Waveguide Resonator" *Electronics Letters*, Vol. 22, No. 21, October 1986, pp 1129-1130

[31] Goto, H., I. Maeda, T. Nakano, U. Kihara, M. Torii. "An Evaluation of the Magnetooptical Characteristics of YIG Single Crystals" *Journal of Magnetism and Magnetic Materials* 31-34, 1983, pp 779-780

[32] Shirasaki, Masataka, Hirochika Nakajima, Takeshi Obokata, Kunihiko Asama. "Nonmechanical Optical Switch for Single-Mode Fibres" *Applied Optics*, Vol. 21, No. 23, December 1982, pp 4229-4234

[33] Shirasaki, Masataka, Fumio Wada, Hisashi Takamatsu, Hirochika Nakajima, and Kunihiko Asama. "Magnetooptical 2X2 Switch for Single-Mode Fibres" *Applied Optics*, Vol. 23, No. 19, October 1984, pp 3271-3276

[34] Kuhn, L. M.L. Dakss, P.F. Heidrich, B.A. Scott. "Deflection of an Optical Guided Wave by a Surface Acoustic Wave" *Applied Physics Letters*, Vol. 17, No. 6, September 1970, pp 265-267

[35] Schmidt, R.V., I.P. Kaminow, J.R. Carruthers. "Acousto-optic Diffraction of Guided Optical Waves in $LiNbO_3$" *Applied Physics Letters*, Vol. 23, No. 8, October 1973, pp 417-419

[36] Kersten, Ralf Th. "Integrated Optical Acousto-optic Switching" *Integrated Optical Circuit Engineering (1984)*, SPIE Vol. 517, pp 258-266

[37] Herriau, J.P., A. Delboublé, B. Loiseaux, J.P. Huignard. "Commutateur Optique Bidimensionnel Par Réseaux Holographiques Photoinduits" *Journal of Optics(Paris)*, Vol. 15, No. 5, pp 314-318

[38] Soares, O.D.D., M. Semlali, M. Grosmann. "Holographic Multiport Optical-Fibre Switch" *Proceedings of the Tenth European Conference on Optical Communication*, 1984, pp 72-73

[39] Miller, R.C., A. Savage. "Temperature Dependence of the Optical Properties of Ferroelectric $LiNbO_3$ and $LiTaO_3$" *Applied Physics Letters*, Vol. 9, No. 4, August 1966, pp 169-171

[40] Haruna, M., J. Koyama. "Thermooptic Deflection and Switching in Glass" *Applied Optics*, Vol. 21, No. 19, October 1982, pp 3461-3465

[41] Hayward, G.A., A.M. Gottlieb, D.G. Boyer, J.E. Berthold. "High-speed 16X16 CMOS Crosspoint Switch" *Electronics Letters*, Vol. 21, No. 20, September 1985, pp 923-925

[42] Yamanaka, N., H. Miyanaga, Y. Yamamoto "Newly Structured 512Mbit/s High-Speed Time-Division Switch" *Electronics Letters*, Vol. 22, No. 21, October 1986, pp 1094-1095

[43] Cherin, Allen H. "An Introduction to Optical Fibres" *McGraw-Hill Book Company*, ©Bell Telephone Laboratories, 1983

[44] Discussions with Ruth Raman, RCA Optoelectronics Division,Montreal, Quebec, March-April 1987.

[45] Sze, S.M. "Physics of Semiconductor Devices" *John Wiley and Sons*, 1981

[46] Equipment Manual "Photodyne XT16, XT17, and XT18 Power Meter Manual" *Photodyne Corporation*, 1986

[47] Discussions with Dr. Elmer H. Hara, University of Regina, Saskatchewan, March 1987

[48] Kim, Ock Ky, Bulusu V. Dutt, R.J. McCoy, John R. Zuber "InGaAs/InP pin-FET Receiver" *IEEE Journal of Quantum Electronics*, Vol. QE-21, No. 2, February 1985, pp 138-143

[49] Discussions with Henry Sealman, RCA Optoelectronics Division, Montreal, Quebec.

[50] Markey, Brian J. "High-speed photodetector switching" *Integrated Optical Circuit Engineering 1984*, SPIE Vol. 517 pp 242-245

[51] McCartney, D.J., D.B. Payne "Monomode Optical Fibre Splicing" *Proceedings of the SPIE, Fibre Optics: Short-Haul and Long-Haul Measurements and Applications II*, Vol. 500, 1984, pp 37-43

[52] Barnoski, M.K. "Fundamentals of Optical Fibre Communications" *Academic Press, Inc*, New York, 1976

[53] Marcuse, D. "Loss Analysis of Single-Mode Fiber Splices" *Bell System Technical Journal*, Vol. 56, No. 8, May-June 1977, pp 703-719

[54] Gambling, W.A., H. Matsumura, C.M. Ragdale "Joint Loss in Single Mode Fibres" *Electronics Letters*, Vol. 14, No. 15, pp 491-492

[55] Gloge, D. "Weakly Guiding Fibres" *Applied Optics*, Vol. 10, No. 10, October 1971, pp 2252-2258

[56] Petermann, K. "Constraints for Fundamental-Mode Spot Size for Broadband Dispersion-Compensated Single-Mode Fibres" *Electronics Letters*, Vol. 19, No. 18, September 1983, pp 712-714

[57] Povlsen, J.H., S.B. Andreasen "Analysis on Splice, Microbending, Macrobending, and Rayleigh Losses in GeO_2-Doped Dispersion-Shifted Single-Mode Fibers" *IEEE Journal of Lightwave Technology*, Vol. LT-4, No. 7, July 1986, pp 706-710

[58] McCartney, D.J., D.B. Payne, J.V. Wright "Analysis of Splices in Shifted Zero Dispersion Monomode Fibre" *Electronics Letters*, Vol. 20, No. 2, January 1984, pp 78-80

[59] Hevey, L.M., S.L. Saikkonen, D.H. Taylor "Theoretical Splice Loss Study of Single-Mode Fibers" *Proceedings of the SPIE: Fiber Optic*

Couplers, Connectors, and Splice Technology, Vol. 479, May 1984, pp 48-52

[60] Burns, W.K., Moges Abebe, Carl A. Villarruel, Robert P. Moeller "Loss Mechanisms in Single-Mode Fibre Tapers" *IEEE Journal of Lightwave Technology*, Vol. LT-4, No. 6, June 1986, pp 608-613

[61] Payne, F.P., Hussey, C.D., Yataki, M.S. "Modelling Fused Single-Mode Fibre Couplers" *Electronics Letters*, Vol. 21, No. 11, May 1985, pp 461-462

[62] Payne, F.P., T. Finegan, M.S. Yataki, R.J. Mears, C.D. Hussey "Dependence of Fused Taper Couplers on External Refractive Index" *Electronic Letters*, Vol. 22 , No. 22, October 1986, pp 1207-1209

[63] Tucker, R.S., Kaminow, I.P. "High-Frequency Characteristics of Directly Modulated InGaAsP Ridge Wavaeguide and Buried Heterostructure Lasers" *IEEE J. of Lightwave Technology*, Vol. LT-2, Feb. 1984, pp 40-43

[64] Tucker, R.S. "High-Speed Modulation of Semiconductor Lasers" *IEEE Transactions on Electron Devices*, Vol. ED-32, No. 12, Dec. 1985, pp 2572-2584

[65] Tucker, R.S. "Large-signal circuit model for simulation of injection-laser modulation dynamics" *IEE Proceedings*, Vol. 128, Pt. 1, No. 5,

October 1981, pp 180-184

[66] Tucker, R.S., D.J. Pope "Circuit modeling of the effect of diffusion on damping in a narrow-stripe semiconductor laser" *IEEE Journal of Quantum Electronics*, Vol. QE-19, July 1983, pp 1179-1183

[67] Burrus, C.A., T.P. Lee, A.G. Dentai "InGaAs/InP p-i-n Photodiodes for Lightwave Communications at 0.95 to 1.65 μm Wavelengths" *IEEE Journal of Quantum Electronics*, Vol. QE-17, 1981, pp 232-237

Appendix 1

Physical Constants

Symbol	Quantity	Value
k	Boltzmann constant	1.38066×10^{-23} J/K
q	Elementary charge	1.60218×10^{-19} C
ϵ_0	Permittivity in vacuum	8.85418×10^{-14} F/cm
ϵ_r	Permittivity of SiO	10.5
h	Planck constant	6.62617×10^{-34} J-s
c	Speed of light in vacuum	2.99792×10^{10} cm/s
kT/q	Thermal voltage at 300 K	0.0259V

Appendix 2

Unit Prefixes

Multiple	Prefix	Symbol
10^{12}	tera	T
10^{9}	giga	G
10^{6}	mega	M
10^{3}	kilo	K
10^{-2}	centi	c
10^{-3}	milli	m
10^{-6}	micro	μ
10^{-9}	nano	n
10^{-12}	pico	p
10^{-15}	femto	f

```
/* This program performs a Monte Carlo simulation of splice */
/* loss for a dispersion shifted single mode fibre cable    */
/* operating at a wavelength of 1.55mu. The equations used  */
/* are derived from a deviated Gaussian analysis with a     */
/* Laplace spot size omega = 4.5mu.                         */

#include <stdio.h>
main()
/* Declare variables  */

{
    float alpha,delta,index,lambda,omega,omega1,pi,theta,xi;
    int na,nb,nc,nd,ne,nf,ng,nh,ni,nj,nk,nl,nm,nn,no,i,j,k;
    long random();
    float final,exp,temp;
    int seed,middle;
    srandom(seed);

/* Set variables to appropriate parameters */

    index=1.47;
    lambda=1.55e-6;
    omega=4.5;
    omega1=4.5e-6;
    pi=3.1415926;
    xi=.957-0.0053*omega1+.0131*omega1*omega1;
    i=0;
    exp=1e-6;

/* Set random number generator */

    seed=random();
    srandom(seed);


/* Begin evaluating equation   */

    for (i=1;i<10000;++i)
        {
        middle = random();
        final=random()/2000000000.0;
        delta=final*3.5;

        theta=(final*pi)/180;
        alpha=(((delta/omega*xi)*(delta/omega*xi))*2.17)+ (((2*index*pi/lambda)*(2*index*pi/lambda))*((xi*omega1*theta)*(xi*omega1*theta)))*2.17;
```

```
/* Set counters to record the number of times a */
/* certain interval has occurred                */

        if (alpha<.05)
           ++na;
        if (alpha>=.05 && alpha <.1)
           ++nb;
        if (alpha>=.1 && alpha <.15)
           ++nc;
        if (alpha>=.15 && alpha <.2)
           ++nd;
        if (alpha>=.2 && alpha <.25)
           ++ne;
        if (alpha>=.25 && alpha < .3)
           ++nf;
        if (alpha>=.3 && alpha < .35)
           ++ng;
        if (alpha>=.35 && alpha < .4)
           ++nh;
        if (alpha>=.4 && alpha < .45)
           ++ni;
        if (alpha>=.45 && alpha < .5)
           ++nj;
        if (alpha>=.5 && alpha < .55)
           ++nk;

        if (alpha>=.55 && alpha < .6)
           ++nl;
        if (alpha>=.6)
           ++nm;
        }
        printf("na = %d nb=%d nc = %d nd = %d ne = %d\n",na,nb,nc,nd,ne);
        printf("nf = %d ng=%d nh = %d ni = %d nj = %d\n",nf,ng,nh,ni,nj);
        printf("nk = %d nl=%d nm = %d\n",nk,nl,nm);

}
```

Appendix 4

SPICE INPUT

INGAASP LASER CIRCUIT SIMULATION

```
IIN 0 1 AC 1
RIN 1 0 47
CP 1 0 .23PF
LP 1 2 .63NH
RP 2 3 1
CS 3 0 9.7PF
RS 3 4 5.8
IL 4 0 DC 1NA CSC 4 0 2.8PF
CD 4 0 1NF
R1 4 0 .005
RS1 4 5 .02
LS 5 6 4.6PH
VOUT 6 0 AC 1
.AC DEC 50 100MEG 2000MEG
.PLOT AC VDB(4) IDB(VOUT)
.PRINT AC VDB(4) IDB(VOUT)
.END
```

```
SPICE INPUT
INGAAS PHOTODIODE CIRCUIT SIMULATION
IIN 1 0 DC .021MA
IS 0 1 AC 2.6PA
CJ 1 0 2.6PF
RJ 1 0 10K
RL 1 0 47
IT 0 1 AC 26.6PA
RI 1 0 47
VOUT 1 0 AC 1
.AC DEC 50 100MEG 2000MEG
.PLOT AC IDB(VOUT)
.PRINT AC IDB(VOUT)
.END
```

```
SPICE INPUT
INGAAS PHOTODIODE CIRCUIT SIMULATION - ON STATE
IIN 0 1 DC .074MA
IS 0 1 AC 5.8PA
CJ 1 0 0.6PF
RJ 1 0 10K
RL 1 0 47
IT 0 1 AC 26.6PA
*SWITCHING CIRCUIT
VEC 3 0 DC 10
*SWITCHING TRANSISTOR
QB 1 2 3 QNMOD
V2 2 0 4
*GROUNDING TRANSISTOR
VG 6 0 DC 0
MG 1 4 0 0 MDMOD L=10U W=5U
RB 5 2 3K
RD 4 0 1M
CD 6 4 2PF
*BUFFER AMPLIFIER
RBUF 1 0 1000
QBUF 7 1 8 QBUFMOD
RGND 8 0 330
LBUF 9 7 1MH
RBASE 1 9 1000
*RECEIVER CIRCUIT
JR 10 9 0 JRMOD
```

```
RT 10 11 11K
QR 13 14 10 QPMOD
QB 17 13 16 QN2MOD
RHI 13 18 1M
V4 18 0 DC -5
CHI 18 0 20PF
RN 16 18 1M
R2 1 20 2K
R3 16 20 1K
CQ 14 0 10PF
RQ 14 0 11.5K
RO 14 11 11.5K
CO 11 0 20PF
VO 11 0 DC 5
VOUT 16 0 AC 1
.MODEL QNMOD NPN BF=50 VAF=50 IS=1.E-12 RB=100 CJC=.1PF
TR=320PS TF=320PS
+ ISE=1.0E-12 ISC=1.0E-12
.MODEL MDMOD NMOS
+ LEVEL=2 VTO =0.510 KP=50.8E-5 GAMMA=0.470 PHI=0.650 RD=3.00E+00

+ RS=3.00E+00 IS=1.00E-20 PB=0.810 CGSO=2.570E-10 CGDO=2.570E-
10 CGBo=2.00E-11
+ RSH=60.000 CJ=1.00E-4 MJ=0.500 CJSW=1.80E-10 MJSW=0.330 TOX=4.70E-
08
.MODEL QBUFMOD NPN BF=100 RB=100 RE=1 CJE=2PF
.MODEL JRMOD NJF VTO=-3.0 BETA=1.0E-5 FC=.3
.MODEL QPMOD PNP BF=20 RB=100 TF=.1NS CJC 1PF
```

```
.MODEL QN2MOD NPN BF=75 RB=100 CJE=1PF
.AC DEC 50 100MEG 2000MEG
.PLOT AC IDB(VOUT)
.PRINT AC IDB(VOUT)
.END
```

```
SPICE INPUT
INGAAS PHOTODIODE CIRCUIT SIMULATION - OFF STATE
IIN 0 1 DC .021MA
IS 0 1 AC 2.6PA
CJ 1 0 2.6PF
RJ 1 0 10K
RL 1 0 47
IT 0 1 AC 26.6PA
*SWITCHING CIRCUIT
VEC 3 0 DC 10
*SWITCHING TRANSISTOR
QB 1 2 3 QNMOD
V2 2 0 0
*GROUNDING TRANSISTOR
VG 6 0 DC 3
MG 1 4 0 0 MDMOD L=10U W=5U
RB 5 2 3K
RD 4 0 1M
CD 6 4 2PF
*BUFFER AMPLIFIER
RBUF 1 0 1000
QBUF 7 1 8 QBUFMOD
RGND 8 0 330
LBUF 9 7 1MH
RBASE 1 9 1000
*RECEIVER CIRCUIT
JR 10 9 0 JRMOD
```

```
RT 10 11 11K
QR 13 14 10 QPMOD
QB 17 13 16 QN2MOD
RHI 13 18 1M
V4 18 0 DC -5
CHI 18 0 20PF
RN 16 18 1M
R2 1 20 2K
R3 16 20 1K
CQ 14 0 10PF
RQ 14 0 11.5K
RO 14 11 11.5K
CO 11 0 20PF
VO 11 0 DC 5
VOUT 16 0 AC 1
.MODEL QNMOD NPN BF=50 VAF=50 IS=1.E-12 RB=100 CJC=.1PF
TR=320PS TF=320PS
+ ISE=1.0E-12 ISC=1.0E-12
.MODEL MDMOD NMOS
+ LEVEL=2 VTO =0.510 KP=50.8E-5 GAMMA=0.470 PHI=0.650 RD=3.00E+00

+ RS=3.00E+00 IS=1.00E-20 PB=0.810 CGSO=2.570E-10 CGDO=2.570E-
10 CGBo=2.00E-11
+ RSH=60.000 CJ=1.00E-4 MJ=0.500 CJSW=1.80E-10 MJSW=0.330 TOX=4.70E-
08
.MODEL QBUFMOD NPN BF=100 RB=100 RE=1 CJE=2PF
.MODEL JRMOD NJF VTO=-3.0 BETA=1.0E-5 FC=.3
.MODEL QPMOD PNP BF=20 RB=100 TF=.1NS CJC 1PF
```

```
.MODEL QN2MOD NPN BF=75 RB=100 CJE=1PF
.AC DEC 50 100MEG 2000MEG
.PLOT AC IDB(VOUT)
.PRINT AC IDB(VOUT)
.END
```

```
SPICE INPUT
INGAAS PHOTODIODE CIRCUIT SIMULATION - ON STATE
FIN 0 1 POLY 1 0 -.2 IC=.074MA
IS 0 1 POLY 1 0 -.4 IC=5.8PA
CJ 1 0 POLY .6PF 0 1PF
RJ 1 0 10K
RL 1 0 47
IT 0 1 AC 26.6PA
*SWITCHING CIRCUIT
VEC 3 0 DC 10
*SWITCHING TRANSISTOR
QB 1 2 3 QNMOD
V2 2 0 PULSE 4 0 2NS 2NS 30NS
*GROUNDING TRANSISTOR
VG 6 0 PULSE 0 4 2NS 2NS 8NS
MG 1 4 0 0 MDMOD L=10U W=5U
RB 5 2 3K
RD 4 0 1M
CD 6 4 2PF
*BUFFER AMPLIFIER
RBUF 1 0 1000
QBUF 7 1 8 QBUFMOD
RGND 8 0 330
LBUF 9 7 1MH
RBASE 1 9 1000
*RECEIVER CIRCUIT
JR 10 9 0 JRMOD
```

```
RT 10 11 11K
QR 13 14 10 QPMOD
QB 17 13 16 QN2MOD
RHI 13 18 1M
V4 18 0 DC -5
CHI 18 0 20PF
RN 16 18 1M
R2 1 20 2K
R3 16 20 1K
CQ 14 0 10PF
RQ 14 0 11.5K
RO 14 11 11.5K
CO 11 0 20PF
VO 11 0 DC 5
VOUT 16 0 AC 1
.MODEL QNMOD NPN BF=50 VAF=50 IS=1.E-12 RB=100 CJC=.1PF
TR=320PS TF=320PS
+ ISE=1.0E-12 ISC=1.0E-12
.MODEL MDMOD NMOS
+ LEVEL=2 VTO =0.510 KP=50.8E-5 GAMMA=0.470 PHI=0.650 RD=3.00E+00

+ RS=3.00E+00 IS=1.00E-20 PB=0.810 CGSO=2.570E-10 CGDO=2.570E-
10 CGBo=2.00E-11
+ RSH=60.000 CJ=1.00E-4 MJ=0.500 CJSW=1.80E-10 MJSW=0.330 TOX=4.70E-
08
.MODEL QBUFMOD NPN BF=100 RB=100 RE=1 CJE=2PF
.MODEL JRMOD NJF VTO=-3.0 BETA=1.0E-5 FC=.3
.MODEL QPMOD PNP BF=20 RB=100 TF=.1NS CJC 1PF
```

```
.MODEL QN2MOD NPN BF=75 RB=100 CJE=1PF
.PLOT DC V(16)
.PLOT TRAN V(16) (0,4)
.PRINT TRAN V(16)
.DC VIN 4 0 0.1
.TRAN 1NS 50NS
.END
```

```
SPICE INPUT
INGAAS PHOTODIODE CIRCUIT SIMULATION - OFF STATE
FIN 0 1 POLY 1 0.2 IC=.021MA
IS 0 1 POLY 1 0 .4 IC=2.6PA
CJ 1 0 POLY 2.6PF 0 -1PF
RJ 1 0 10K
RL 1 0 47
IT 0 1 AC 26.6PA
*SWITCHING CIRCUIT
VEC 3 0 DC 10
*SWITCHING TRANSISTOR
QB 1 2 3 QNMOD
V2 2 0 PULSE 0 4 2NS 2NS 30NS
*GROUNDING TRANSISTOR
VG 6 0 0
MG 1 4 0 0 MDMOD L=10U W=5U
RB 5 2 3K
RD 4 0 1M
CD 6 4 2PF
*BUFFER AMPLIFIER
RBUF 1 0 1000
QBUF 7 1 8 QBUFMOD
RGND 8 0 330
LBUF 9 7 1MH
RBASE 1 9 1000
*RECEIVER CIRCUIT
JR 10 9 0 JRMOD
```

```
RT 10 11 11K
QR 13 14 10 QPMOD
QB 17 13 16 QN2MOD
RHI 13 18 1M
V4 18 0 DC -5
CHI 18 0 20PF
RN 16 18 1M
R2 1 20 2K
R3 16 20 1K
CQ 14 0 10PF
RQ 14 0 11.5K
RO 14 11 11.5K
CO 11 0 20PF
VO 11 0 DC 5
VOUT 16 0 AC 1
.MODEL QNMOD NPN BF=50 VAF=50 IS=1.E-12 RB=100 CJC=.1PF
TR=320PS TF=320PS
+ ISE=1.0E-12 ISC=1.0E-12
.MODEL MDMOD NMOS
+ LEVEL=2 VTO =0.510 KP=50.8E-5 GAMMA=0.470 PHI=0.650 RD=3.00E+00

+ RS=3.00E+00 IS=1.00E-20 PB=0.810 CGSO=2.570E-10 CGDO=2.570E-
10 CGBo=2.00E-11
+ RSH=60.000 CJ=1.00E-4 MJ=0.500 CJSW=1.80E-10 MJSW=0.330 TOX=4.70E-
08
.MODEL QBUFMOD NPN BF=100 RB=100 RE=1 CJE=2PF
.MODEL JRMOD NJF VTO=-3.0 BETA=1.0E-5 FC=.3
.MODEL QPMOD PNP BF=20 RB=100 TF=.1NS CJC 1PF
```

```
.MODEL QN2MOD NPN BF=75 RB=100 CJE=1PF
.PLOT DC V(16)
.PLOT TRAN V(16) (0,4)
.PRINT TRAN V(16)
.DC VIN 0 4 0.1
.TRAN 1NS 50NS
.END
```

VITA

Surname: STRACHAN Given Names: James Alan

Place of Birth: Nelson, B.C. Date of Birth: March 25,1957

Educational Institutions Attended, with Dates of Entering and Leaving:

UNIVERSITY OF VICTORIA	1975	to	1976
UNIVERSITY OF BRITISH COLUMBIA	1976	to	1980
UNIVERSITY OF VICTORIA	1985	to	1987

Degrees, Diplomas, Etc., Awarded, with Dates and Names of Institutions:

B.A.Sc. 1980 University of British Columbia, Vancouver

Honors and Awards:

B.C. Provincial Scholarship, 1975

C.U.P.E. Scholarship, 1975

Publications:

A. Strachan, V.K. Bhargava and E.H. Hara, "A 1.55μm Optoelectronic Broadband Matrix Switch". To be published in Proceedings, IEEE Pacific Rim Conference on Communications, Computers and Signal Processing, June 1987.

PARTIAL COPYRIGHT LICENSE

I hereby grant the right to lend my thesis (the title of which is shown below) to users of the University of Victoria Library, and to make single copies only for such users or in response to a request from the Library of any other university, or similar institution, on its behalf or for one of its users. I further agree that permission for extensive copying of this thesis for scholarly purposes may be granted by me or a member of the University designated by me. It is understood that copying or publication of this thesis for financial gain shall not be allowed without my written permission.

Title of Thesis

THE DESIGN AND ANALYSIS OF AN OPTOELECTRONIC

BROADBAND MATRIX SWITCH

Author

[redacted]

Signature

James Alan Strachan

Name

June 19, 1987

Date